論文 / 著書情報
Article / Book Information

題目(和文)	レーザ粉末焼結積層造形におけるPBT造形品の特性に関する研究
Title(English)	Study on material properties of poly(butylene terephthalate) processed by laser sintering
著者(和文)	荒井聡
Author(English)	Satoshi Arai
出典(和文)	学位:博士(工学), 学位授与機関:東京工業大学, 報告番号:甲第11279号, 授与年月日:2019年9月20日, 学位の種別:課程博士, 審査員:扇澤 敏明,鞠谷 雄士,森川 淳子,塩谷 正俊,淺井 茂雄
Citation(English)	Degree:Doctor (Engineering), Conferring organization: Tokyo Institute of Technology, Report number:甲第11279号, Conferred date:2019/9/20, Degree Type:Course doctor, Examiner:,,,,
学位種別(和文)	博士論文
Type(English)	Doctoral Thesis

Doctoral Dissertation

Study on material properties of poly(butylene terephthalate) processed by laser sintering

Satoshi Arai

Department of Organic and Polymeric Materials

Graduate School of Science and Engineering

Tokyo Institute of Technology

July 2019

Contents

Chapter 1

General introduction

1-1. Additive manufacturing

Additive manufacturing (AM), also well known as three-dimensional (3D) printing, has recently emerged as a subject of intense worldwide attention [1,2]. According to the Wohlers Report 2018 [3], the current AM market of $7.4 billion is expected to reach $18.2 billion in 2021 and $27.3 billion in 2023.

AM is the process of joining materials to make objects from 3D model data, usually layer by layer [4]. The process flow of general AM is shown in Fig. 1.

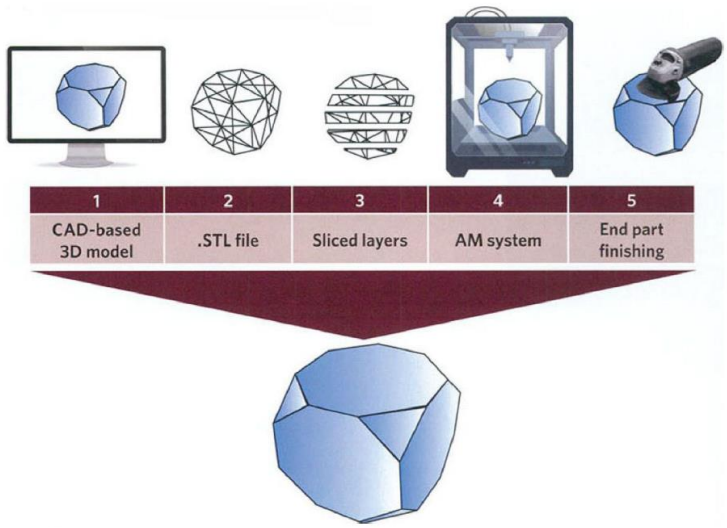

Fig. 1: Process flow of AM [5].

AM begins with a 3D model that can be created from structures built by computer-aided-design (CAD) software. A STL (Standard Triangle Language) file is commonly created from the 3D model. The data in the STL file is sliced into a build file of 2D layers and sent to the AM machine. Finally, after being formed by AM, the AM-formed parts are used after being post-processed such as removal of supports and blasting.

Since AM can obtain design samples and reduce the length of development cycles, it was first applied in the area of rapid prototyping [6,7], and that area of application continues to be exploited to the present day. Recently, as a result of improving the performance of AM technologies, AM is increasingly being used for direct manufacturing of parts in small to medium quantities [8-10]. In particular, AM beats traditional production methods in economic terms as shown schematically in Fig. 2(a) (b) [11].

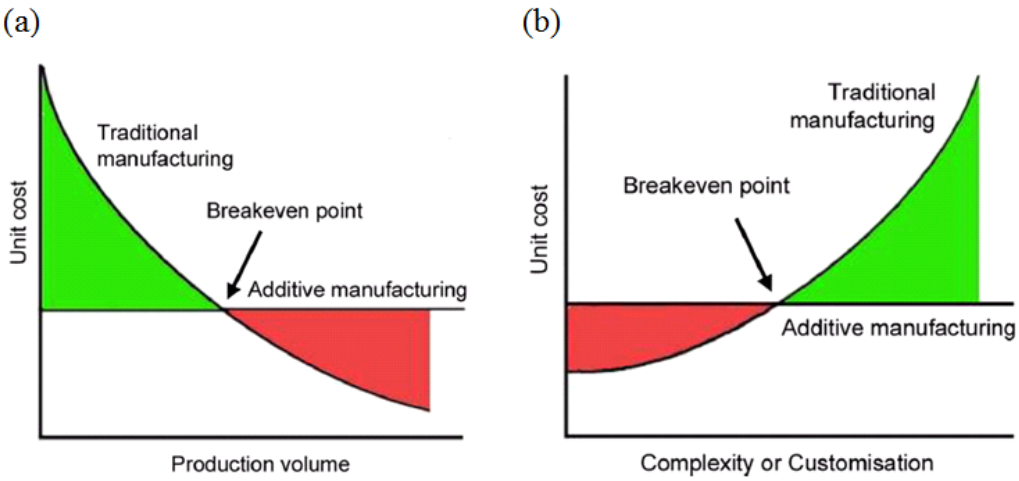

Fig. 2: Comparison of AM and traditional production methods: (a) unit production cost against production volume and (b) unit production cost against product complexity or customization [11].

Established production technologies are often optimized for large quantities of parts to be produced at the lowest possible cost. Typically, cost per unit decreases significantly with number of parts produced. The current position of the breakeven point for the high costs of AM systems, materials, preparation, and post processing mean large parts, high production volumes or rates, and high accuracy and surface finish quality typically render AM production more expensive than traditional manufacturing.

On the other hand, in regard to traditional production technologies, costs increase significantly with increasing the complexity of the part. Usually, a limit of complexity is reached with traditional methods, and it cannot be overcome easily or can be overcome only at exorbitantly high cost. Herein can be found the advantages of AM; that is, the unit cost is almost unchanged for small part quantities or parts with substantial complexity. In contrast to the situation with traditional production technologies, increasing complexity of AM parts incurs minimal additional costs, and any customization can be done digitally without the need for additional processing cost. Especially, in the future, the breakeven point is expected to shift significantly due to the progress of AM technology.

In light of the above-described circumstances, AM is best suited to applications requiring complex, high value, time-sensitive, and customized products, such as automobile and aerospace parts (i.e., complex designs), replacement of broken parts (i.e., time-sensitive), and medical implants (i.e., highly customized) [5].

In the field of polymer AM, the methods available are classified as shown in Fig. 3 [12].

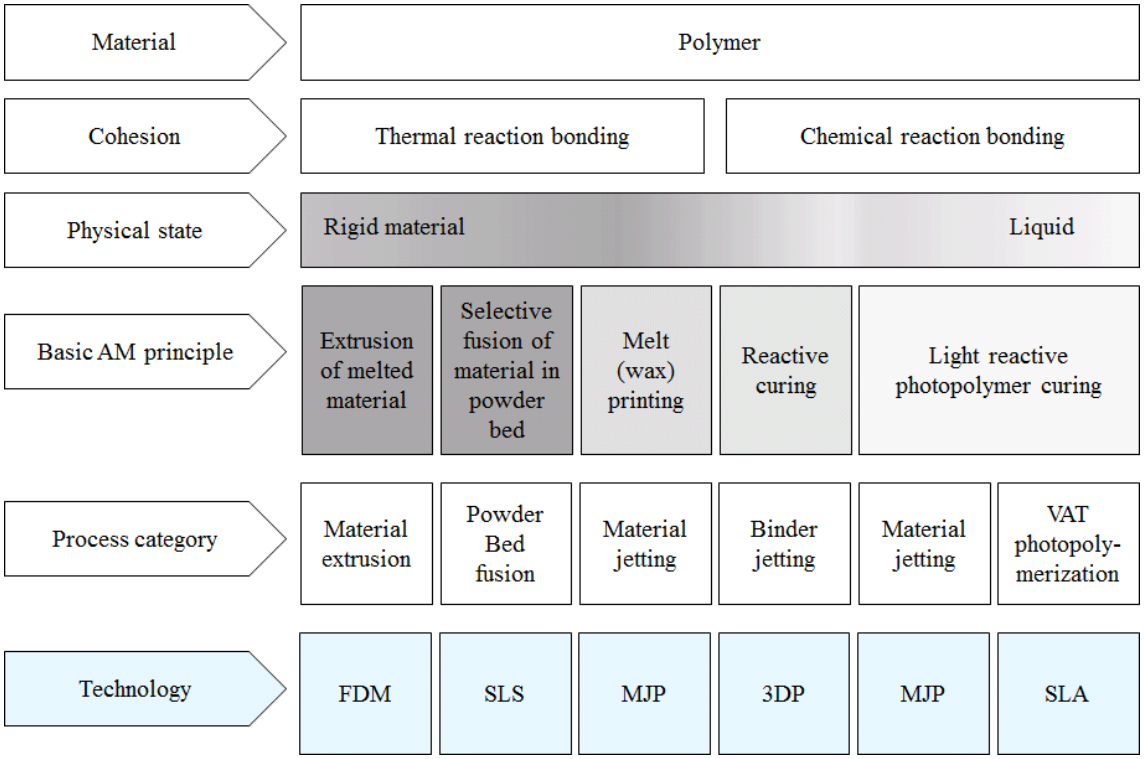

Fig. 3: Characterization matrix for AM processes with polymers [12].

This classification is based on ISO 17296-2:2015 in terms of material and process matrix, and the AM technologies listed in the figure can be characterized as follows.

- **Material extrusion (fused deposition modeling (FDM®))**

As shown in Fig. 4(a), FDM is the most popular AM technology in terms of number of fabricators. FDM machines work by controlled extrusion of thermoplastic filaments [13]. In the case of FDM, the filaments melt into a semi-liquid state at the extrusion nozzle, and in that state, they are extruded layer by layer onto the build platform, where the layers are fused together and solidify into finished parts.

- **Powder bed fusion (selective laser sintering (SLS))**

SLS is a type of powder-bed fusion wherein a bed of powdered polymer (resin) is targeted partially by a high-power directional heating source (such as a laser) to form a

solidified layer of fused powder. The principle of SLS is explained in detailed in Chapter 1.2.

- **Material jetting (including wax and inkjet)**

As shown in Fig. 4(b), a material-jetting printer (MJP) selectively deposits droplets of material onto a build platform [14]. Generally, current commercial material-jetting technologies use wax or photosensitive polymers, which are cured upon deposition.

- **Binder jetting (3D printing (3DP))**

As shown in Fig. 4(c), a 3D printer (3DP) deposits liquid in the form of droplets onto a binder powder material [13]. Often, the binder has adhesive qualities and is ink-jetted onto the surface of a powder bed. Production of structural materials typically requires some form of post-processing to remove the binder and to densify the constituent powder.

- **VAT polymerization (stereolithography apparatus (SLA))**

A SLA uses photopolymers that can be cured by ultraviolet (UV) laser. As shown in Fig. 4(d), the UV laser is controlled so that the laser beam keeps to the desired path in a reservoir of resin, which is a photocurable resin that polymerizes into a 2D patterned layer. After each layer is cured, the platform lowers and another layer of uncured resin is ready to be patterned [7].

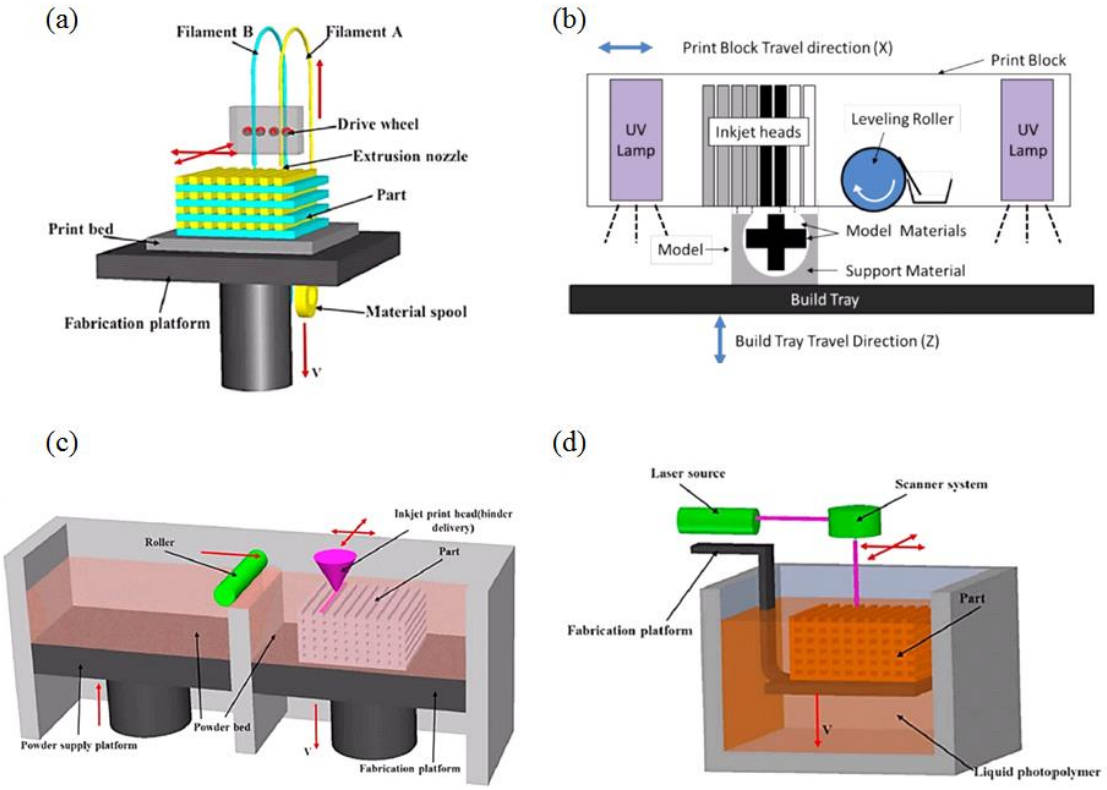

Fig. 4: Schematic diagrams of four methods of AM: (a) material extrusion [13], (b) material jetting [14], (c) binder jetting [13], and (d) VAT polymerization [13].

Due to the different technological approaches taken to produce AM parts, it can be expected that the resulting products have very different properties. A qualitative evaluation of the AM processes in terms of component properties for various boundary conditions is shown in Table 1 [12]. With this table, it is possible to define the predominant uses of parts produced with the different AM methods.

Table 1: Qualitative evaluation of the AM processes in terms of component properties and field of applications [12].

Technology	FDM	SLS	MJP (wax printing)	3DP	MJP (UV-polymer printing)	SL
Support structure requirements	Yes	No	Yes	No	Yes	Yes
Qualitative evaluation of AM parts						
Mechanical properties	+++-	++++	+----	+----	++--	++--
Thermal properties	++--	+++-	----	+++-	++--	+---
Part precision	+----	++--	++++	++--	++++	++++
Surface quality	+---	++--	++++	++--	++++	++++
Predominant use of AM parts						
Model	×		×	×	×	×
Product development	×	×	×		×	×
Functional parts	(×)	×				

++++ Very good properties
+++- Good properties
++-- Acceptable properties
+--- Poor properties
---- Unsatisfactory properties

The compilation in Table 1 shows that methods such as SLA or MJP (using UV polymer) provide outstanding results with respect to surface finish and part precision; however, they have characteristic weakness with respect to long-term stability. Low mechanical stability is a disadvantage of 3DP and a barrier to its use for production of functional components. However, 3DP can be used to make models that can be colored by introducing a binder or models can be created by using a variety of possible substrate powders (e.g., plastic, metals, ceramics, and inorganic powders). With 3DP, the user is able to produce attractive models very quickly. Specifically, the fabrication of architectural models and the new business model based on miniature figures are based on 3DP. Prototypes made by MJP (using wax) are often used in a range of

precision-casting processes as lost-wax models. FDM uses thermoplastic filaments such as polycarbonate (PC), acrylonitrile butadiene styrene (ABS), and polylactic acid (PLA). Therefore, FDM-produced parts have high mechanical and thermal properties. Moreover, composite materials containing relatively long fibers (such as carbon fiber) can be added to the filaments, so the properties can be further improved [15,16]. Another advantage of FDM is its potential to allow diverse materials to be deposited simultaneously. FDM printers can be fitted with multiple extrusion nozzles loaded with different materials, so multi-functional parts can be printed with designed composition [13]. However, FDM also has the disadvantages that accuracy and surface precision are poor and that regular vacancies inevitably remain between the extruded lines [16].

In regard to SLS, although the equipment price is higher than that in the case of the other methods, mechanical properties and thermal characteristics of SLS-produced parts are good, and since SLS uses a laser, it has relatively high accuracy and low surface roughness in comparison with FDM. In contrast to FDM, SLS has two more significant merits: (i) it does not use supports and (ii) it has numerous degrees of freedom in terms of shape. This study therefore focuses on SLS, namely, one of the most anticipated and widely used AM technologies for end-use parts.

1-2. Selective laser sintering

1-2-1. General principle

SLS is one of the main processes in the rapidly evolving AM field available in the market for production of high-performance polymer parts. As for SLS, mainly, three-dimensional laminates are formed by irradiating a thinly laid powder with a laser beam and repeating the process.

As shown in Fig. 5, a SLS system is composed of a part cartridge (hereafter referred to as a "powder bed") for arranging the powder for molding and the modeled object, a piston for moving up and down a feed cartridge for supplying material to the part cartridge, a roller for supplying new powder material, heaters for heating the powder bed and the material-supply point, and a laser for selectively heating parts of the surface of the powder bed.

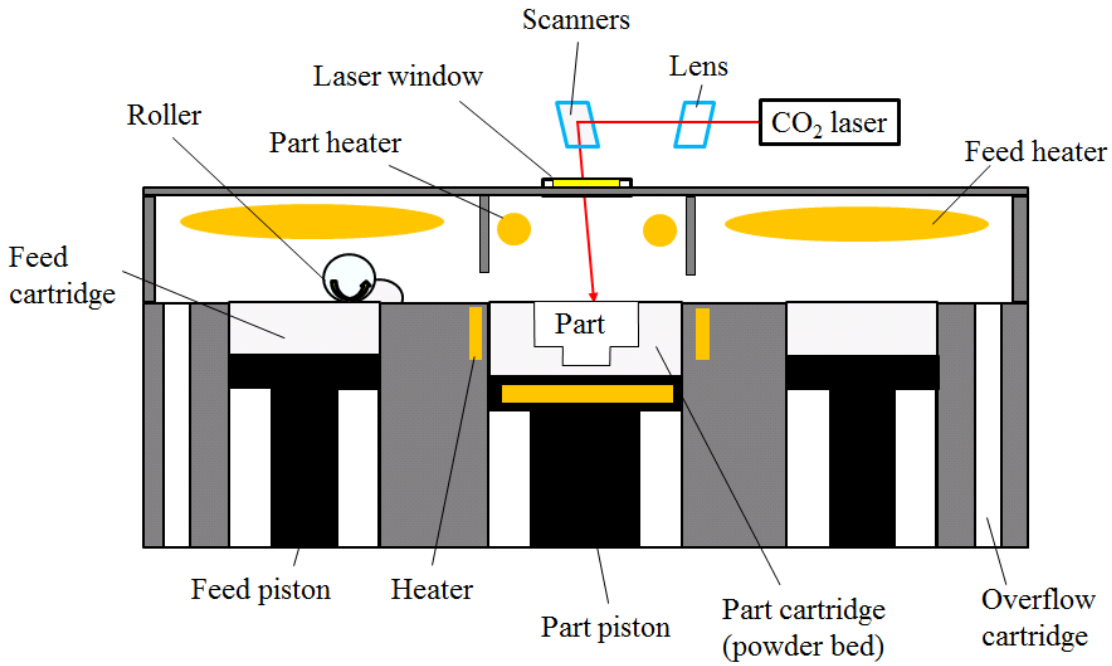

Fig. 5: Schematic diagram of an SLS system.

A schematic diagram of the modeling procedure is shown in Fig. 6 [17]. First, a roller is used to spread the powder on the powder bed. Next, on the basis of slice data obtained from a CAD model, laser irradiation is performed to selectively sinter and solidify the powder of the powder bed. After that, the feed cartridge (in the vicinity where the roller is disposed) is raised by the piston, and the powder bed and the other feed cartridge are lowered by the piston. By repeating the supply of powder, selective solidification by laser irradiation, and sintering the lower layer, a three-dimensional

shape is formed. Upon completion of the SLS build, the part and surrounding supporting material in the build chamber, collectively known as the "part cake," are removed from the SLS system. The part is removed from the part cake, and the loose powder is either brushed off or bead-blasted away. Unfused powder is sieved and reused for subsequ

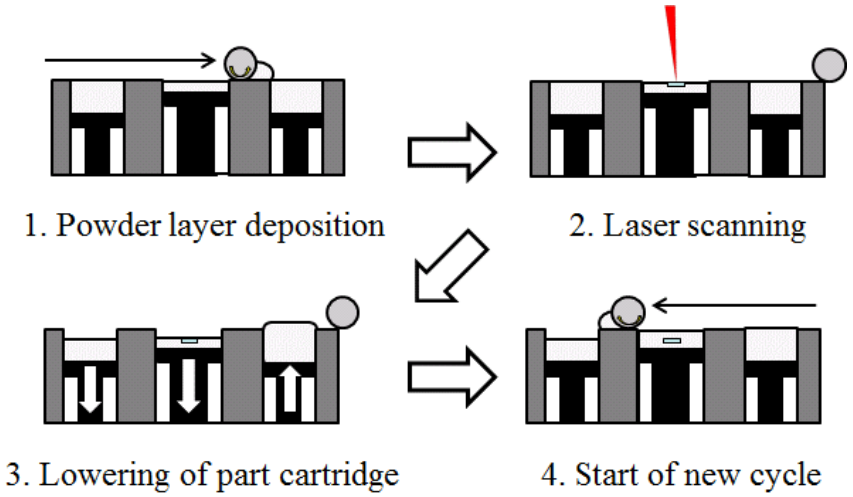

Fig. 6: Schematic of SLS process [17].

SLS has a number of advantages over other polymer AM technologies. First, SLS does not require the use of the support structures that are required by many other additive processes for supporting overhangs and thin walls in the part as it is built. In the case of SLS, the part is supported by the surrounding unfused powder as it is built.

As for SLS, the most-important parameters are temperature control around the powder bed and laser-irradiation conditions [18]. The thermal behavior of the powder-bed area is represented on a DSC diagram in Fig. 7. Moreover, it is necessary to preheat the temperature of the powder bed (points A and C) to near the melting point of the resin (i.e., above its crystallization temperature) during molding.

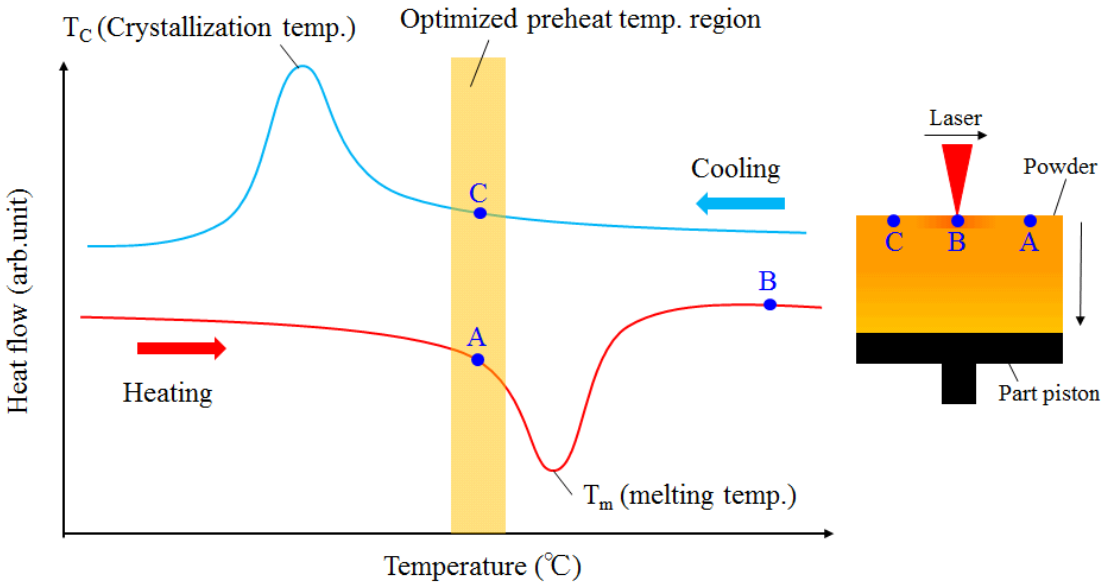

Fig.7: Schematic of the DSC curves of a crystalline polymer.

For example, if the points A and C are close to the crystallization temperature rather than above it, as shown in Fig. 8 [19], some parts will warp after laser irradiation and eventually strike the roller, causing the trouble that the part moves or the systems stops. On the other hand, when the temperature of points A and C is high, porosity is reduced, and the mechanical properties of the SLS-shaped part are improved [20]; however, when it is too high, the resin powder in the powder bed melts and aggregates. As a result, the phenomenon occurs that the powder cannot be laid smoothly. That situation leads to a decrease in the density of the parts, that is, a decrease in mechanical properties. Consequently, in particular, it is necessary to precisely control the temperature of the entire powder bed.

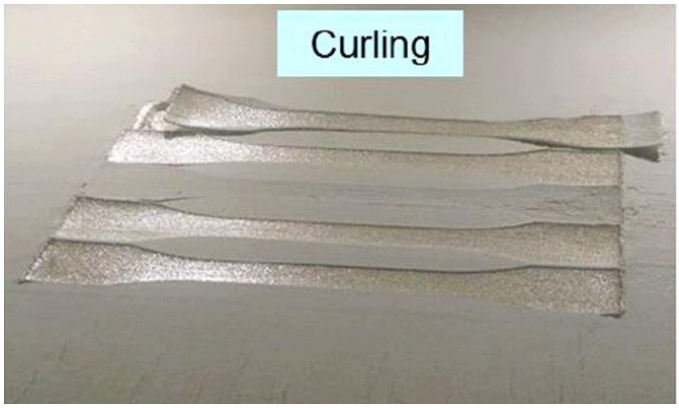

Fig. 8: Problems observed during SLS processing: "curling" [19]

The main parameters concerning laser-irradiation conditions are laser power, scan direction, scan speed, and scan spacing. In addition to scan direction, laser-energy density (E) [21] expressed by Equation (1) is used as a parameter considering laser power, scan speed, and scan spacing as follows:

$$E = \frac{P}{vS} \tag{1}$$

where P is laser power, v is scan speed, and S is scan spacing. Higher energy densities have been associated with improved particle fusion and mechanical properties; however, if it is excessive, it leads to unwanted smoking from degradation of the sintered part, as shown in Fig. 9 .

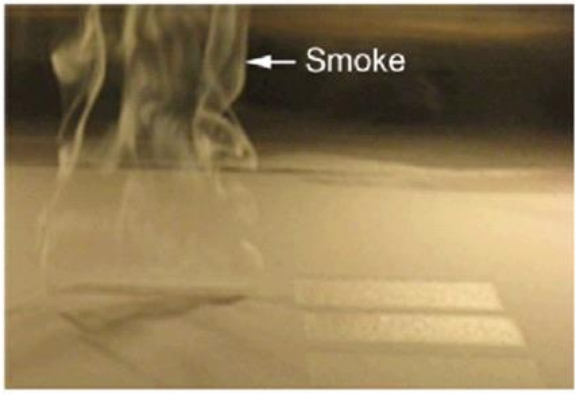

Fig. 9: Smoke generated during SLS processing using excessive laser-energy input [22].

In addition, powder-laminate thickness is another important parameter [18]. The thickness of the layers that make up the part influences the productivity of the laser-sintering process because the thicker the layer, the less time it takes to build the part. However, thick layers have a negative effect on surface roughness, and their quality is low due to high porosity. The maximum layer thickness is restricted by the depth of penetration of the laser energy into the powder, which is determined by energy density, particle size, powder density, thermal conductivity, compaction, and specific heat of the material [23, 24]. However, in the case of general SLS, the laminated thickness is often 100-150 μm [25, 26].

1-2-2. Available materials

In SLS, thermoplastic resins (either semi-crystalline polymer or amorphous polymer) are used. Amorphous polymers do not have a defined melting point; instead they have a glass-transition temperature (Tg), above which the polymer gradually softens and ultimately becomes a viscous liquid. They are therefore consolidated by heating above

their Tg. As these materials are heated, their melt viscosity decreases; however, it does not decrease rapidly. Consequently, sintered parts tend to exhibit high levels of porosity, thus low strength and poor precision [27]. In contrast, as for a semi-crystalline polymer, as temperature rises above the melting point of the polymer, melt viscosity decreases rapidly; consequently, the mechanical properties of the sintered part are improved, and manufacturing precision is high [27]. Accordingly, as for final products, crystalline resin is used for SLS.

The global polymer market, including that for the SLS polymers, is broken down in Fig. 10 [19].

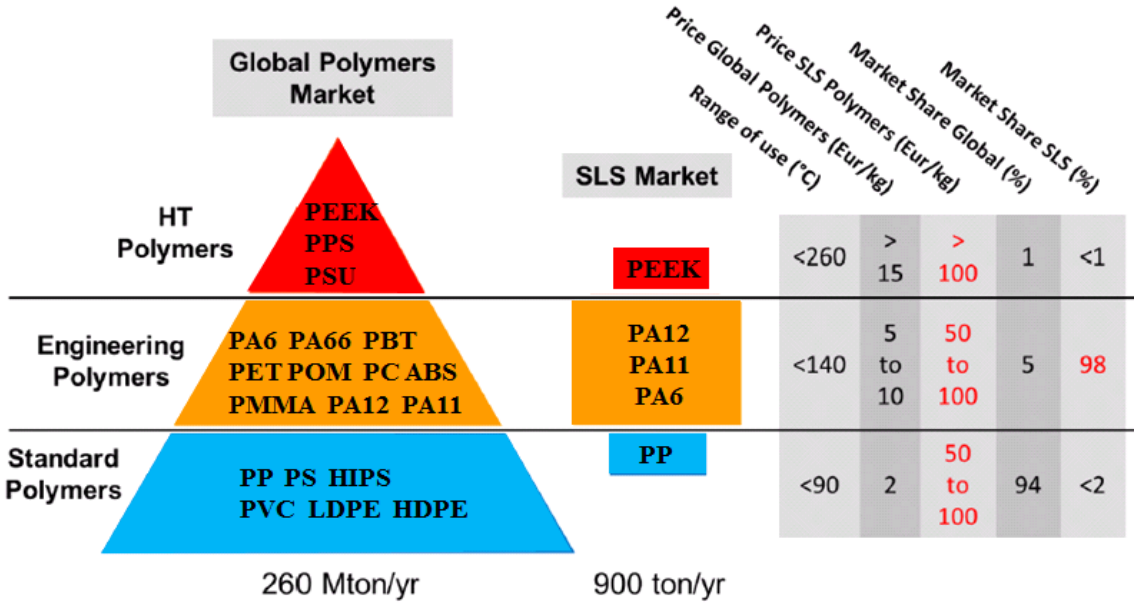

Fig. 10: Market overview and comparison of global and SLS polymer materials [19].

Normally, as for the global polymers market, the market for standard polymers (including polypropylene (PP)) makes up over 90 %; in contrast, as for the SLS-polymers market, engineering polymers dominate with a 98 % market share, of which polyamide 12 (PA12) is the most-used polymer worldwide for SLS applications.

Moreover, according to Goodridge [18], it is also reported that PA12 has captured more than 95 % of the market for laser AM materials. Thefore, tight restrictions are imposed on laser AM materials and act as a barrier to their widespread application. Recently, new materials have been introduced into the market (e.g., polyamide 6 (PA6) and PP); however, their volume still remains low.

Furthermore, in the case of a general molding apparatus, from the viewpoint of the melting point and cost of PA12, the upper limit value of the temperature of the powder bed is usually set to about 200 °C. As a result, it is difficult to use a resin material having a high melting point. However, specialized equipment (e.g., EOS-P800, EOS GmbH) specialized for high-melting-point resin that can mold poly(ether ether ketone) (PEEK) [28] and poly(ether ketone) (PEK) [29] has been commercialized and is beginning to be used; however, its very high equipment cost is a problem. In the case of SLS, from the viewpoint of part density and surface quality, the correct powder size is set to 90 μm or less [30]. In particular, part density, surface quality, and accuracy of the produced parts have all been found to increase with decreasing particle size; however, when powder size becomes too small, it is difficult to lay uniform powder by static forces [30]. Four commercially available PA powders, namely, (A) PA12-PA2200 (EOS GmbH), (B) PA12-Orgasol (Arkema SA), (C) PA11-Rilsan (Arkema SA), and (D) PA6-Sinterline SA, are shown in Fig. 11 [31].

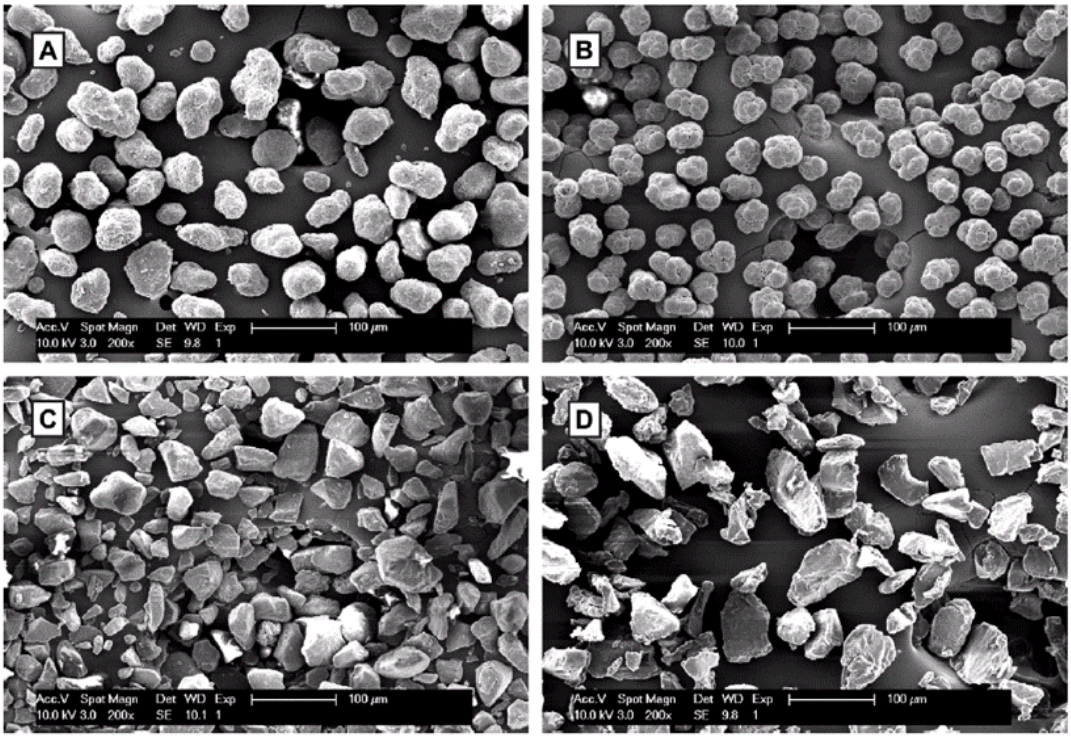

Fig. 11: SEM images of PA12–PA2200 (A), PA12–Orgasol (B), PA11–Rilsan (C), and PA6–Sinterline (D) [31].

Powder sizes D50 of PA12–PA2200, PA12–Orgasol, PA11–Rilsan, and PA6–Sinterline are 58.6, 42.3, 44.2, and 57.9 μm, respectively [31]. In regard to PA12–PA2200, a solution–precipitation process in ethanol at elevated temperature is used to obtain spherical particles, and TiO_2 and silicas are added to improve whiteness and flowability [31]. In regard to PA12–Orgasol, the cauliflower-shaped morphology is the direct result of the polymerization process used [31]. On the other hand, PA11 and PA6 consist of rough particles with sharp edges, which probably result from milling. In regard to PEEK [28] and PEK [29] as well, milling is used for powdering them. In other words, except for PA12, milling is the major means of powdering the resins. Accordingly, besides PA12, studies on the powdering method and the processability of SLS are being actively conducted.

1-3. Objective of this thesis

Among engineering plastics, PBT resin is used in large amounts and is regarded as one of the five major engineering plastics. In particular, PBT possesses several advantageous features, namely, high heat resistance, good mechanical and electrical properties, high chemical resistance, and low cost [32]. PBT is primarily used in injection-molding applications, although it is also used in film applications. It also has low melt viscosity and very fast crystallization, which allow for easy molding [32]. SLS is a means of sintering by laser irradiation under a condition in which the powder-bed temperature is set to a temperature at which crystallization speed is low. From the standpoint of the SLS process, as for the resin used, a wide processing window (i.e., the difference between melting point and crystallization temperature) is required, and a low crystallization speed at powder-bed temperature is desirable. Therefore, SLS with PBT is difficult, and very few research examples have been reported [33-35].

In light of the above-described circumstances, in this research, PBT resin—having many good characteristics—was used to evaluate various basic characteristics SLS. And these varied characteristics of SLS were compared with those of IM.

In Chapter 2, it was explained that by using copolymer PBT(cPBT) with lower crystallinity than homo PBT, it was possible to produce parts with excellent characteristics by SLS. Moreover, various characteristics of SLS specimens were compared with those of IM specimens.

To use an SLS product as a final product, flame-retardant properties may be necessary in some cases. Therefore, as explained in Chapter 3, the effect of adding flame retardant and flame-retardant promoter to cPBT was evaluated, and the flame-retardant property was compared the that of IM products.

In the case that heat resistance and rigidity are required, generally, a composite is formed by adding glass fiber or the like. As a result, PBT is being increasingly applied to injection molding. For that reason, as explained in Chapter 4, short-fiber fiberglass (short glass fiber (SGF) hereafter) was added to cPBT, and the characteristics of that composite with SGF addition as a parameter were examined. Like an IM product, an SLS product features anisotropy due to arrangement and anisotropy due to SGF addition.

In the case SLS, it is known that porosity is a serious problem. Therefore, as explained in Chapter 5, to reduce the influence of anisotropy due to arrangement and SGF (by using 30 wt% of SGF added to cPBT), the number of laser scans was taken as twice per layer, and the effect of the scanning process was evaluated. And the SLS-formed product was compared with an IM product in terms of SGF orientation.

References

[1] M.K. Thompson, G. Moroni, T. Vaneker, G. Fadel, R.I. Campbell, I. Gibson, A. Bernard, J. Schulz, P. Graf, B. Ahuja, F. Martina, Design for additive manufacturing: trends, opportunities, considerations, and constraints, CIRP Ann. Manuf. Technol. 65 (2016) 737-760.

[2] R. Jiang, R. Kleer, F.T. Piller, Predicting the future of additive manufacturing: A Delphi study on economic and societal implications of 3D printing for 2030, Technol. Forecast. Soc. Change, 117 (2017) 84-97.

[3] Wohlers Report 2018. Wohlers Associates.

[4] ASTM F2792-12a, Standard Terminology for Additive Manufacturing Technologies, ASTM International; 2012.

[5] J.R.C. Dizon, A.H. Espera, Q. Chen, R.C. Advincula, Mechanical characterization of 3D-printed polymers, Addit. Manuf. 20 (2018) 44–67.

[6]J.P. Kruth, Material increase manufacturing by rapid prototyping techniques, CIRP Ann. Manuf. Technol. 40 (1991) 603-614.

[7]A. Bernard, A. Fischer, New trends on rapid product development, CIRP Ann. Manuf. Technol. 51 (2002) 635-652.

[8] B.P. Conner, G.P. Manogharan, A.N. Martof, L.M. Rodomsky, C.M. Rodomsky, D.C. Jordan, J.W. Limperos, Making sense of 3-D printing: Creating a map of additive manufacturing products and services, Addit. Manuf. 1-4 (2014) 64–76.

[9] S. Ford, M. Despeisse, Additive manufacturing and sustainability: an exploratory study of the advantages and challenges, J. Clean. Prod. 137 (2016) 1573-1587.

[10]S.A.M Tofail, E.P. Koumoulos, A. Bandyopadhyay, S. Bose, L. O'Donoghue, C. Charitidis, Additive manufacturing: scientific and technological challenges, market uptake and opportunities, Mater. Today. 21 (2018) 22–37.

[11] A.J. Pinkerton, Lasers in additive manufacturing, Opt. Laser Technol. 78 (2016) 25–32.

[12] M. Scmid, Laser sintering with plastics technology, processes, and materials, HANSER, 2018.

[13] X. Wang, M. Jiang, Z. Zhou, J. Gou, D. Hui, 3D printing of polymer matrix composites: A review and prospective, Composites: Part B 110 (2017) 442–458.

[14] J.P. Moore, C.B. Williams, Fatigue properties of parts printed by PolyJet material jetting, Rapid Prototyp. J. 21 (2015) 675-685.

[15] G.D. Goh, Y.L. Yap, S. Agarwala, W.Y. Yeong, Recent Progress in Additive Manufacturing of Fiber Reinforced Polymer Composite, Adv. Mater. Technol. 2018, 1800271.

[16] P. Parandoush, D. Lin, A review on additive manufacturing of polymer-fiber composites, Compos. Struct. 182 (2017) 36–53.

[17] S. Dupin, O. Lame, C. Barrès, J.-Y. Charmeau, Microstructural origin of physical and mechanical properties of polyamide 12 processed by laser sintering, Eur. Polym. J. 48 (2012) 1611–1621.

[18] R.D. Goodridge, C.J. Tuck, R.J.M. Hague, Laser sintering of polyamides and other polymers, Prog. Mater. Sci. 57 (2012) 229–267.

[19] A.F. Amado Becker, Characterization and Prediction of SLS Processability of Polymer Powders with Respect to Powder Flow and Part Warpage. (Doctoral thesis), ETH Zürich, Switzerland, 2016.

[20] A.E. Tontowi, T.H.C. Childs, Density prediction of crystalline polymer sintered parts at various powder bed temperatures, Rapid Prototyp. J. 7 (2001) 180-184.

[21] N. Hopkinson, C.E. Majewski, H. Zarringhalam, Quantifying the degree of particle melt in Selective Laser Sintering®, CIRP Ann. Manuf. Technol. 58 (2009) 197-200.

[22] D. Bourell, J.P. Kruth, M. Leu, G. Levy, D. Rosen, A.M. Beese, A. Clare, Materials for additive manufacturing, CIRP Ann. Manuf. Technol. 66 (2017) 659-681.

[23] H. Chung, S. Das, Processing and properties of glass bead particulate-filled functionally graded nylon-11 composites produced by selective laser sintering, Mater. Sci. Eng. A 437 (2006) 226-234.

[24] I. Gibson. D. Shi, Material properties and fabrication parameters in selective laser sintering process, Rapid Prototyp. J. 3 (1997) 129-136.

[25] H. Zarringhalam, N. Hopkinson, N.F. Kamperman, J.J. de Vlieger, Effects of processing on microstructure and properties of SLS Nylon 12, Mater. Sci. and Eng. A 435–436 (2006) 172–180.

[26] T. Stichel, T. Frick, T. Laumer, F. Tenner, T. Hausotte, M. Merklein, M.Schmidt, A Round Robin study for Selective Laser Sintering of polyamide 12: Microstructural origin of the mechanical properties, Opt. Laser Technol. 89 (2017) 31–40.

[27] C. Yan, Y. Shi, L. Hao, Investigation into the differences in the selective laser sintering between amorphous and semi-crystalline polymers. Int. Polym. Process 4 (2011) 416–423.

[28] Y. Wang, D. Rouholamin, R. Davies, O.R. Ghita. Powder characteristics, microstructure and properties of graphite platelet reinforced Poly Ether Ether Ketone composites in High Temperature Laser Sintering (HT-LS), Mater. Des. 88 (2015) 1310–1320.

[29] O.R. Ghita, E. James, R. Davies, S. Berretta, B. Singh, S. Flint, K.E. Evans. High temperature laser sintering (HT-LS): an investigation into mechanical properties and shrinkage characteristics of poly (ether ketone) (PEK) structures, Mater. Des. 61 (2014) 124–132.

[30] R.D. Goodridge, K.W. Dalgarno, D.J. Wood, Indirect selective laser sintering of an apatite–mullite glass–ceramic for potential use in bone replacement applications, Proc IMechE Part H: J Eng Med 220 (2006) 57-68.

[31] L. Verbelen, S. Dadbakhsh, M. Van den Eynde, J.-P. Kruth, B. Goderis, P. Van Puyvelde, Characterization of polyamide powders for determination of laser sintering processability, Eur. Polym. J. 75 (2016) 163–174.

[32] J. Scheirs, T.E. Long, Modern polyesters: chemistry and technology of polyesters and copolyesters, Wiley, Chichester, 2003.

[33] J. Schmidt, M. Sachs, M. Zhao, S. Fanselow, K. Wudy, M. D. D. Drummer, K. E. Wirth, W. Peukert. A novel process for production of spherical PBT powders and their processing behavior during laser beam melting, AIP Conf. Proc. 1713, 14008, (2016) 1-8.

[34] J. Schmidt, M. Sachs, S. Fanselow, M. Zhao, S. Romeis, D. Drummer, K. E. Wirth, W. Peukert. Optimized polybutylene terephthalate powders for selective laser beam melting, Chem. Eng. Sci. 156 (2016) 1-10.

[35] G.V. Salmoria, V.R. Lauth, M.R. Cardenuto, R.F. Magnago, Characterization of PA12/PBT specimens prepared by selective laser sintering, Opt. Laser Technol. 78 (2018) 92–96.

Chapter 2

Characterization of laser sintered PBT parts in comparison with injection molded parts

2-1. Introduction

Selective laser sintering (SLS) is a method mainly used for forming three-dimensional structures by repeatedly irradiating a thin layer of powder with a laser beam. Among additive manufacturing (AM) methods, SLS is the most promising from the viewpoints of quality and precision. A particular advantageous feature of SLS in comparison to other AM methods is that it does not require a support to prevent deformation during molding. Accordingly, compared to conventional processing methods like injection molding (IM), SLS has several advantages, such as a high degree of freedom in regard to product design, ease of handling customization, low cost, and the possibility of fabrication in a short time in the case of low manufacturing volumes. Due to these advantages, SLS is mostly being utilized for fabricating end-use components in the aerospace, automotive, and medical fields [1].

As one semi-crystalline polymer, polyamides (namely, "polyamides 11 and 12"; PA 11 and PA12, hereafter) are most-widely used as standard materials for laser AM [2]. It is reported that PA12 has captured more than 95 % of the market for laser AM materials [2]. Despite that situation, tight restrictions are imposed on laser AM materials and act as a barrier to their widespread application. In response to that issue, other semi-crystalline polymers—such as polyethylene [3,4], polypropylene [5,6], polyoxymethylene [7], polyamide 6 [8, 9], poly(butylene terephthalate) (PBT)[10, 11], poly(ether ketone) [12,13], and poly(ether ether ketone) [14,15], are being actively researched, and some have been commercialized.

As a diverse crystalline resin that has spread to a wide range of industrial applications, PBT possesses several advantageous features, namely, high heat resistance, good mechanical and electrical properties, high chemical resistance, and low cost. PBT has a

high crystallization speed, so it tends to be used for IM—which requires shortening of the takt time in order to reduce costs. SLS is a means of sintering by laser irradiation under a condition in which the powder-bed temperature is set to a temperature at which crystallization speed is low [2]. From the standpoint of the molding process (i.e., SLS), as for the resin used, a wide processing window is required, and a low crystallization speed is desirable. In the case of using "homo PBT" powder with melting point of 223 °C, as reported by Schmidt et al. [10,11], building temperature for SLS was set at 210 °C. However, as for commercial SLS apparatuses still in general use, maximum powder-bed temperature is fixed at around 200 °C [2]. Due to these factors, "homo PBT"—which is used for normal IM—is supposed to be unsuitable for SLS. Copolymer PBT (cPBT) [16,17] is known as a material whose crystallization speed and crystallization temperature decrease with decreasing melting point. However, as melting point decreases, crystallization temperature decreases at a greater rate, so the process window becomes wider. Accordingly, in the present study, in which it is supposed that the powder-bed temperature is set below 200 °C, the possibility of using cPBT as a sintering material is focused on. In particular, the crystallization properties of pellets and powder, as well as the mechanical and crystallization properties of SLS specimens in comparison to IM ones, are investigated.

2-2. Experimental methods

2-2-1. Sample preparation

Material

cPBT (containing 10 mol% isophthalic acid) powder formed by "cryomilling" (namely, mechanical milling at cryogenic temperature) of (non-commercial) cPBT

pellets was used. The size of pellets was about 4 × 3 × 1.5 mm, and their average molecular weight (Mn) and density were 9.03×10^3 (in PMMA-converted molecular weight) and 1.29 g/cm^3, respectively. Melting point and crystallization temperature of the cPBT pellets are 207.5 and 150.7 °C, respectively.

In the cryomilling, a pin mill (Contraplex 400 C, Makino Mfg, Co. Ltd.) was used. The rotation speed of the pin disk was 145 m/s, and the operating time at -100 °C was from 90 to 240 min. The obtained cPBT powder was passed through a sieve with hole diameter of 106 μm. An SEM image and particle-size distribution of the cPBT powder are shown in Figs. 1(a) and (b), respectively.

The resulting powder size of D10, D50, and D90 was 31, 76, and 132 μm, respectively. As regards a material for SLS, flowability of the powder is a key property, and fumed silica is effective for improving the flowability [11,18,19]. Accordingly, hydrophobic fumed silica (AEROSIL®RA200H; Evonik Industries) was added (at mass fraction from 0.05 to 1.0 wt%) to the cPBT powder as a parameter. Average primary particle size of silica used was about 12 nm. The cPBT powder and silica were mixed for 15 min by mixing machine (SKH-40CA, Misugi Ltd.).

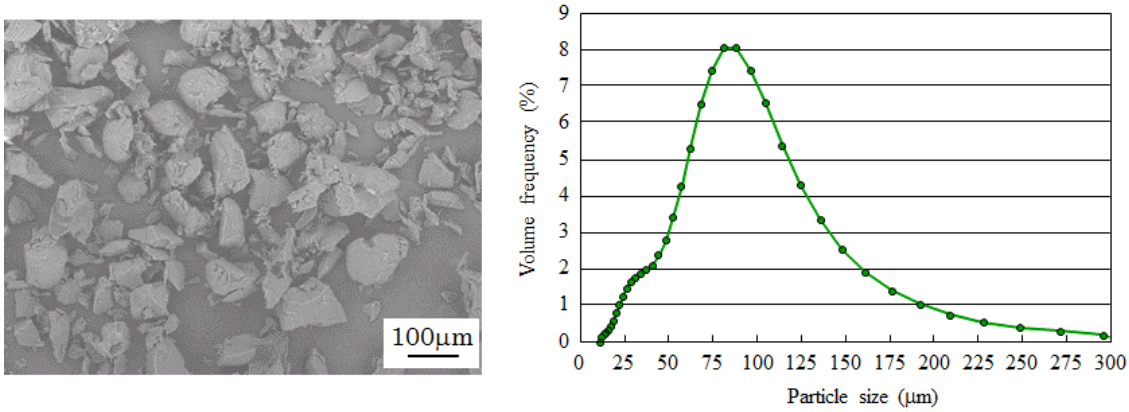

Fig. 1: (a) SEM image and (b) particle-size distribution of cPBT powder.

Selective laser sintering (SLS)

An SLS machine (RaFaEl 300, Aspect Inc.) was used for fabricating the specimens. As for the heat source, a carbon-dioxide laser (with high absorption rate in regard to plastic) with spot diameter of about 0.3 mm was used. As for the SLS process, the parameters that influence quality (including mechanical properties) are laser power, scan rate, scan spacing, powder-bed temperature, feed temperature, and layer thickness [2]. The conditions under which laser AM was performed are listed in Table 1. Taken as the parameter used in this study, laser energy density was varied as four values, namely, 6.7, 14.7, 26.7, and 40.0 kJ/m^2 by changing laser power. In consideration of obtaining a differential-scanning-calorimetry (DSC) thermogram of cPBT powder, powder-bed temperature was taken as 190 or 193 °C, and feed temperature was taken as 165 °C. As for laser-scanning direction, it was supposed that it differs for each layer (with thickness of 0.1 mm).

Table 1: Processing parameters for SLS of cPBT powder.

Processing parameters	
Wavelength	10.6 μm
Laser beam diameter	0.3 mm
Fill and outline laser power	5, 11, 20, 30 W
Scan speed	5.0 m/s
Scan spacing	0.15 mm
Fill energy density	6.7, 14.7, 26.7, 40.0 kJ/m^2
Laser scan direction	Alternating bi-directional scan
Powder bed temp.	190 °C
Feed temp.	165 °C
Layer thickness	0.1 mm
Part piston temp.	180 °C

Injection molding (IM)

Before being injection molded, cPBT pellets were dried for 4 hours at 140 °C. The IM specimens were prepared by injection molding (S-2000i 50A, Fanuc Corporation),

and the dimensions of the test specimens formed by IM and SLS were assumed to be the same. As for the IM, nozzle temperature was 245 °C, cylinder temperature was 240 °C, tool temperature was 80 °C, injection pressure was 25 MPa, injection speed was 20 mm/s, and screw revolution rate was 120 rpm.

2-2-2. Evaluation methods

Powder flowability

Since the cPBT used in this study was powdered by cryomilling, the shape of the powder particles is more angular and irregular shapes than that of PA12 [9]. The angular and irregular shape of the individual cPBT powder particles is related to poor powder flowability due to their natural orientation to interlock with each other, increase the number of adhesive bonds, and resist free flowing. In effect, mechanical interlocking of grains leads to the formation of caking, arches, and voids inside the bulk, which in turn lead to cohesive behaviour and higher shear stresses. In the case of SLS, flowability of the powder significantly affects porosity and mechanical properties [20]. Flowability of the cPBT powders with or without added silica was evaluated in terms of Hausner ratio (HR), which is given as [21]:

$$\mathrm{HR} = \frac{\rho_{tapped}}{\rho_{bulk}} \tag{1}$$

where ρ_{tapped} is tapped density, and ρ_{bulk} is bulk density. and were measured by powder-characteristics tester (PT-X, Hosokawa Micron Corporation).

Scanning electron microscopy (SEM)

The surface of the cPBT powders with or without added silica have been characterized by SEM (JSM-7000F, JEOL, Ltd.) with acceleration voltage taken as 15 kV.

Differential scanning calorimetry (DSC)

DSC (Q2000, TA Instruments) was used to determine melting points, degrees of crystallinity, and crystallization temperatures of the cPBT pellets, cPBT powder, and SLS and IM specimens. Degree of crystallinity (χ) is given by the ratio of the heat of fusion (ΔH) of the specimen divided by its perfect-crystal heat of fusion (ΔH_m^o) as follows [21]:

$$\chi(\%) = \frac{\Delta H}{\Delta H_m^o} \times 100 \quad (2)$$

where ΔH_m^o of PBT was taken as 145.5 J/g in this study [22,23].

The SLS and IM specimens were cut from the central portion of flexural test pieces. The DSC specimens (with assumed weight of 5 ± 0.5 mg) were measured under a temperature increase from 5 to 300 °C at a rate of 10 °C/min and nitrogen flow rate of 40 ml/min. Moreover, isothermal crystallization DSC (EXSTAR 6000, Seiko Instruments Inc.) was performed. The cPBT pellets and powder were heated to 250 °C and held for 5 min, cooled, and when the temperature reached 190 °C, the heat of crystallization was measured at each time. Relative crystallization speed was estimated as the ratio of the heat of crystallization at each time divided by the 100 % of the heat of crystallization.

Optical microscopy

Polarization microscopy (LV100POL, Nikon Corporation) was used to investigate the morphology of the cPBT pellets, cPBT powder, and SLS and IM specimens. The cPBT pellets and cPBT powder were observed in a state in which they were spread on a glass plate, heated to a temperature of 250 °C, cooled, held at 190 °C for 60 min, and allowed to cool to 25 °C. In the case of the SLS and IM specimens, their central portions (10 × 4 mm) were cut in the direction of lamination thickness, and pieces with thickness of 3 to 4 μm were prepared by microtome. The thin pieces were observed by polarization microscopy.

To evaluate porosity ratio of the test specimens, the central portions of the SLS and IM specimens were cut in the same direction as the previously mentioned specimens, and after embedding the specimens in epoxy resin, near-center portions of the SLS and IM specimens were polished at intervals of 0.5 mm, and observed by microscope (VHX-2000, Keyence Corporation). After that, porosity ratio was calculated by image processing (WinROOF, Mitani Corporation). The number of calculations of porosity ratio was taken as five cross-sections of each specimen under each condition.

X-ray diffraction(XRD)

Wide-angle XRD (D8 Advance, Bruker AXS GmbH) was used for structural analysis of the cPBT pellets and cPBT powder. The analysis conditions were as follows: CuKα radiation as the X-ray source; scan range 2θ from 5 ° to 60 °; step width of 0.02 °; and scan time of 1 s for each step.

Inductively coupled plasma-mass spectrometry (ICP-MS)

ICP-MS was performed to estimate contamination of the cPBT pellets and powder. As pre-processing, the cPBT pellets or powder (about 3 mg) were heated from 250 to

430 °C gradually for 2 hours, and the specimens was kept at 430 °C for 12 hours to degrade them by thermal decomposition. Mixed acid (50 % hydrochloric acid + 50 % nitric acid) was added to the thermally degraded specimens, which were further heated at 80 to 100 °C for 1.5 hours for washing. The specimens were then diluted with 5 ml of water and subjected to ICP-MS (7700x, Agilent Technologies) under the following conditions: RF power of 1550 W, argon-gas flow rate of 15 L/min, argon sub-gas flow rate of 0.9 L/min, helium option-gas flow rate of 4.3 mL/min, time for integral calculus of 0.33 s/point (repeated three times), and a standard solution of Merck KGaA Single-Element Standard for ICP. Lower limit of quantification (LOQ) was determined as 10 times the standard deviation of blank.

Mechanical testing

To evaluate the mechanical properties of the SLS and IM specimens, tensile tests, flexural tests, and Charpy impact-strength tests were performed. The tensile-testing specimens were taken as “type A” specified in ISO3167; 1993 (total length: 170 mm; parallel-portion length: 80 mm; thickness: 4 mm). As for the tensile tests (5500RF, Instron Corporation), performed according to ISO527-1, -2; 2012, testing speed was 50 mm/min, and distance between clamps was 115 mm. As for the flexural tests (5500RF, Instron Corporation), performed according to ISO178; 2001, with test-specimen size of 80 × 10 × 4 mm, testing speed was 2 mm/min, and the distance between the fulcrums was 64 mm. As for the Charpy-impact-strength tests (AG-100kNX, Shimazu Corporation), performed in accordance with ISO179-1; 2010, a notch was formed in a test specimen with the same shape as the flexural-test specimens. With an energy of 0.5 J, the hammer weight was applied so that the impact was in the edgewise direction. All the strength tests were performed with n=5 (minimum).

Dynamic mechanical analysis (DMA)

The sizes of the SLS and IM specimens, measured by DMA (Rheogel-E4000, UBM Corporation), were 20 × 5 × 1 mm, and the measurement frequency was 1 Hz. The temperature range was 25 to 125 °C, and the rate of temperature increase was 5 °C/min. From the DMA analysis, storage elastic modulus (E'), loss elastic modulus (E"), and a loss factor (tan δ=E'/E") were obtained.

Gel-permeation chromatography (GPC)

The molecular-weight distributions of the cPBT powder and SLS and IM specimens were determined by GPC (HLC-8220GPC, Tosoh Corporation). As for the SLS and IM specimens, a specimen cut from the central portion of the flexural-test specimen was used. The eluent was hexafluoroisopropanol containing 10 mM of sodium trifluoroacetate. Flow velocity was 0.3 mL/min, column temperature was set to 40 °C, specimen concentration was 1 mg/mL, and specimen-injection volume was 20 μL. For the standard polymer, poly(methyl methacrylate) (PMMA) was used, so the obtainable molecular weight of cPBT is the "PMMA-converted molecular weight."

2-3. Results and discussion

2-3-1. Powder characteristics

Powder flowability

HR values are plotted in Fig. 2 with amount of silica added to cPBT used as a parameter. SEM images of the powder surface of (a) cPBT, (b) cPBT with 0.05 wt% added silica, (c) cPBT with 0.1-wt% added silica, (d) cPBT with 0.2-wt% added silica,

and (e) cPBT with 0.5-wt% added silica, and (f) cPBT with 1.0-wt% added silica are shown in Fig. 3.

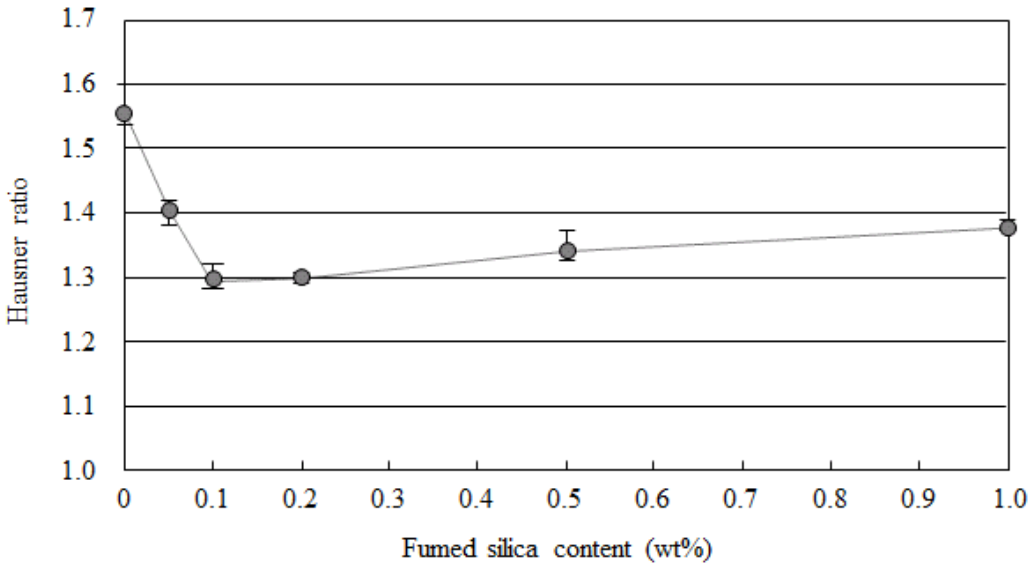

Fig. 2: HR of cPBT with amount of fumed silica content as a parameter.

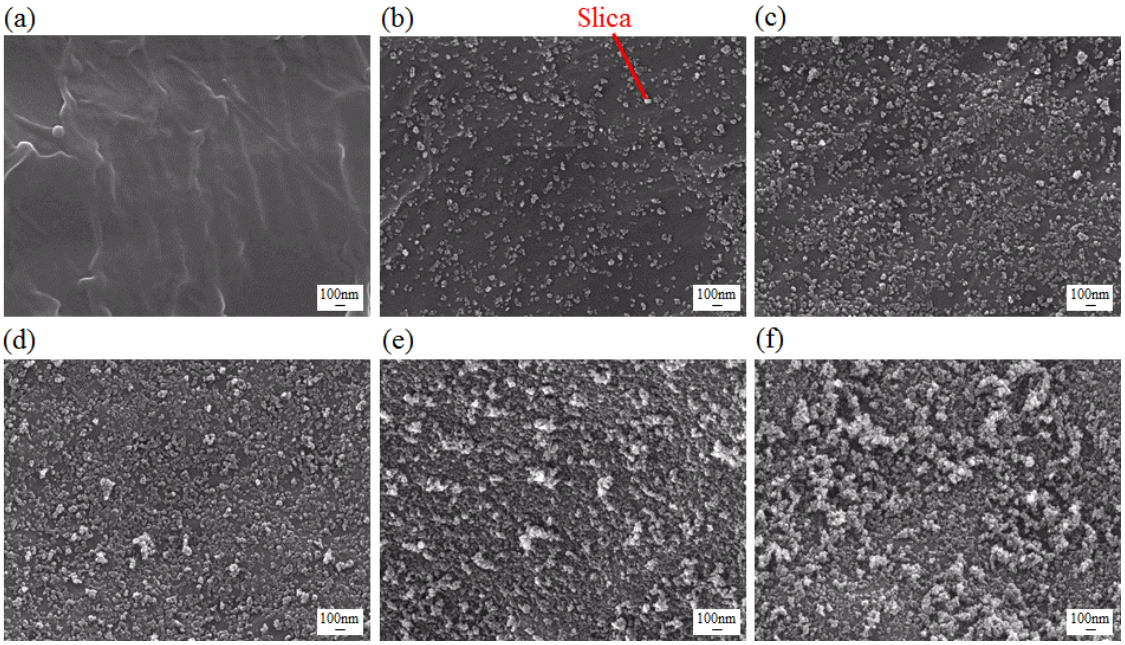

Fig. 3: SEM images of fracture surfaces of SLS specimens: (a) cPBT, (b) cPBT with 0.05-wt% added silica, (c) cPBT with 0.1-wt% added silica, (d) cPBT with 0.2-wt% added silica, and (e) cPBT with 0.5-wt% added silica, and (f) cPBT with 1.0-wt% added silica.

When silica is added in amounts in the range of 0.1 wt%, HR reaches its minimum value. Furthermore, the SEM-observation results confirm that when the amount of silica addition was 0.1 wt%, aggregation of silica was scarce, and silica was uniformly adhered to cPBT; in contrast, when it was 0.2 wt% or more, aggregation of silica was abundant. Reporting a similar result, Schmidt [11] et al. showed that adding 0.1 wt% of hydrophobic silica to PBT improved its flowability. Therefore, this trend is presumed to be due to the fact that as the amount of silica increases, the silica particles tend to aggregate easily, so adhesion between the cPBT-powder grains increases and flowability is degraded.

Crystallization characteristics

The results of the DSC evaluation of pellets, powder, and powder with 0.1-wt% additions of fumed silica (hydrophobic fumed silica) are shown in Fig. 4: (a) heating curves (b) cooling curves.

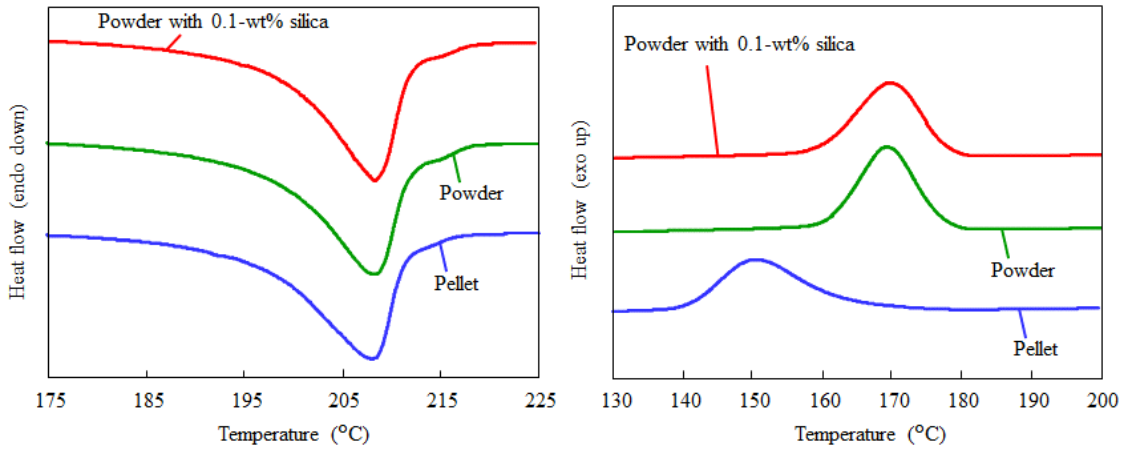

Fig. 4: Results of DSC evaluation of pellets, powder, and powder with 0.1-wt% addition of fumed silica: (a) heating curves and (b) cooling curves.

As for the pellets and powder, although their melting points hardly differ, crystallization temperature with regard to cooling of the powder is 19.0 °C higher than

that with regard to cooling of the pellets. As for the powder, melting point and crystallization temperature hardly differ after 0.1-wt% additions of fumed silica. In regard to homo-PBT, the same trend as that for cPBT was confirmed, namely, powder-crystallization temperature was 194.3 °C, i.e., 12.9 °C higher than that of the pellets, but the melting point was the same, i.e., 223.5 °C. Moreover, evaluated crystallization rate of the cPBT pellets, powder, and powder with 0.1-wt% addition of fumed silica at 190 °C (i.e., 17.5 °C below the melting point) is plotted in Fig. 5. This plot of cPBT clearly shows that the crystallization rate of the cPBT powder is much higher than that of the cPBT pellets. In Fig. 5, the data for pulverized homo PBT at 206 °C (i.e., 17.5 °C below the melting point) is added. This additional result confirms that even if the difference between melting points is set to the same temperature, crystallization rate of homo PBT is very high, so homo PBT is particularly unsuitable for SLS.

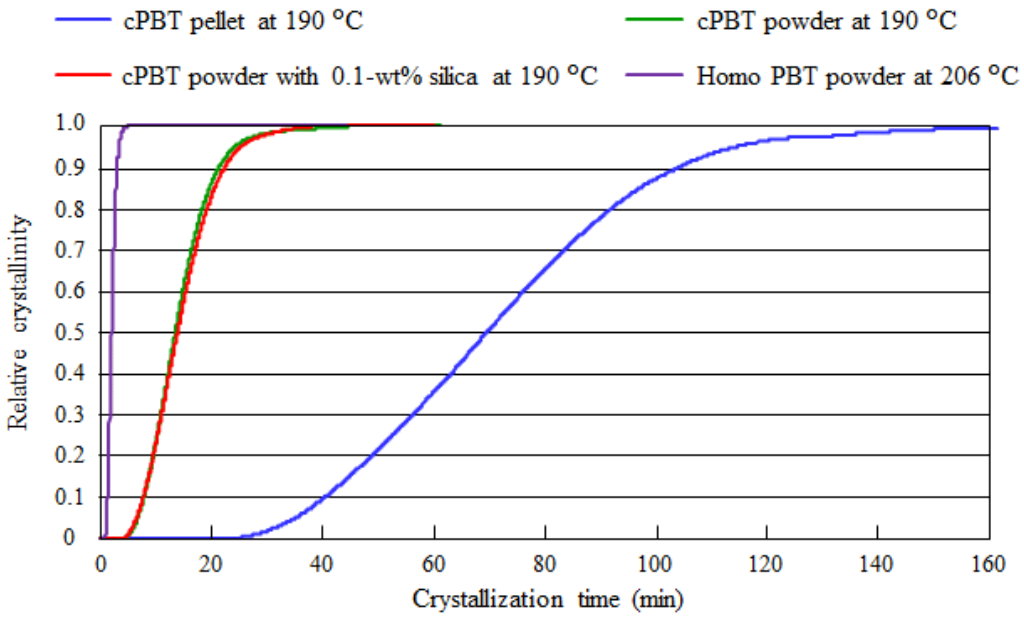

Fig. 5: Crystallization rate of cPBT pellets, cPBT powder, and cPBT powder with 0.1-wt% addition of fumed silica at 190 °C and of homo-PBT powder at 206 °C.

Crystal modification

PBT is well known to exist in two crystalline forms (α and β) [24-26]. In particular, β form is generated under tension, and the basic form is known as α [25, 26]. According to Schmidt et al. [10], the crystallization temperature of PBT products pulverized by combining dry grinding and wet grinding is larger than that of pellets, and formation of different crystalline polymorphs has been reported as the cause of that higher crystallization temperature. Accordingly, cPBT pellets and powder were evaluated by XRD, and the evaluation results are shown in Fig. 6.

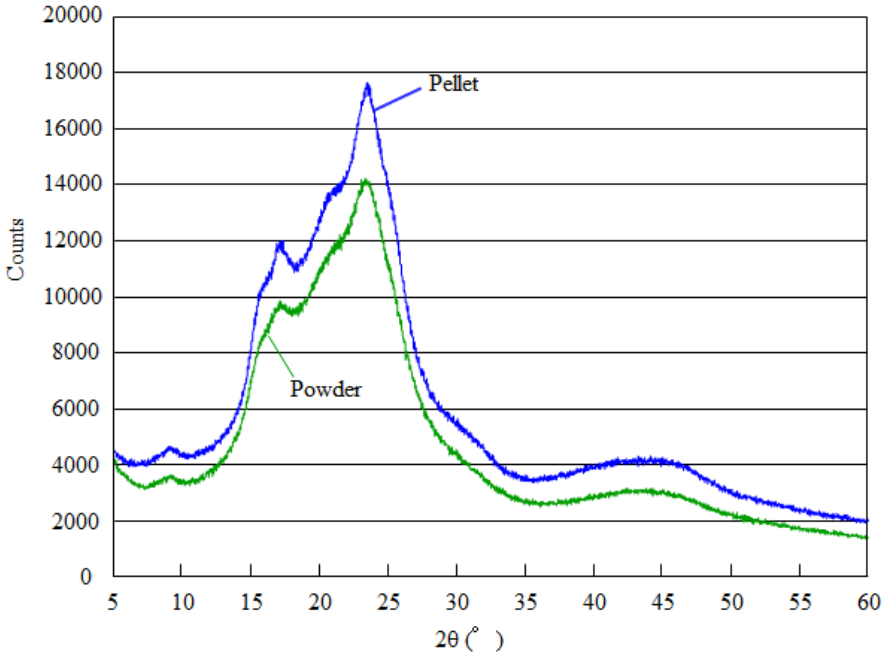

Fig. 6: XRD patterns of cPBT pellets and powder.

The XRD patterns of the pellets and powder do not significantly differ, and both indicate typical α form; in particular, the 2θ peak at 28.0° [25, 26] characteristic of β form could not be confirmed. This result confirms that the change in the crystal structure is not the cause of the increase in crystallization temperature of the powder after low-temperature pulverization. Moreover, as for DSC evaluation as well, a similar

result was obtained even after the heating and cooling were repeated once or twice. It is therefore concluded that the structural change of crystalline form was not caused by cryomilling.

Spherulite size

Polarization-microscope images of the pellets, powder, and powder with 0.1-wt% addition of fumed silica cooled to 25 °C after temperature crystallization (in which the pellets and powder were heated to 250 °C, cooled, and held at 190 °C for 60 min) are shown in Fig. 7 [(a) pellets, (b) powder, and (c) powder with 0.1-wt% addition of fumed silica]. As for the images of the powder, much finer spherulites can be seen compared to the images of the pellets. However, after addition of 0.1-wt% fumed silica, the sizes of the spherulites hardly differ.

Fig. 7: Polarization-microscope images of pellets and powder obtained at RT after temperature crystallization at 190 °C for 60 min: (a) pellets and (b) powder (c) powder with 0.1-wt% addition of fumed silica.

In the case of SLS, it is known that the wide process window is a significant advantage [2]; however, as for the powder formed by cryomilling, the results presented here show that the process window gets smaller (i.e., crystallization temperature is increased). On the contrary, the results also confirm that the addition of 0.1-wt% fumed

silica to powder formed by pulverization does not affect the change in crystallization temperature. However, it has been reported that the crystallization temperature of PA12 powder is increased by adding clays [27], nanotubes [28], or graphite nanoplatelets [21].

Contaminants

Transforming cPBT into powder involves pulverization by pin mill. As for cryomilling, it is supposed that some kinds of blended compound act as a nucleating agent for crystallization. In this experiment, all the main parts of the pin mill (including the pin disk) were made of stainless steel (SUS304). The ICP-MS measurement results for the pellets and powder (in regard to the iron, chromium, and nickel constituents of SUS304) are listed in Table 2. It is clear that the proportions of all three elements in the powder are higher than those in the pellets. In particular, the content of iron (which is the most abundant constituent of SUS304) is about 30 times or more than those of the other constituents (chromium and nickel). In addition, it is suggested that during the mill pulverization, fine metal particles shaved off the blade are mixed into the powder. As reported by Zhu et al. [29], contaminants produced during low-temperature pulverization act as nucleating agents in poly(ethylene terephthalate) resin (which is similar to PBT).

Table 2: ICP-MS evaluation of cPBT pellets and powder.

	ppb (ng/g)		
Element	Fe	Cr	Ni
Pellet	69	31	11
Powder	2,087	124	76

* LOQ of Fe, Cr, and Ni were 41, 39, and 41 ppb, respectively.

It is clear from the results presented here that despite the fact that the amount of added fumed silica is considerably higher than the amount of mixed metal contaminants due to mill pulverization, the crystallization temperature does not change. Accordingly, it is assumed that the capability of increasing the crystallization temperature depends greatly on the material quality of the fine particles that are found to exist.

2-3-2. Characteristics of laser sintered and injection molded specimens

In the case of SLS, it is necessary to adjust the powder-bed temperature in terms of mechanical properties and accuracy [2,30]. The external appearance of the powder bed during SLS processing is shown in Fig. 8. The tensile-test specimens during processing under powder-bed temperatures of (a) 193 °C and (b) 190 °C are shown in photos (a) and (b), respectively.

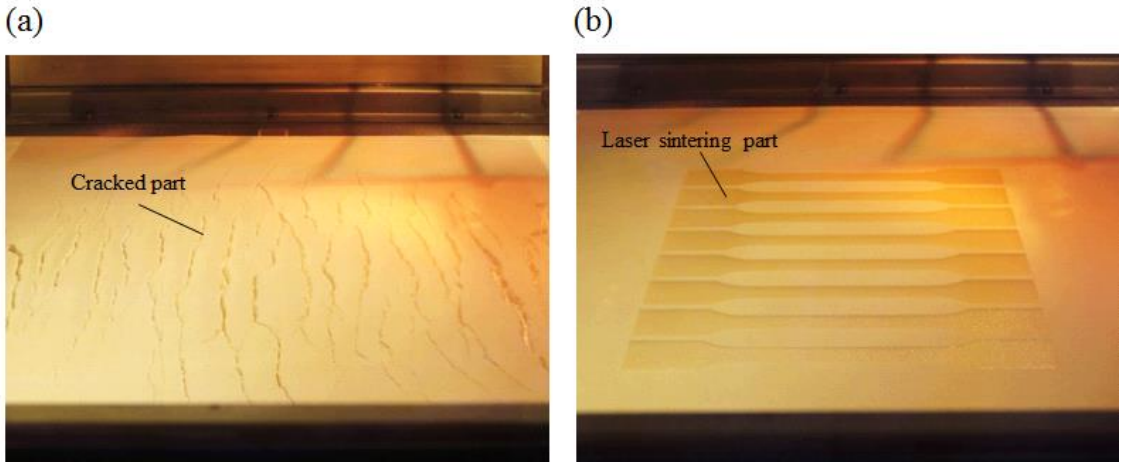

Fig. 8: External appearance of the powder bed during SLS processing: powder-bed temperature (a) 193 °C and (b) 190 °C.

When the powder-bed temperature was 193 °C, when the powder was spread out by a roller, the powder particles agglomerated, and considerable cracking occurred. Consequently, the SLS process was interrupted before laser irradiation. In contrast,

when the powder-bed temperature was 190 °C, the powder was spread by the roller uniformly, and the specimens could be sintered correctly.

Mechanical properties

Tensile properties of the IM specimen and SLS specimens formed under several laser-energy densities are compared in Fig. 9: (a) tensile strength, (b) elongation at break, and (c) stress-strain curves. All the plotted stress-strain curves are close to the average data. In the case of the SLS specimens, all tensile properties are maximized when laser-energy density is 14.7 kJ/m^2. When laser-energy density is increased beyond that value, the mechanical properties are deteriorated. The IM specimen has higher tensile properties, particularly higher toughness and ductility, than the SLS specimens.

Flexural strength and Charpy impact strength of the IM specimen and SLS specimens formed under several laser-energy densities are compared in Figs. 10 and 11. As with tensile properties, flexural strength and Charpy impact strength of the SLS specimens are maximized at laser-energy densities of 14.7 kJ/m^2, but they are lower than those of the IM specimen. As reported by Athreya et al. [31], in the case PA12 is used, tensile strength and flexural strength of SLS specimens are higher than those of IM specimens. In contrast, tensile strength and flexural strength of SLS specimens made of cPBT are lower than those of injection-molded specimens made of cPBT. According to Goodridge et al. [2], as for powder formed by pulverization, mechanical properties of sintered parts are deteriorated in comparison to those of parts formed by polymerization. Moreover, according to Ziegelmeier et al. [32], flowability of a powder has a significant effect on tensile strength. The cPBT powder with 0.1-wt% addition of fumed silica used for SLS in the present study has a higher HR (1.30) than those of other commercial

products [20,32]. Therefore, it is possible that the reason for the lower tensile properties and flexural strength of injection-molded specimens is that the flowability of powder has a significant effect on those properties. Moreover, in contrast with the IM specimen, the SLS specimens showed notably lower Charpy impact strength and elongation at break in the same manner as the results reported for PA12 [21,33].

The DMA results for the IM specimen and SLS specimens under four assumed laser-energy densities are shown in Fig. 12: (a) storage elastic modulus and (b) tan δ. In the case of the SLS specimens, the order of the magnitudes of the storage elastic modulus is the same as the order of the evaluation results for mechanical properties. In the case of the IM specimen, although the elastic storage modulus is larger than that in the case of the smallest laser energy density, it is lower than those in the cases of the other laser energy densities (14.7, 26.7, and 40.0 kJ/m^2). Moreover, as for the SLS specimens, the storage elastic modulus is decreased at high temperature, and the value of tan δ at high temperature, shown in Fig. 12(b), is high. When IM and SLS products are compared, even in the case of PA12 (which has good flowability), the SLS product has a higher porosity ratio [34]. Moreover, as for IM and SLS, since the molding processes differ significantly, the influences of crystallization characteristics also differ [35]. Hereafter, the evaluation results concerning the porosity and crystallinity are presented and discussed in detail.

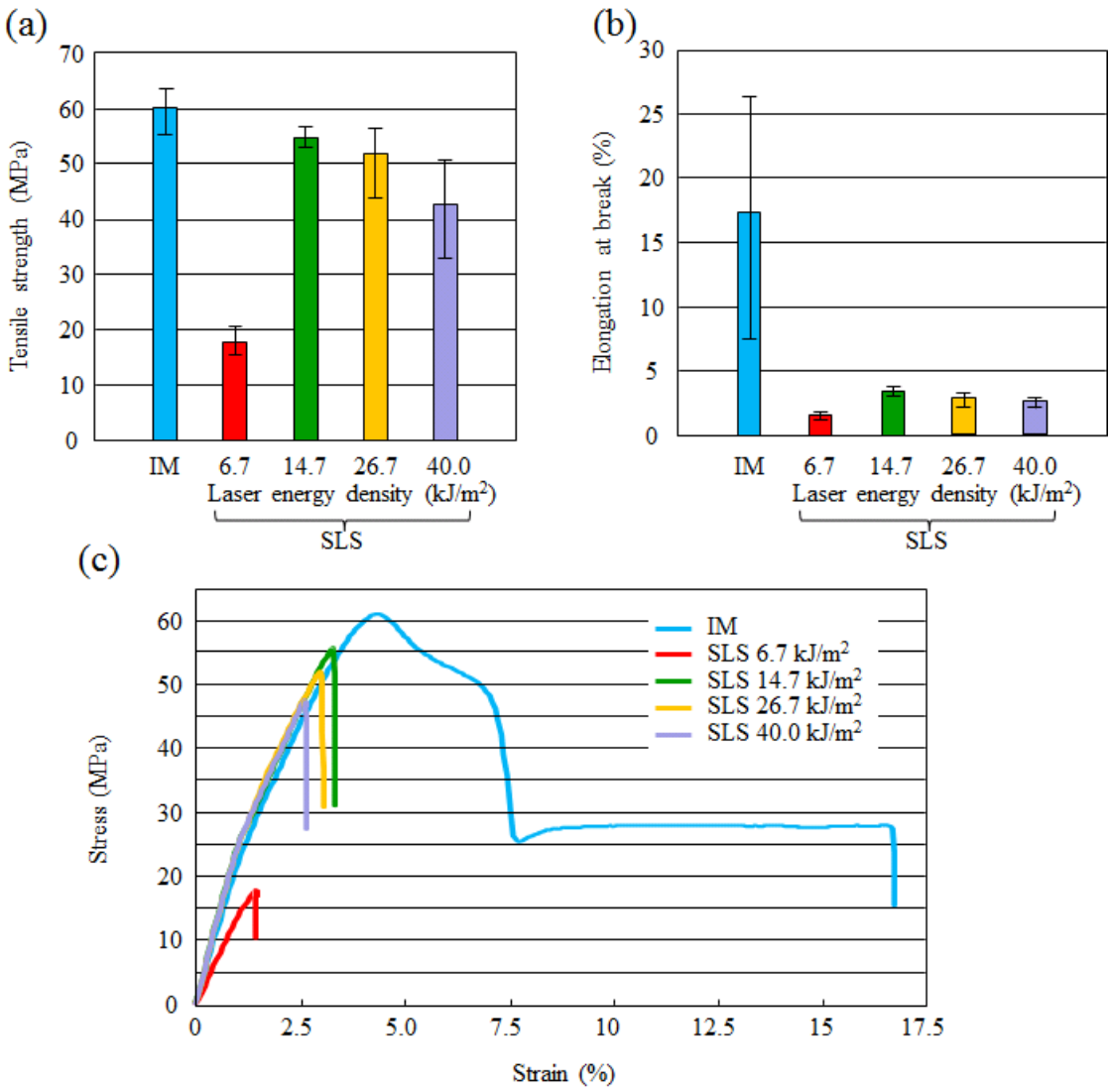

Fig. 9: Comparison of tensile properties of IM specimen and SLS specimens under assumed laser-energy densities of 6.7, 14.7, 26.7, and 40.0 kJ/m^2: (a) tensile strength, (b) elongation at break and (c) stress-strain curves.

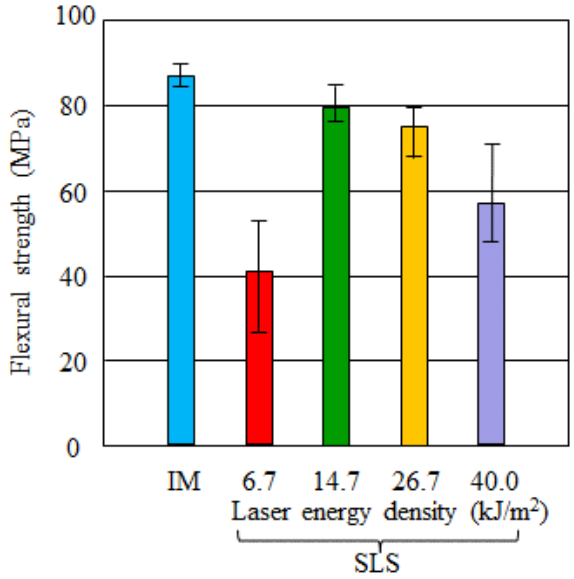

Fig. 10: Comparison of flexural strength of IM specimen and SLS specimens under assumed laser-energy densities of 6.7, 14.7, 26.7, and 40.0 kJ/m².

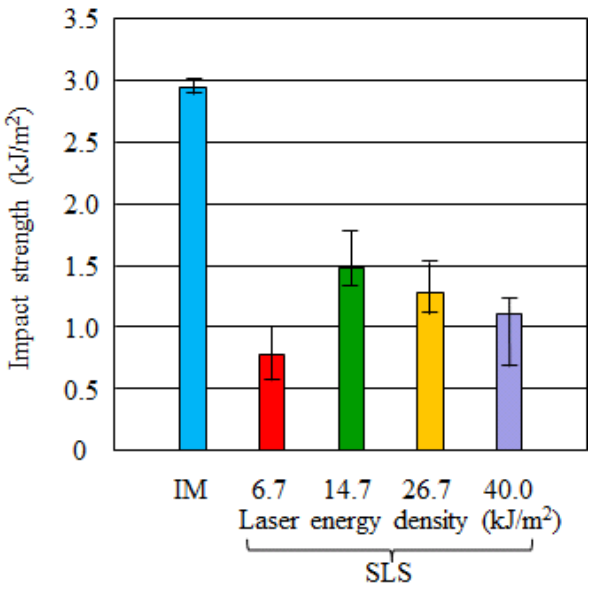

Fig. 11: Comparison of Charpy impact strength of IM specimen and SLS specimens under assumed laser-energy densities of 6.7, 14.7, 26.7, and 40.0 kJ/m².

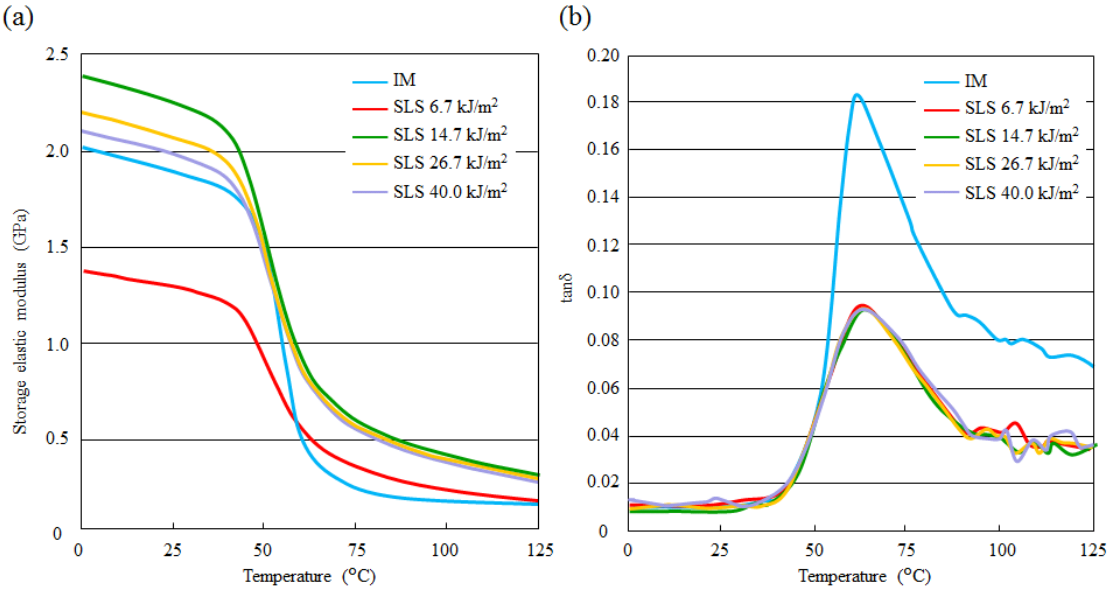

Fig. 12: DMA results for IM specimen and SLS specimens under assumed laser energy densities of 6.7, 14.7, 26.7, and 40.0 kJ/m^2: (a) storage elastic modulus and (b) tan δ.

Porosity ratio

Estimated porosities of the IM specimen and SLS specimens (formed under the 4 laser-energy densities), determined by image processing of cross-sectional images of the specimens, are compared in Fig. 13.

	IM	SLS			
		6.7 kJ/m^2	14.7 kJ/m^2	26.7 kJ/m^2	40.0 kJ/m^2
Before image analysis					
After image analysis	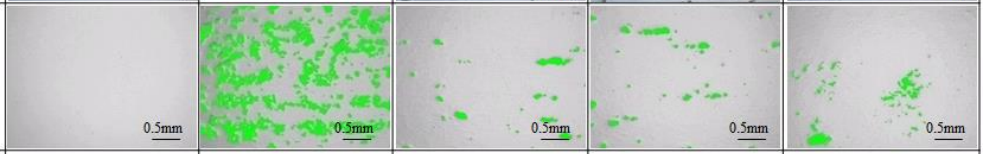				
Average porosity ratio (%)	0	20.8	1.74	1.92	1.94

Fig. 13: Comparison of porosities of IM specimen and SLS specimens under laser energy densities of 6.7, 14.7, 26.7, and 40.0 kJ/m^2.

As for the IM specimen, no porosity can be seen; in contrast, as for the SLS specimens, a constant amount of porosity is seen in all specimens under all sintered conditions. This result agrees with that reported by Zarringhalam et al. [36]. As for the SLS specimens, particularly, when laser energy density is 6.7 kJ/m^2, a considerable amount of the porosity remains. This result suggests that insufficient cPBT resin melts and is sintered in a state in which the viscosity has become high. Accordingly, the proportion of "open" porosity among the total porosity gets bigger. When the laser energy density is 14.7 kJ/m^2 (which produces the highest mechanical properties), the porosity ratio is low. The relation between porosity ratio and mechanical properties is the same as the results reported for PA12 [35]. However, porosity ratio when laser energy density is 14.7 kJ/m^2 does not appear to differ notably from those for 26.7 and 40.0 kJ/m^2. Accordingly, porosity is not considered the main cause of the noticeable difference in mechanical properties in the case of laser energy densities of 14.7 and 40.0 kJ/m^2. The assumed reason is discussed in the following subsection.

Molecular weight

Caulfield et al. [37] and Vasquez et al. [38] suggested that in the case of SLS, plastic degrades when laser energy density increases. Results of GPC evaluation in the case of laser-energy densities of 14.7 and 40.0 kJ/m^2 are listed in Table 3.

Table 3: Results of molecular-weight evaluation for pellets, powder, IM specimen, and SLS specimen.

	Mn ($\times 10^3$)	Mw ($\times 10^4$)	Mw/Mn
Pellet	9.03	2.45	2.71
Powder	9.13	2.49	2.76
IM	8.95	2.42	2.70
SLS 14.7 kJ/m^2	9.89	2.72	2.75
SLS 40.0 kJ/m^2	6.88	2.18	3.17

Comparing the SLS specimens formed under laser-energy densities of 14.7 and 40.0 kJ/m^2 reveals that the specimen sintered under laser-energy density of 40.0 kJ/m^2 has a lower molecular weight. It is thus suggested that thermal degradation of the upper part of the layer during laser irradiation is the main cause of the deterioration of mechanical properties under increasing laser-energy density. The results of the molecular-weight evaluation of the pellets, powder, IM specimen, and SLS specimen sintered at laser-energy density of 14.7 kJ/m^2 are also listed in Table 3. The IM specimen has a comparable molecular weight to those of the pellets and powder. Moreover, the SLS specimen sintered at laser-energy density of 14.7 kJ/m^2 has a higher molecular weight than that of the IM specimen. This result implies that cross-linking in the SLS specimen is more progressed (because the SLS specimen has a longer thermal history). It is thus clear that thermal degradation does not occur in the SLS process with appropriate laser-energy density.

Crystallization characteristics

Polarization-microscopy images of the IM specimen and the SLS specimen (sintered under laser energy of 14.7 kJ/m^2, which is the optimum formation condition used in this study) are shown in Fig. 14.

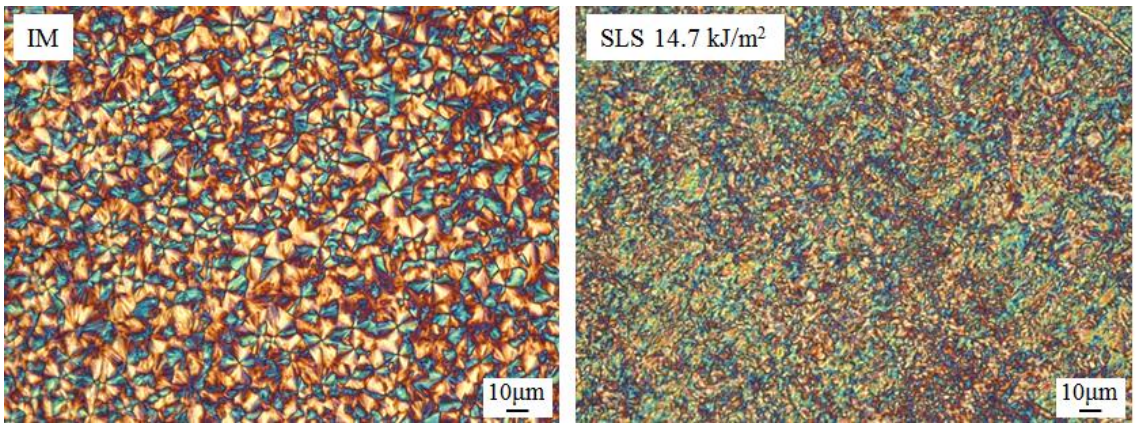

Fig. 14: Polarization-microscopy images of IM specimen and SLS specimen under laser energy density of 14.7 kJ/m2 (optimum formation condition).

It is clear from these images that the IM specimen features large spherulites, while the SLS specimen features fine spherulites. In the case of PA12, when the IM specimen and SLS specimen are compared, it has been reported that the spherulites get smaller because the cooling rate of IM is higher [31,36]. In contrast to that report, the images in Fig. 14 show the opposite trend. As for the reason for this discrepancy with reported results, in the case of the SLS specimen used in the present study, it is supposed that the metallic contaminants in the cPBT powder (such as iron) act as nucleating agents. The evaluated degrees of crystallinity of the pellets, powder with 0.1-wt% addition of fumed silica, IM specimen, and SLS specimen sintered under laser energy of 14.7 kJ/m^2 are listed in Table 4. As clear from Table 4, the degree of crystallinity of the SLS specimen is higher than that of the IM specimen. This result—indicating that degree of crystallinity depends on the process used—agrees with that reported by Karevan et al.

[21] and Hooreweder et al. [39]. Although the SLS specimen has a higher porosity ratio than that of the IM specimen, it can be supposed that its elastic modulus is increased by its higher degree of crystallinity. As for strength, the influence of porosity is predominant; thus, it is supposed that the IM specimen has a higher strength than that of the SLS specimen.

Table 4: Results of comparison of degrees of crystallinity of pellets, powder with 0.1-wt% addition of fumed silica, IM specimen, and SLS specimen under laser energy density of 14.7 kJ/m^2 (optimum formation condition).

	Fumed silicas	Tm (°C)	Tc (°C)	Degee of Crystallinity (%)
Pellet	None	207.5	150.7	30.8
Powder	0.1-wt%	207.5	169.7	32.8
IM	None	207.9	168.9	27.1
SLS 14.7 kJ/mm^2	0.1-wt%	209.9	169.0	34.8

2-4. Conclusions

In the case of powder made from cPBT pellets pulverized at low temperature, it was revealed that although melting point, crystalline form and molecular weight are unchanged by cryomilling, contaminants produced during the pulverization act as nucleating agents of cPBT, which increase the crystallization temperature of cPBT powder. As a result, the process window gets narrower. On the other hand, even though a greater amount of fumed silica (added to improve flowability) in relation to the contaminants was added, it does not become a nucleating agent in cPBT powder.

As for SLS using cPBT powder (melting point: 207.5 °C; crystallization temperature: 169.7 °C), it was confirmed that SLS is possible by setting the powder-bed temperature to 190 °C. The mechanical properties of the SLS specimen (namely, tensile strength of 54.9 MPa, elongation at break of 3.41 %, flexural strength of 79.5 MPa, notched Charpy impact strength of 1.63 kJ/m^2, and storage elastic modulus of 2.39 GPa) are maximized under the SLS processing conditions that give the lowest porosity. In comparison with the IM specimen, however, the SLS specimen shows lower values of mechanical properties (except storage elastic modulus). This result is supposed to be due to the fact that degree of crystallinity (which differs in the case of IM and SLS) is the main factor affecting elastic modulus; in contrast, porosity (the amount of which depends on flowability of the powder) has a considerable effect on tensile strength, elongation at break, flexural strength, and notched Charpy impact strength. Moreover, in the case of SLS with cPBT powder used in the present study, finer spherulites than those of the IM specimen (due to the nucleating effect of contaminants generated during sintering) were observed.

References

[1] A.J. Pinkerton, Lasers in additive manufacturing, Opt. Laser Technol. 78 (2016) 25–32.

[2] R.D. Goodridge, C.J. Tuck, R.J.M. Hague, Laser sintering of polyamides and other polymers, Prog. Mater. Sci. 57 (2012) 229–267.

[3] M.M. Savalani, L. Hao, R.A. Harris, Evaluation of CO2 and Nd:YAG lasers for the selective laser sintering of HAPEX, Proc. Inst. Mech. Eng. Part B-J. Eng. Manuf. 220 (2006) 171–182.

[4] R.D Goodridge, R.J.M. Hague, C.J. Tuck, An empirical study into laser sintering of ultra-high molecular weight polyethylene (UHMWPE). J. Mater. Process. Technol., 210 (2010) 72–80.

[5] L. Fiedler, L.O. Garcia Correa, H.J. Radusch, A. Wutzler, J. Gerken, Evaluation of polypropylene powder grades in consideration of laser sintering processibility, J. Plast. Technol. 3 (2007) 1–14.

[6] W. Zhu, C. Yan, Y. Shi, S. Wen, J. Liu, Y. Shi, Investigation into mechanical and microstructural properties of polypropylene manufactured by selective laser sintering in comparison with injection molding counterparts. Mater. Des. 82 (2015) 37-45.

[7] D. Drummer, D. Rietzel, F. Künlein. Development of a characterization approach for the sintering behavior of new thermoplastics for selective laser sintering, Phys. Procedia 5 (2010) 533–542.

[8] W. Zhou, X. Wang, J. Hu, X. Zhu, Melting process and mechanics on laser sintering of single layer polyamide 6 powder, Int. J. Adv. Manuf. Technol. 69 (2013) 901–908.

[9] L. Verbelen, S. Dadbakhsh, M. Van den Eynde, J.-P. Kruth, B. Goderis, P. Van Puyvelde, Characterization of polyamide powders for determination of laser sintering processability, Eur. Polym. J. 75 (2016) 163–174.

[10] J. Schmidt, M. Sachs, M. Zhao, S. Fanselow, K. Wudy, M. D. D. Drummer, K. E. Wirth, W. Peukert. A novel process for production of spherical PBT powders and their processing behavior during laser beam melting, AIP Conf. Proc. 1713, 14008, (2016) 1-8.

[11] J. Schmidt, M. Sachs, S. Fanselow, M. Zhao, S. Romeis, D. Drummer, K. E. Wirth, W. Peukert. Optimized polybutylene terephthalate powders for selective laser beam melting, Chem. Eng. Sci. 156 (2016) 1-10.

[12] O.R. Ghita, E. James, R. Davies, S. Berretta, B. Singh, S. Flint, K.E. Evans. High temperature laser sintering (HT-LS): an investigation into mechanical properties and shrinkage characteristics of poly (ether ketone) (PEK) structures, Mater. Des. 61 (2014) 124–132.

[13] O.R. Ghita, E. James, R. Trimble, K.E. Evans, Physico-chemical behaviour of poly (ether ketone) (PEK) in high temperature laser sintering (HT-LS), J. Mater. Process. Technol. 214 (2014) 969–978.

[14] Y. Wang, D. Rouholamin, R. Davies, O.R. Ghita. Powder characteristics, microstructure and properties of graphite platelet reinforced Poly Ether Ether Ketone composites in High Temperature Laser Sintering (HT-LS), Mater. Des. 88 (2015) 1310–1320.

[15] S. Berretta, O. Ghita, K.E. Evans. Morphology of polymeric powders in Laser Sintering (LS): From Polyamide to new PEEK powders, Eur. Polym. J. 59 (2014) 218-229.

[16] L. Finelli, N. Lotti, A. Munari, Crystallization kinetics and melting behavior of poly(butylene isophthalate/terephthalate) random copolyesters, Eur. Polym. J. 37 (2001) 2039-2046.

[17] X. Xiao, Z. Zeng, W. Xue, Q. Kong, W. Zhu, Isothermal crystallization kinetics and melting behaviors of poly(butylene terephthalate) and poly(butylene terephthalate-co-fumarate) copolymer, Polym. Eng. Sci. 53 (2013) 482-490.

[18] R. Pfeffer, R. N. Dave, D. Wei, M. Ramlakhan. Synthesis of engineered particulates with tailored properties using dry particle coating, Powder Technol. 117 (2001) 40-67.

[19] S. Dupin, O. Lame, C. Barrès, J.-Y. Charmeau, Microstructural origin of physical and mechanical properties of polyamide 12 processed by laser sintering, Eur. Polym. J. 48 (2012) 1611–1621.

[20] S. Ziegelmeier, F. Wöllecke, C. Tuck, R. Goodridge, R. Hague, Characterizing the Bulk & Flow Behaviour of LS Polymer Powders. Proc. of the Solid Freeform Fabrications Symp., Austin, TX, (2013) 354–367.

[21] M. Karevan, S. Eshraghi, R. Gerhardt, S. Das, K. Kalaitzidou. Effect of processing method on the properties of multifunctional exfoliated graphite nanoplatelets/polyamide 12 composites, Carbon 64 (2013) 122-131.

[22] F.J. Vallejo, J.I. Eguiazábal, J. Nazábal, Solid state features and mechanical properties of PEI/PBT blends, J. Appl. Polym. Sci. 80 (2001) 885-892.

[23] N. Tomar, S.N. Maiti, Thermal and Crystallization Properties of PBT/ABAS Blends, J. Appl. Polym. Sci. 113 (2009)1657-1663.

[24] M. Yokouchi, Y. Sakakibara, Y. Chatani, H. Tadokoro, T. Tanaka, K. Yoda, Structures of two crystalline forms of poly(buty1ene terephthalate) and reversible transition between them by mechanical deformation, Macromolecules 9 (1976) 266–273.

[25] J. Roebuck, R. Jakeways, I.M. Ward, The existence of a stable β form in oriented poly (butylene terephthalate), Polymer 33 (1992) 227–232.

[26] P.L. Carr, R. Jakeways, J.L. Klein, I.M. Ward, Tensile drawing, morphology, and mechanical properties of poly(butylene terephthalate), J.Polym.Sci.B Polym. Phys. 35 (1997) 2465–2481.

[27] P.K. Jain, P.M. Pandey, P.V.M. Rao, Selective Laser Sintering of Clay-Reinforced Polyamide, Polym. Compos. 31 (2010) 732-734.

[28] J. Bai, R.D. Goodridge, R.J.M. Hague, M. Song, Carbon nanotube reinforced Polyamide 12 nanocomposites for laser sintering, Proc. of the Solid Freeform Fabrications Symp., Austin, TX, (2012) 98-107.

[29] Y. G. Zhu, Z. Q. Li, D. Zhang, T. Tanimoto, Effect of cryomilling on the thermal behaviors of poly(ethylene terephthalate), J. Appl. Polym. Sci. 99 (2006) 2868-2873.

[30] A.E. Tontowi, T.H.C. Childs, Density prediction of crystalline polymer sintered parts at various powder bed temperatures, Rap. Proto. J. 7 (2001) 180-184.

[31] S.R. Athreya, K. Kalaitzidou, S. Das, Mechanical and microstructural properties of Nylon-12/carbon black composites: Selective laser sintering versus melt compounding and injection molding. Compos. Sci. Technol. 71 (2011) 506–510.

[32] S. Ziegelmeier, P. Christou, F. Wöllecke, C. Tuck, R. Goodridge, R. Hague, E. Krampe, E. Wintermantel, An experimental study into the effects of bulk and flow behaviour of laser sintering polymer powders on resulting part properties, J. Mater. Process. Technol. 215 (2015) 239–250.

[33] B.V. Hooreweder, J.P. Kruth, High cycle fatigue properties of selective laser sintered parts in polyamide 12, CIRP Ann. Manuf. Technol. 63 (2014) 241-244.

[34] J.P. Kruth, G. Levy, F. Klocke, T.H.C. Childs. Consolidation phenomena in laser and powder-bed based layered manufacturing, CIRP Ann. Manuf. Technol. 56 (2007) 730-759.

[35] S. Griessbach, R. Lach, W. Grellmann, Structure-property correlations of laser sintered nylon 12 for dynamic dye testing of plastic parts. Polym.Test. 29 (2010) 1026–1030.

[36] H. Zarringhalam, N. Hopkinson, N.F. Kamperman, J.J. de Vlieger, Effects of processing on microstructure and properties of SLS Nylon 12, Mater. Sci. Eng. A 435-436 (2006) 172–180.

[37] B. Caulfield, P.E. McHugh, S. Lohfeld, Dependence of mechanical properties of polyamide components on build parameters in the SLS process, J. Mater. Process. Technol. 182 (2007) 477–488.

[38] M. Vasquez, B. Haworth, N. Hopkinson, Methods for Quantifying the Stable Sintering Region in Laser Sintered Polyamide-12, Polym. Eng. Sci., 53 (2013) 1230-1240.

[39] B. Van Hooreweder, D. Moens, R. Boonen, J.P. Kruth, P. Sas, On the difference in material structure and fatigue properties of nylon specimens produced by injection molding and selective laser sintering, Polym. Test. 32 (2013) 972–981.

Chapter 3

Characterization of flame-retardant laser sintered PBT parts in comparison with injection molded parts

3-1. Introduction

As one method of additive manufacturing (AM), selective laser sintering (SLS) mainly involves three-dimensionally laminating a thin resin powder by repeatedly irradiating the powder with a laser. In contrast to conventional fabrication methods like injection molding (IM), AM methods, including SLS, do not require a mold; accordingly, AM brings advantages such as increased design freedom, easy correspondence with complicated shapes and customization, reduced complexity of assembly, and manufacturability in a short period of time. In particular, a crystalline resin, namely, polyamide (polyamides 12 and 11), is used as the standard material—with more than 95 % of the market—for SLS [1]. Therefore, it is a problem that usable materials are severely limited, and needs concerning various applications of SLS are not being satisfied [1]. Under those circumstances, resin-powder materials other than PA 12 and PA 11 are being vigorously researched [2-11].

As one of the crystalline resins developed in many industries, poly(butylene terephthalate) (PBT) is well-balanced in terms of mechanical properties, heat resistance, chemical resistance, dimensional stability, and cost [12]. In a previous study [9], the authors used a powder (namely, powdered cPBT pellets formed by low-temperature grinding) with lower crystallization temperature than that of the homo PBT used by Schmidt et al. [8], and we demonstrated the feasibility of SLS with powder-bed temperature set to 190 °C.

Furthermore, it was reported that the mechanical properties (tensile strength, flexural strength, and notched Charpy impact strength) of SLS products are maximized under laser-irradiation conditions that produce the least porosity. PBT resin is often formed around electronic components because of its good electrical characteristics; however, to

apply it to end-use products, flame retardancy is often required as a specification. For that reason, the effects of adding flame retardants to PBT on various properties of IM products have been extensively studied [13, 14]. On the other hand, as for SLS, grades of PA12 and PA11 with added flame retardant have been distributed and studied [15, 16], but examples of studies on other resins are few and far between. Therefore, as in the case of IM products, in the case of SLS products, it is essential to fully understand the influence of adding flame-retardant materials. Accordingly, in the present study, we investigated the effect on powder characteristics and properties of SLS specimens when brominated flame-retardant and antimony trioxide were added to cPBT resin. We then compared those characteristics with those of injection-molded specimens.

3-2. Experimental methods

3-2-1. Sample preparation

Material

For resin pellets, cPBT (containing 10-mol% isophthalic acid) pellets [9] and FR-cPBT pellets were used. The FR-cPBT pellets were prepared by melt extruding cPBT pellets, 10 wt% of halogen-based flame retardant (FR), and 5 wt% of antimony-trioxide (ATO) as a synergist with a twin-screw extruder (KTX-30, Kobe Steel Ltd.) under the following conditions: feed revolution rate: 270-320 rpm; screw revolution rate: 200 rpm ; and resin temperature: 250-255 °C.

In general, flame-retardant polymer containing halogen-based FR additives and antimony-trioxide (ATO) demonstrates a high flame-retardant efficiency because it stops the thermal-decomposition chain reaction (i.e., “radical-trap effect”) and the

diluting-and-blocking effect of oxygen under gas phase by a phased reaction between a halogen compound and ATO [17].

For FR additives, poly(pentabromobenzyl acrylate) (PPBBA) (FR 1025 [14, 18], ICL) was used. PPBBA has a molecular weight of 60,000, a density of 2.50 g/cm^3, a bromine content of 71%, and a melting range of 190 to 220°C. Average particle diameter of the ATO powder used (AT-3CN, Suzuhiro Chemical Co., Ltd.) is 1.0 to 2.0 μm. A cross-sectional SEM image of the FR-cPBT pellets is shown in Fig. 1, which shows that most of the ATO powder is embedded in the PPBBA resin.

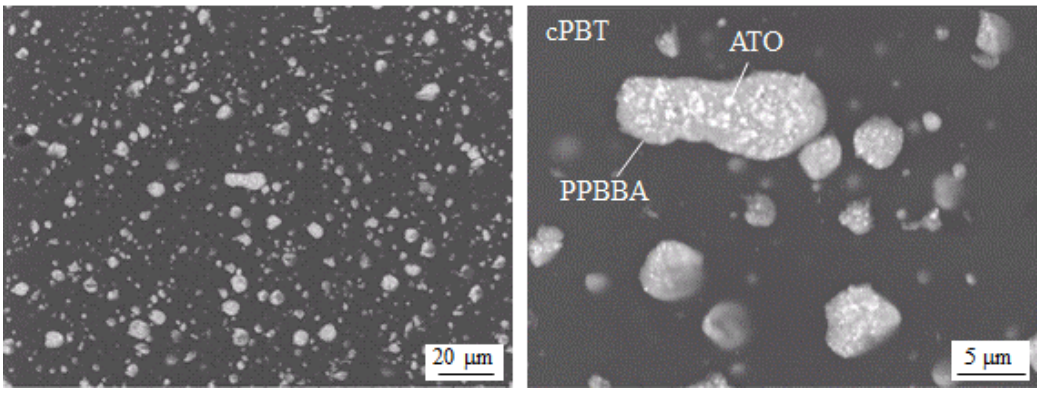

Fig. 1: Cross-sectional SEM image of FR-cPBT pellets.

The FR-cPBT powder was prepared by the following two processes. (Note that the cryomilling used is similar to the method reported in regard to conventional cPBT [9].)

· FR-cPBT powder: Powder made by cryomilling FR-cPBT pellets (resulting powder size of D50 particles: 65.3 μm).

· Dry-blended FR-cPBT: cPBT pellets and PPBBA (D50: 118.0 μm) are respectively powdered by cryomilling. Dry-blended powders were prepared by adding

10 wt% of cryomilled PPBBA powder (D50: 27.4 μm) and 5 wt% of ATO powder to the cPBT powder (D50: 78.8 μm).

In addition, to compare various properties, other powders, namely, powder formed by adding 10 wt% of cryomilled PPBBA to cPBT powder and powder formed by adding 5 wt% of ATO to cPBT powder, were also used. SEM images of the formed FR-cPBT powder, dry-blended FR-cPBT powder, dry-blended cPBT/10-wt%-PPBBA powder, and dry-blended cPBT/5-wt%-ATO powder are shown in Fig. 2.

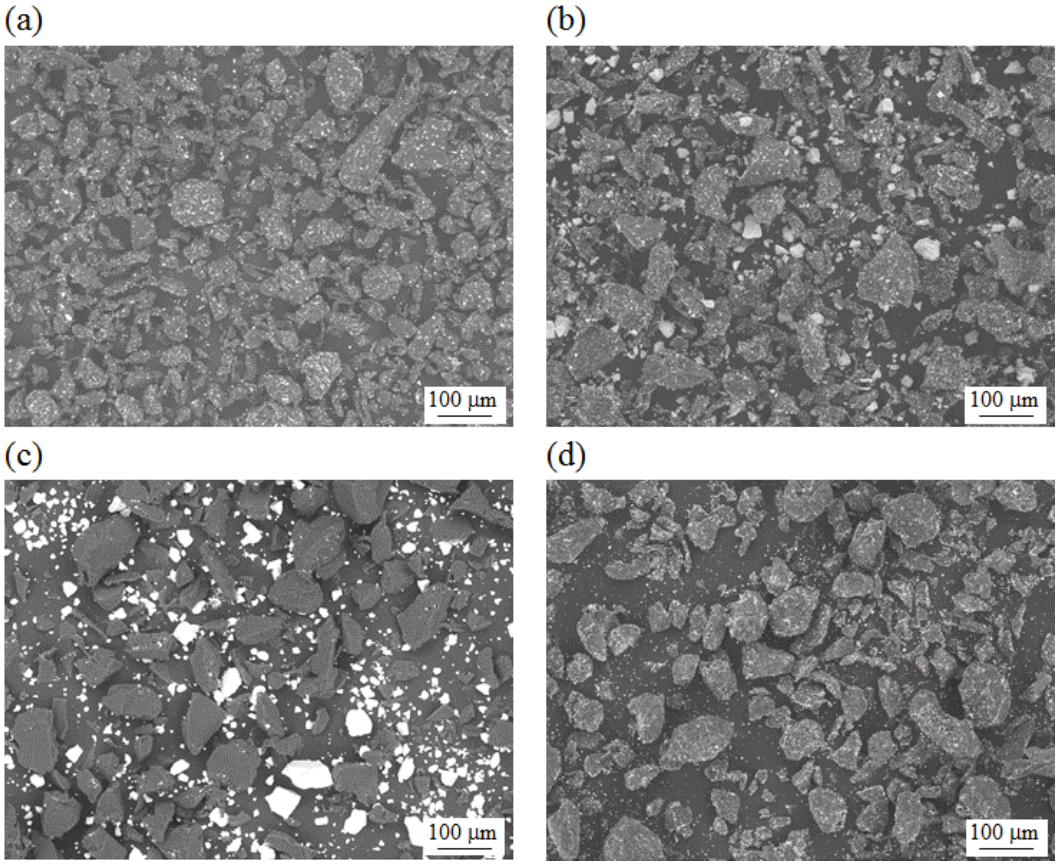

Fig. 2: SEM images of powder: (a) FR-cPBT, (b) dry-blended FR-cPBT, (c) dry-blended cPBT/10-wt% PPBBA, and (d) dry-blended cPBT/5-wt% ATO.

As for the FR-cPBT powder, it is pulverized into a state in which a great deal of the ATO powder is embedded in the PPBBA; in contrast, as for the dry-blended FR-cPBT,

cryomilled-PPBBA and ATO exist around the PBT resin powder. As regards a material for SLS, flowability of the powder is a key property. Accordingly, to improve the flowability, a dry-particle coating using fumed silica is applied to the powder to reduce the attractive force between the SLS-powder particles [19, 20]. Therefore, for each powder, 0.1 wt% of hydrophobic silica (AEROSIL® RA 200 H, Evonik Industries) was added in the same manner as in the case of conventional cPBT powder for SLS [9]. The powders were mixed for 15 minutes with a mixer (SKH-40CA, Misugi Ltd.) and used for SLS.

Selective laser sintering (SLS)

An SLS machine (RaFaEl 300, Aspect Inc.) was used for fabricating the specimens. A carbon-dioxide laser (with wavelength of 10.6 μm and spot diameter of about 0.3 mm) was used as a heat source. The parameters that influence the quality of the SLS specimens are laser power, scan rate, scan spacing, powder-bed temperature, feed temperature, and layer thickness [1]. Of those parameters, laser power was taken as the variable (namely, 8, 11, 14, 17, or 20 W) used in this study. All SLS processing parameters are listed in Table 1. A previous study [9] found that when cPBT was used, if powder-bed temperature was 193 °C, the cPBT powder could not be layered uniformly, whereas at 190 °C, it could be laid and shaped normally. In accordance with that finding, in this study, powder-bed temperature was taken as 190 °C or 192 °C. All parameters other than laser power and powder-bed temperature were the same as those used in our previous study on cPBT [9]. As for SLS, it is reported that the build direction of the fabricated specimens has a significant effect on its properties [1, 21]. Accordingly, in this study, as for build direction, the x-direction is defined as the

roller-movement direction, the y-direction is defined as the perpendicular surface direction (i.e., perpendicular to the direction in which the roller moves along the surface), and the z-direction is defined as the layer-thickness direction.

Table 1: Processing parameters used for SLS.

Processing parameters	
Wavelength	10.6 μm
Laser-beam diameter	0.3 mm
Fill and outline laser power	8 - 20 W
Scan speed	5.0 m/s
Scan spacing	0.15 mm
Fill energy density	10.7 - 26.7 kJ/m^2
Laser-scan direction	Alternating bi-directional scan
Powder-bed temp.	190 °C or 192 °C
Feed temp.	165 °C
Layer thickness	0.1 mm
Part piston temp.	180 °C

Injection molding (IM)

FR-cPBT pellets were dried for 4 hours at 140 °C and then injection molded to form IM specimens (S-2000i 50A, Fanuc Corporation) under the following conditions: nozzle temperature: 245 °C; cylinder temperatures: 250 °C (front zone), 240 °C (middle zone), and 235 °C (rear zone); tool temperature: 80 °C; injection pressure: 25 MPa; injection speed: 20 mm/s; and screw revolution rate: 120 rpm.

3-2-2. Evaluation methods

Powder flowability

As for SLS, flowability of the powder significantly affects the properties of the formed products. Flowability of the sample powders (with or without 0.1-wt% silica) with FR-cPBT, dry-blended FR-cPBT, dry-blended cPBT/10-wt% PPBBA, and

dry-blended cPBT/5-wt% ATO was evaluated in terms of Hausner ratio (HR), given as [22]

$$\mathrm{HR} = \frac{\rho_{tapped}}{\rho_{bulk}} \tag{1}$$

where ρ_{tapped} (tapped density) and ρ_{bulk} (bulk density) were measured at 25 °C by powder-characteristics tester (PT-X, Hosokawa Micron Corporation).

Differential-scanning calorimetry (DSC)

DSC (Q2000, TA Instruments) was used to determine the melting point and crystallization of the cPBT pellets, FR-cPBT pellets, cPBT powder, FR-cPBT powder, dry-blended FR-cPBT powder, dry-blended cPBT/10-wt%-PPBBA powder, and dry-blended cPBT/5-wt%-ATO powder. The IM and SLS specimens were cut from the central portion of the flexural-test specimens (with weight of 5 mg) and evaluated by DSC (to investigate their degree of crystallinity) under the following conditions: heating from 25 °C to 300 °C followed by cooling to 25 °C, heating rate and cooling rate of 10 °C/min, and nitrogen flow rate of 40 ml/min.

Degree of crystallinity (χ) [23] is expressed in terms of heat of fusion of the sample (ΔH), heat of complete crystal fusion (ΔH_m^o), and mass fraction of material other than the main polymer as

$$\chi(\%) = \frac{\Delta H}{\Delta H_m^o \times (1 - f)} \times 100 \tag{2}$$

In this study, ΔH_m^o of PBT was taken as 145.5 J/g [24, 25]. Crystallization times of the cPBT pellets, FR-cPBT pellets, cPBT powder, FR-cPBT powder, dry-blended

FR-cPBT powder, dry-blended cPBT/10-wt%-PPBBA powder, and dry-blended cPBT/5-wt%-ATO powder were determined by isothermal-crystallization DSC (EXSTAR 6000, Seiko Instruments Inc.). In detail, the powders were heated to 250 °C, held for 10 min at that temperature, and then cooled to 190 °C or 192 °C, at which the heat of crystallization was measured. Crystallization half-time (t1/2) was calculated as the time taken for the heat of crystallization to reach 50 % of the value for complete crystallization.

Mechanical testing

The mechanical properties of the IM specimens with FR-cPBT and the SLS specimens with FR-cPBT, dry-blended FR-cPBT, dry-blended cPBT/10-wt% PPBBA, and dry-blended cPBT/5-wt% ATO were evaluated by tensile tests, flexural tests, and Charpy impact-strength tests. The tensile-testing specimens were taken as "type A" specified in ISO3167; 1993 [total length: 170 mm (x-direction); parallel-portion length (x-direction): 80 mm; thickness: 4 mm (z-direction)]. The tensile tests were performed on a 5500RF, Instron Corporation, according to ISO527-1 and -2; 2012; testing speed was 50 mm/min, and distance between the clamps was 115 mm. The flexural tests were performed on the same machine according to ISO178; 2001 with test-specimen size of 80 (x-direction)×10 (y-direction)×4 mm (z-direction); testing speed was 2 mm/min, and the distance between the fulcrums was 64 mm. The Charpy-impact-strength tests were performed on an AG-100kNX, Shimadzu Corporation, according to ISO179–1; 2010. A notch was formed in a test specimen with the same shape as that in the flexural test specimens. With an energy of 0.5 J, the hammer weight was applied so that the impact was in the edgewise direction.

Heat-deflection-temperature (HDT) testing

Heat-deflection temperatures (HDT) of the IM specimens with FR-cPBT and the SLS specimens with FR-cPBT, dry-blended FR-cPBT, dry-blended cPBT/10-wt%-PPBBA, dry-blended cPBT/5-wt%-ATO were measured by HDT tester (6A-2, Taiyo-Seiki Co., Ltd.) according to standard ISO75-1,-2; 2004 (JIS K7191-1,-2; 2007) in flatwise mode under bending stress of 1.82 MPa.

Observations by optical microscopy and scanning electron microscopy (SEM)

The morphology of the IM and SLS specimens was investigated by polarization microscopy (LV100POL, Nikon Corporation). The central portions of the specimens (10 mm (y-direction)×4 mm (z-direction)) were cut in the direction of lamination thickness, and pieces with thickness of 3 to 4 μm were prepared by microtome. The thin pieces were observed by polarization microscopy.

To evaluate the porosity ratio of the test specimens, the central portions of the SLS and IM specimens were cut in the same direction as the previously mentioned specimens, and after embedding the specimens in epoxy resin, near-center portions of the SLS and IM specimens were polished at intervals of 0.5 mm in the y-direction and observed by microscope (VHX-2000, Keyence Corporation). After that, the porosity ratios of five cross-sections of each specimen were calculated by image processing (WinROOF, Mitani Corporation). Cross-sectional samples similar to the porosity-measured samples were used for SEM observation (TM-1000, Hitachi High-Technologies Corporation) of the conditions of the PPBBA and ATO contained in the IM specimens made with FR-cPBT pellets and the SLS specimens formed with FR-cPBT powder and dry-blended FR-cPBT powder. The SEM images were obtained under acceleration voltage of 15 kV.

Microscale combustion calorimetry (MCC)

Thermal-combustion properties of the cPBT and FR-cPBT pellets and the cPBT, FR-cPBT, and dry-blended FR-cPBT powders (with or without 0.1-wt% silica) were measured by MCC test (MCC-3-X-UL, Govmark, Inc.) according to ASTM D7309-07 method A (pyrolysis under nitrogen). The IM specimens with FR-cPBT and the SLS specimens with FR-cPBT and dry-blended FR-cPBT were cut from the central portion of the flexural test pieces, and 10 mg of each specimen was heated at 1 °C/s from 75 °C to 850 °C.

Underwriters Laboratories (UL) test standard 94

The IM specimens with FR-cPBT and the SLS specimens with FR-cPBT and dry-blended FR-cPBT were subjected to vertical-burning tests according to UL-94. The dimensions of the specimens were 125 mm (x-direction)×13 mm (y-direction)×2.0 mm (z-direction) as specified in IEC60695-11-10 B.

3-3. Results and discussion

3-3-1. Powder characteristics

Powder flowability

The evaluation results for HR of the FR-cPBT powder, dry-blended FR-cPBT powder, dry-blended cPBT/10-wt%-PPBBA powder, and dry-blended cPBT/5-wt%-ATO powder with or without addition of 0.1-wt% silica are plotted in Fig. 3.

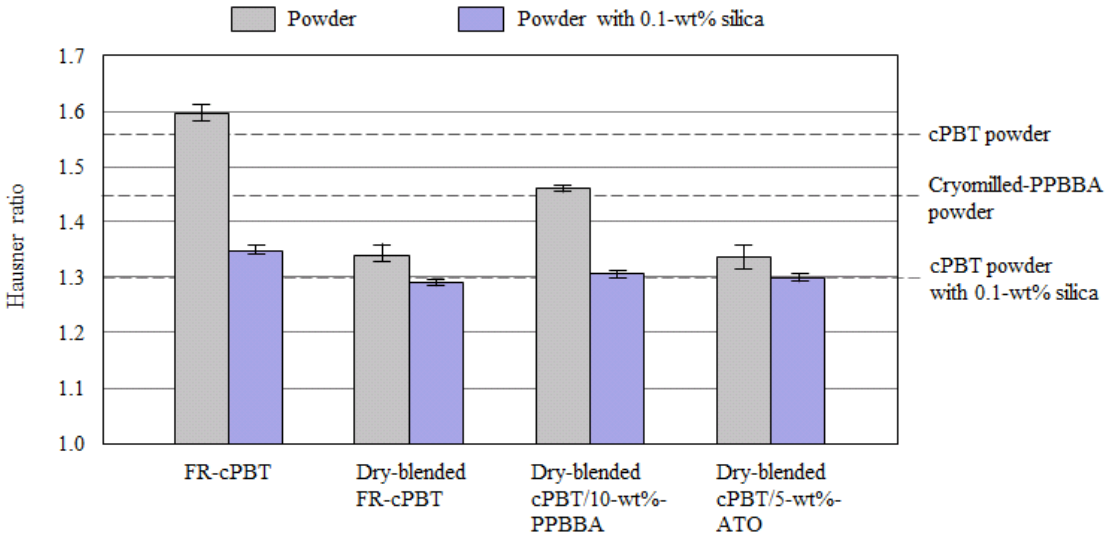

Fig. 3: Comparison of HR of FR-cPBT powder, dry-blended FR-cPBT powder, dry-blended cPBT/10-wt%-PPBBA powder, and dry-blended cPBT/5-wt%-ATO powder with or without 0.1-wt% added silica.

For comparison, the HR values of cPBT powder [9] and cryo-milled PPBBA powder with or without addition of 0.1-wt% silica are also shown. It is clear from the figure that compared to the flowability of the cPBT powder, that of the FR-cPBT powder is deteriorated; in contrast, the flowabilities of dry-blended FR-cPBT powder, dry-blended cPBT/10-wt%-PPBBA powder, and dry-blended cPBT/5-wt%-ATO powder are improved. It was reported by Ziegelmeier et al. [26] that as average size of the powder decreases, HR also decreases. In this study, the D50 value of the FR-cPBT powder (65.3 μm) was less than that of the cPBT powder (78.8 μm); therefore, it is presumed that the flowability of the cPBT powder was deteriorated. On the other hand, the dry-blended FR-cPBT powder and dry-blended cPBT/5-wt%-ATO powder have greatly improved flowability (lower HR). This result is explained by the fact that the ATO powder is coated around the cPBT resin and acts as a lubricant, as shown in Figs. 2(b) and (d). It is also clear from Fig. 3 that the cryo-milled PPBBA powder itself has higher

flowability than that of the cPBT powder, and that part of the fine powder works as a cPBT lubricant; as a result, dry-blended cPBT/10-wt%-PPBBA powder is considered to have better flowability than cPBT powder. Moreover, it is confirmed that that addition of 0.1 wt% of silica to any of the powders improves their flowability. The flowability-improvement effect of adding silica is particularly strong in the case of the FR-cPBT powder (with high HR value) and the dry-blended cPBT/10-wt%-PPBBA powder.

Crystallization characteristics

The DSC results for the cPBT and FR-cPBT pellets and the cPBT, FR-cPBT, dry-blended FR-cPBT, dry-blended cPBT/10-wt%-PPBBA, and dry-blended cPBT/5-wt%-ATO powders (to which 0.1 wt% of silica was added) are listed in Table 2.

Table 2: Results of evaluation of melting point, crystallization temperature, and crystallization half-time at 190 °C and 192 °C of pellets (cPBT and FR-cPBT) and powders (cPBT, FR-cPBT, dry-blended FR-cPBT, dry-blended cPBT/10-wt% PPBBA, and dry-blended cPBT/5-wt% ATO).

	Form	Fumed silica	Tm (°C)	Tc (°C)	Crystallization half-time (s)	
					192 °C	190 °C
cPBT	Pellet	None	207.5	150.7	-	4196
FR-cPBT	Pellet	None	207.6	171.6	1207	739
cPBT	Powder	0.1-wt%	207.5	169.7	1560	855
FR-cPBT	Powder	0.1-wt%	207.4	174.4	847	485
Dry-blended FR-cPBT	Powder	0.1-wt%	207.1	175.9	586	375
Dry-blended cPBT/10-wt%-PPBBA	Powder	0.1-wt%	207.2	169.3	1583	952
Dry blended cPBT/5-wt%-ATO	Powder	0.1-wt%	207.1	177.5	326	231

It is known that in the case of SLS, the relationship between melting point and crystallization temperature of the powder and powder-bed temperature of the SLS apparatus is very important [1]. Up until now, in modeling PBT powder, if powder-bed temperature was set at 193 °C, the powder aggregated and could not be laid uniformly with the rollers; however, by setting the temperature to 190 °C, uniform laying and modeling become possible [9]. Accordingly, the isothermal crystallization DSC was performed at 190 °C and 192 °C.

According to the table, the melting points of all of the pellets and powders show no significant difference, whereas their crystallization temperatures and crystallization times show significant differences. Moreover, comparing the crystallization temperatures of the pellets reveals that the crystallization temperature of FR-cPBT is higher than that of cPBT; as a result, the crystallization time at 190 °C is greatly reduced. In the case of the FR-cPBT powder, its crystallization temperature is increased and its crystallization time is shortened in comparison with those of the FR-cPBT pellets. From a previous study [9], it was clarified that while contaminants during pulverization of cPBT pellets act as crystal-nucleating agents, silica does not. As for the FR-cPBT powder used in this study, it is presumed that a similar tendency—namely, contamination acted as a nucleating agent—was observed because a similar powdering method was used. However, it is considered that at the stage when the FR-cPBT is in the form of pellets (before pulverization), crystallization is promoted to a greater extent than in the case of the cPBT pellets; as a result, the increase in crystallization temperature when the FR-cPBT is powdered from pellet form was lower than in the case of cPBT.

Furthermore, comparing the powders revealed no significant difference in the crystallization characteristics of the cPBT powder and the dry-blended cPBT/10-wt%-PPBBA powder. On the other hand, it was revealed that in the case of all the powders dry-blended with ATO, crystallization temperature is greatly increased, and crystallization time becomes considerably shorter than that of the cPBT powder. In the case of PA12, it has been reported that dry-blended clays [27], carbon nanotubes [28], and graphite nanoplatelets [29] act as crystal-nucleating agents. The results of this study revealed that in the case of cPBT, the PPBBA powder does not act as a crystal-nucleating agent, whereas the ATO powder does.

Combustion characteristics

The results of evaluation by MCC of the cPBT and FR-cPBT pellets and the cPBT, FR-cPBT, and dry-blended FR-cPBT powders (with or without 0.1-wt% silica) are plotted in Fig. 4 and listed in Table 3.

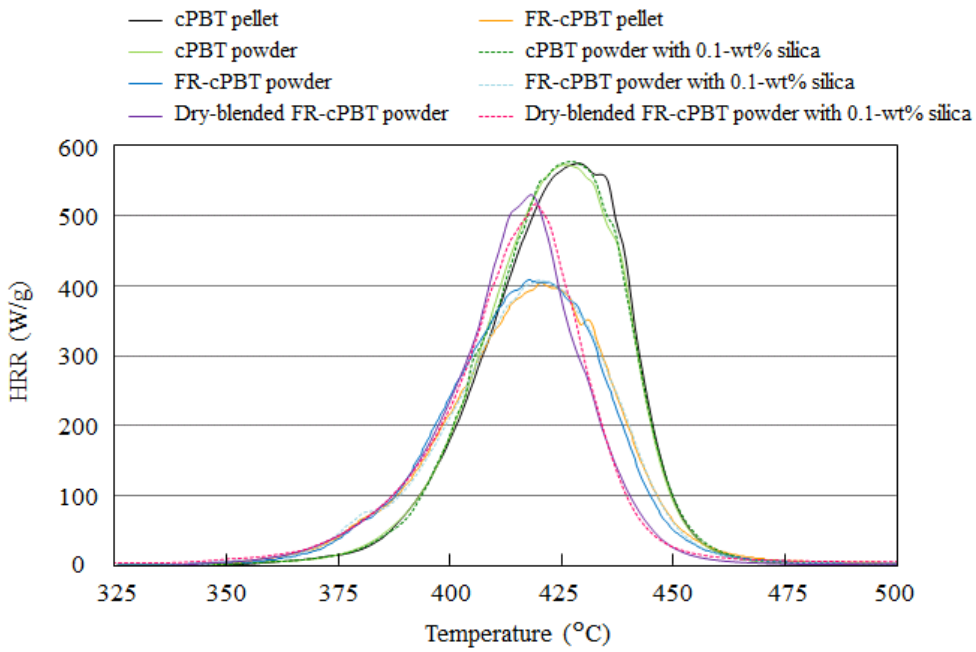

Fig. 4: HRR curves obtained by MCC of cPBT and FR-cPBT pellets, cPBT powder, FR-cPBT powder, and dry-blended FR-cPBT powder with or without 0.1-wt% silica.

Table 3: HRC and THR values obtained by MCC of cPBT and FR-cPBT pellets and cPBT, FR-cPBT, and dry-blended FR-cPBT powders with or without 0.1-wt% silica.

	Form	Fumed silica	HRC (J/g·K)	THR (kJ/g)
cPBT	Pellet	None	579	22.5
FR-cPBT	Pellet	None	407	18.5
cPBT	Powder	None	575	22.6
		0.1-wt%	580	22.6
FR-cPBT	Powder	None	414	18.6
		0.1-wt%	413	18.7
Dry-blended FR-cPBT	Powder	None	551	18.4
		0.1-wt%	547	18.1

Comparing the cPBT pellets and powder reveals no significant differences between the heat-release-rate (HRR) curves (Fig. 4) and between the heat-release-capacity (HRC) values and between the total-heat-release (THR) values (Table 3). Likewise, comparing the FR-cPBT pellets and powder reveals no significant differences between the HRR curves and between the HRC values and between the THR values. It is therefore concluded that pulverization by low-temperature pulverization and addition of 0.1-wt% silica does not affect the combustion characteristics. Moreover, comparing the cPBT and FR-cPBT powders reveals that since PPBBA (which is a flame retardant) causes thermal decomposition at a lower temperature than that in the case of cPBT, due to the actions of PPBBA and ATO, HRR on the low-temperature side increases compared to that of cPBT, and HRC and THR are decreased significantly. That is, the flame-retardant properties of the powder are greatly improved. In regard to the HRR curves, comparing the FR-cPBT powder and the dry-blended FR-cPBT powder reveals

that, in the case of the dry-blended FR-cPBT powder, combustion occurs more rapidly on the lower-temperature side and ends more abruptly when the temperature becomes high. As a result, the HRC values in the two cases significantly differ. In the case of the FR-cPBT pellets and powder used in this study, the ATO powder is mostly embedded in the PPBBA, whereas the dry-blended FR-cPBT powder is only attached around the PPBBA. As a result, the combustion characteristics are thought to differ depending on the physical distances between the cPBT, PPBBA, and ATO regions. However, the proportions of PPBBA and ATO in the powder are equal, so the THR values (representing total area of HRR) are fairly equivalent.

3-3-2. Characteristics of laser sintered and injection molded specimens

Mechanical properties

SLS was performed under two powder-bed temperatures for the following reasons. According to the DSC results, Tc of the FR-cPBT, dry-blended FR-cPBT, and dry-blended cPBT/5-wt%-ATO powders was increased compared to that of the cPBT powder, so one powder-bed-temperature setting was taken as 192 °C. Moreover, the dry-blended cPBT/10-wt%-PPBBA powder has roughly equivalent Tc to that of the cPBT powder, so the other powder-bed-temperature setting was taken as 190 °C. Tensile strength, elongation at break, flexural strength, and Charpy impact strength of the FR-cPBT, dry-blended FR-cPBT, dry-blended cPBT-10/wt%-PPBBA, and dry-blended cPBT/5-wt%-ATO SLS specimens fabricated at laser-energy densities of 10.7, 14.7, 18.7, 22.7, and 26.7 kJ/m^2 are shown in Fig. 5.

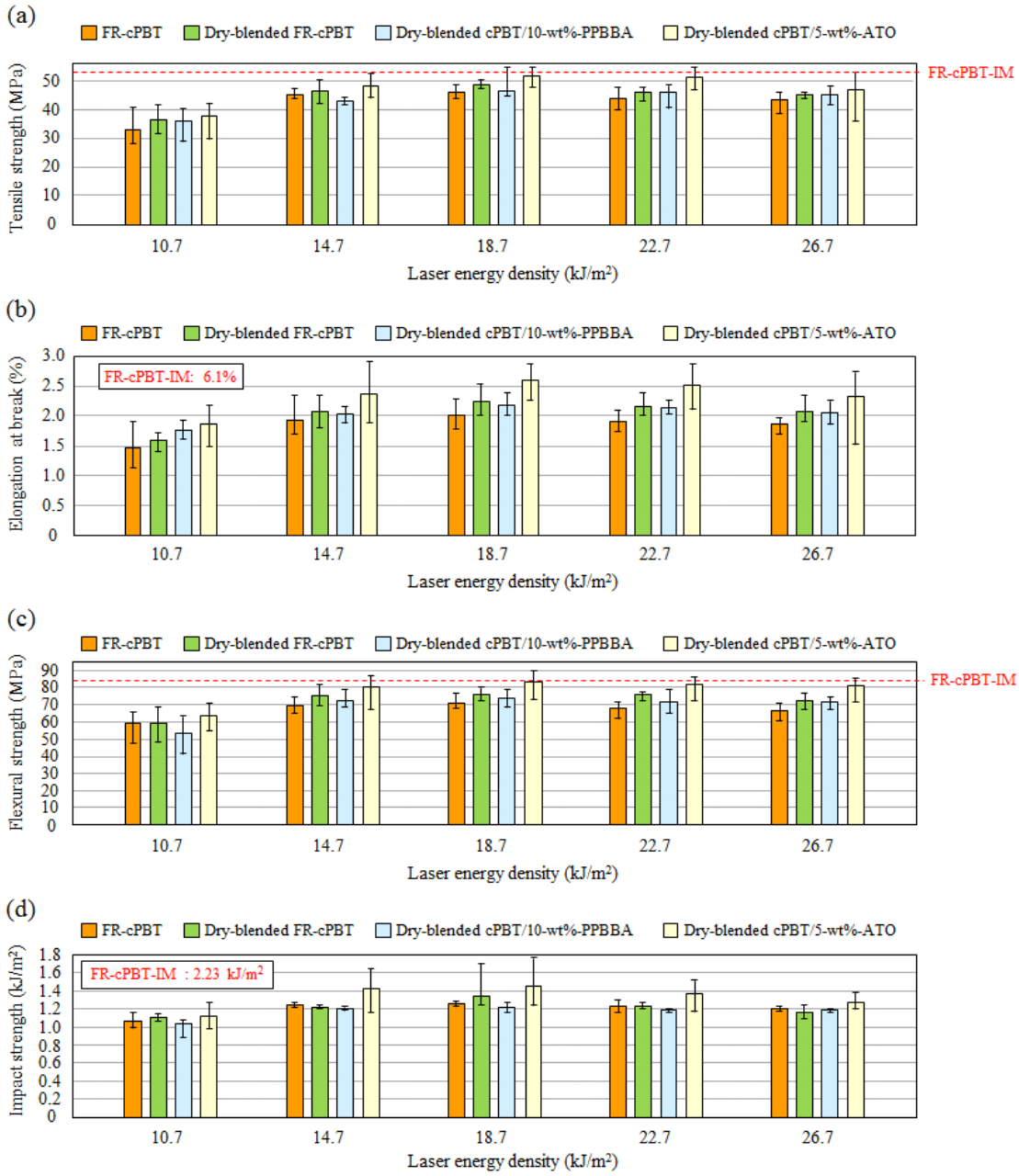

Fig. 5: Comparison of tensile properties of FR-IM specimens and SLS specimens composed of FR-cPBT, dry-blended FR-cPBT, dry-blended cPBT/10-wt% PPBBA, and dry-blended cPBT/5-wt% ATO under assumed laser-energy densities of 10.7, 14.7, 18.7, 22.7, and 26.7 kJ/m²: (a) tensile strength, (b) elongation at break, (c) flexural strength, and (d) notched Charpy impact strength.

For comparison, the results for the injection-molded FR-cPBT specimens are also shown. According to these results, in the case of the SLS specimens, the values of all the properties are lower than those of the IM specimens. In particular, the mechanical properties of the SLS specimens in comparison with the IM specimens are significantly lower in terms of elongation at break and impact strength, and that finding is similar to the results of another investigation on cPBT [9] and other reports [29, 30] on PA12. In the case of the mechanical properties of all the powders used for SLS, when laser-energy density was 18.7 kJ/m^2, all the mechanical properties show maximum values. The phenomenon that mechanical properties are degraded as laser energy density increases from a certain value is similar to that reported in the case of cPBT [9] and that reported by Caulfield, et al. [21] and Vasquez, et al. [31] on PA12. The cause of this phenomenon is presumed to be thermal decomposition (i.e., reduction in molecular weight) of the resin due to input of excessive energy. In the following evaluations, mechanical-property values corresponding to laser energy density of 18.7 kJ/m^2 (which maximizes mechanical properties) are compared.

Comparing the SLS specimens composed of cPBT [9] with the SLS specimens composed of dry-blended cPBT/10-wt% PPBBA reveals that all mechanical properties decreased by 7 to 36 %. On the other hand, the SLS specimens composed of dry-blended cPBT/5-wt% ATO show a 5 % increase in flexural strength but 5 to 23 % decreases in the other properties (tensile strength, elongation at break, and impact strength). It is clear from these results that when PPBBA is added, all the mechanical properties tend to be decreased. It is also clear that in comparison with the mechanical properties of the FR-cPBT SLS specimens, all those of the dry-blended FR-cPBT and dry-blended cPBT/5-wt%-ATO SLS specimens are enhanced. As shown above, the

dry-blended FR-cPBT powder and the dry-blended cPBT/5-wt%-ATO powder are samples prepared by coating ATO powder around cPBT resin powder. It can therefore be inferred that the states of PPBBA and ATO affect the mechanical properties of the SLS specimens. However, it is also known that porosity significantly affects mechanical properties [1, 32, 33]. Given that fact, porosity and morphology are focused on in the following subsections.

Thermal properties

The results of tests to determine heat-deflection temperature (HDT) of the FR-IM and SLS specimens (FR-cPBT, dry-blended FR-cPBT, dry-blended cPBT/10-wt% PPBBA, and dry-blended cPBT/5-wt% ATO) are shown in Fig. 6.

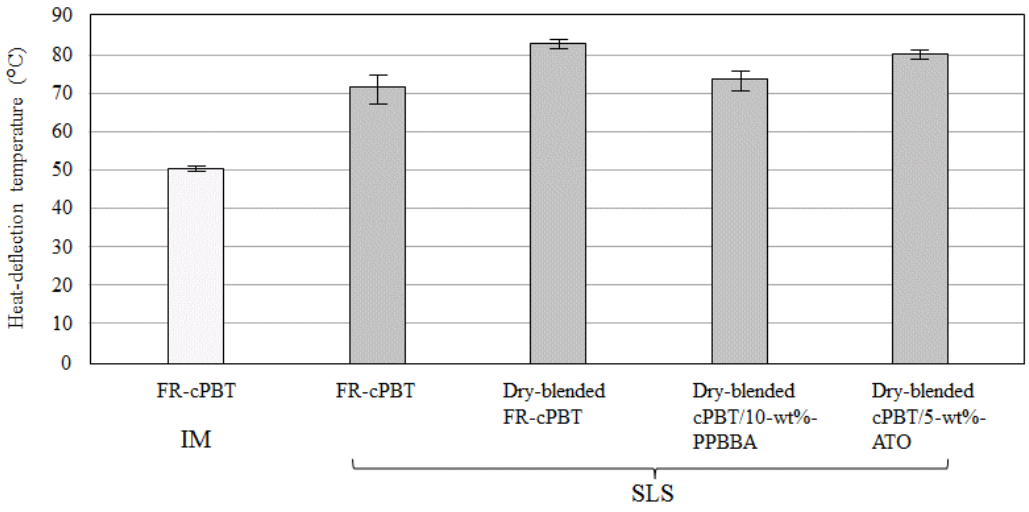

Fig. 6: Comparison of heat-deflection temperatures (HDT) of FR-IM specimens and SLS specimens composed of FR-cPBT, dry-blended FR-cPBT, dry-blended cPBT/10-wt% PPBBA, and dry-blended cPBT/5-wt% ATO.

It is clear from the figure that compared to the IM specimens, the SLS specimens tend to have higher HDT. Moreover, as mentioned in previous subsection, addition of PPBBA degrades each mechanical property; however, HDT was found to be slightly

increased compared to that of the IM specimens. Furthermore, in the same manner as mechanical properties, the dry-blended FR-cPBT and dry-blended cPBT/5-wt%-ATO SLS specimens showed higher HDTs than those of the FR-cPBT SLS specimens. It is known that HDT greatly affects degree of crystallinity in the case of IM specimens [34, 35], and that effect is discussed in the following subsection.

Porosity evaluation

According to Ziegelmeier et al. [26], the flowability of powder significantly influences the strength and porosity of the fabricated specimen. According to the evaluation result presented in the subsection of powder flowability, HR of the FR-cPBT powder was higher than that of the cPBT powder or dry-blended FR-cPBT powder. Cross-sectional observation images of the FR-cPBT and dry-blended FR-cPBT SLS specimens and the FR-cPBT IM specimen are shown in Fig. 7.

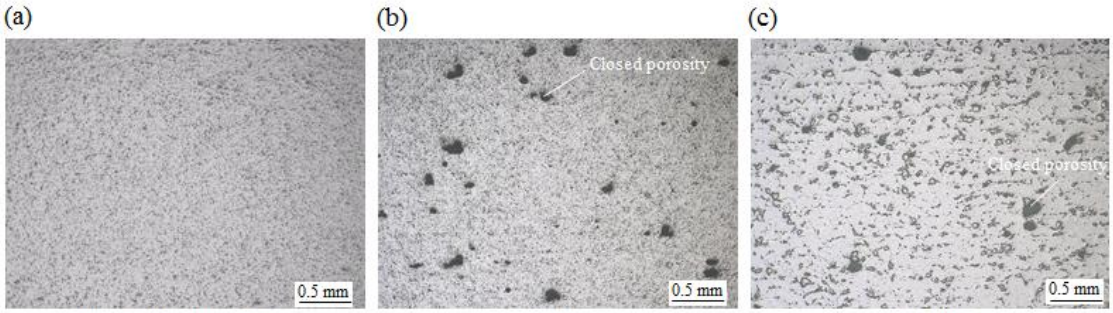

Fig. 7: Cross-sectional-observation images by optical microscope of (a) IM specimens composed of FR-cPBT and SLS specimens composed of (b) FR-cPBT and (c) dry-blended FR-cPBT.

As for the IM specimen, porosity cannot be observed, whereas as for the SLS specimens, a certain amount of porosity can be observed. This result agrees with the results of another investigation on cPBT [10] and a study by Zarringhalam et al. [36].

Therefore, as for the FR-IM and SLS specimens, porosity is presumed to be the main cause of the deterioration of mechanical properties of the SLS specimens. Moreover, when the FR-cPBT and dry-blended FR-cPBT SLS specimens are compared, it becomes clear that only closed porosity exists, and the porosity ratios in both cases differ only slightly. In particular, those porosity ratios do not significantly differ from that previously reported in a study on cPBT (1.74 %) [9]. It is therefore considered that the difference in HR values determined in the present study does not significantly influence mechanical properties of the various used powders; instead, the differences in the mechanical properties are considered to be mainly caused by factors other than porosity.

Crystallization characteristics and morphology

The results of the evaluation of degree of crystallinity of the FR-IM and SLS specimens (FR-cPBT, dry-blended FR-cPBT, dry-blended cPBT/10-wt% PPBBA, and dry-blended cPBT/5-wt% ATO) are shown in Fig. 8.

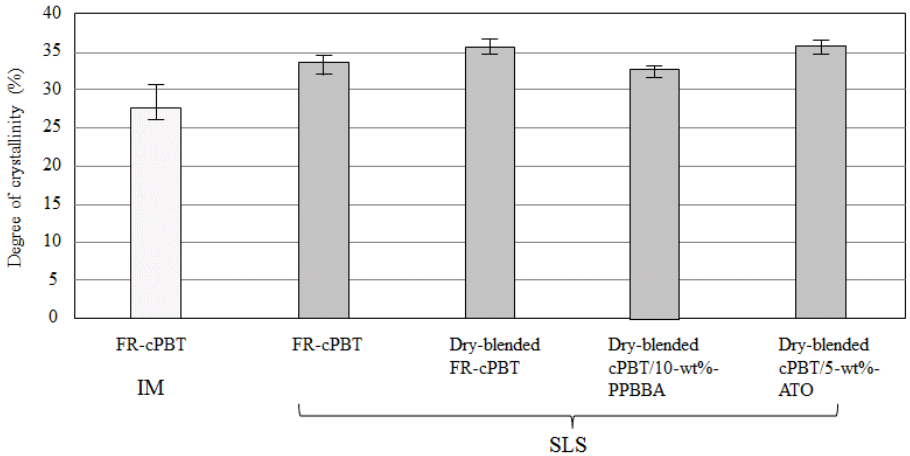

Fig. 8: Results of evaluation of degree of crystallinity of FR-IM specimens and SLS specimens composed of FR-cPBT, dry-blended FR-cPBT, dry-blended cPBT/10-wt% PPBBA, and dry-blended cPBT/5-wt% ATO.

According to the figure, it is evident that the crystallinity of all the SLS specimens is higher than that of the IM specimens. This result agrees with a previously reported result concerning cPBT [9] and results reported by Karevan, et al. [29] and Hooreweder, et al. [37]. Therefore, as explained in the subsection of thermal properties, the main reason that the SLS specimens showed higher HDT than that of the IM specimens is considered to be due to the SLS specimens having higher crystallinity than that of the IM specimens. In the measurements performed in this study, the part of the test pieces without a core layer formed from the IM and SLS-formed specimens was measured. However, it is known that the IM specimens have a lower degree of crystallinity in the skin layer with respect to the core layer [38]. Therefore, as for the whole IM specimen (with thickness of 4 mm) measured in the tests on mechanical property and HDT, the degree of crystallinity is lower than the value shown in Fig. 8, and from the viewpoint of degree of crystallinity, it is considered that the difference between the SLS and IM specimens is more significant. Accordingly, it can be concluded that from the viewpoint of HDT, the influence of degree of crystallinity is greater than that of porosity. When the SLS specimens are compared, it becomes clear that degrees of crystallinity of the dry-blended FR-cPBT and dry-blended cPBT/5-wt%-ATO specimens (which showed high values of mechanical properties and HDT) are slightly higher than those of the FR-cPBT and dry-blended cPBT/10-wt%-PPBBA specimens. It is thought that this difference might be due to the fact that (i) PPBBA is not act as a nucleating agent and (ii) the difference in the total amount of ATO that acts as a nucleating agent in cPBT depends on whether the majority of the ATO is embedded in PPBBA or not.

SEM observations of cross sections of the FR-IM specimen and the SLS specimens (FR-cPBT and dry-blended FR-cPBT) are shown in Fig. 9.

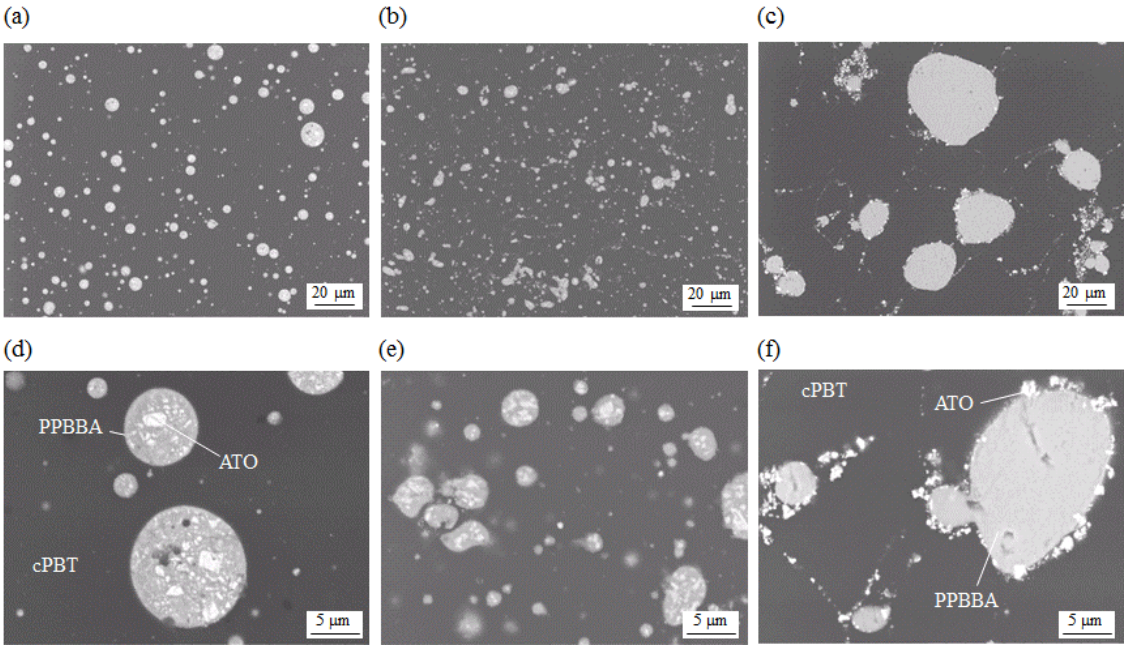

Fig. 9: Cross-sectional SEM images of FR-IM specimens [(a) low and (d) high magnification] and SLS specimens composed of FR-cPBT [(b) low and (e) high magnification] and dry-blended FR-cPBT [(c) low and (f) high magnification].

Similarly to the FR-cPBT pellets, the FR-IM specimen and the FR-cPBT SLS specimen contain a great deal of ATO embedded in the PPBBA; in contrast, the dry-blended FR-cPBT SLS specimen is molded in a state in which the ATO is coated around the PPBBA and PBT powders. In other words, it is conceivable that in contrast to the FR-cPBT SLS specimen, the main cause of the increase in mechanical properties and thermal characteristics of the dry-blended FR-cPBT and dry-blended cPBT/5-wt%-ATO SLS specimens is that the proportion of ATO contained in the cPBT is large, and compared to PPBBA, ATO acts as a reinforcing material. Moreover, the state of the ATO coating is expressed in the cross section of the shaped specimen, and that state reveals that in the SLS process, the laser scanning does not cause significant flow of the melted powder.

Polarization-microscopy images of the FR-IM specimens and the SLS specimens composed of FR-cPBT, dry-blended FR-cPBT, dry-blended cPBT/10-wt% PPBBA, and dry-blended cPBT/5-wt% ATO are shown in Fig. 10.

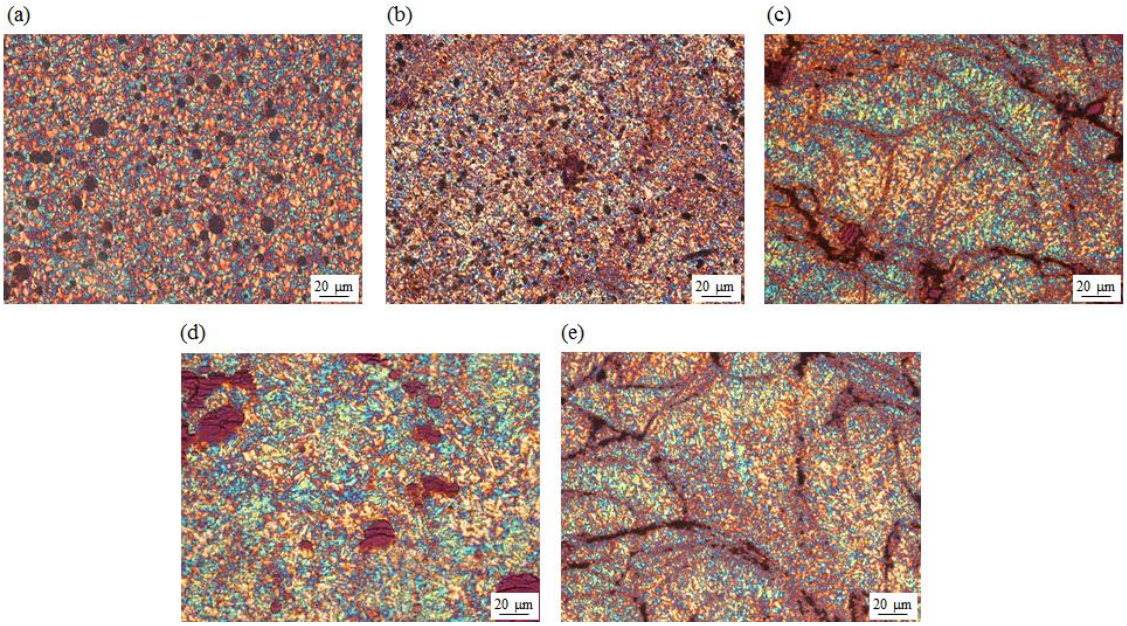

Fig. 10: Polarization-microscopy images of (a) FR-IM specimens and SLS specimens composed of (b) FR-cPBT, (c) dry-blended FR-cPBT, (d) dry-blended cPBT/10-wt% PPBBA, and (e) dry-blended cPBT/5-wt% ATO.

In the case of the FR-IM specimens, Maltese cross-like shapes can be observed; however, no such shapes can be observed in the images of the SLS specimens. In addition, compared to the FR-IM specimen, the FR-cPBT SLS specimen is composed of smaller spherulites. It was shown by the results of DSC evaluation (presented in the subsection of crystallization characteristics) that the PPBBA powder does not act as a nucleating agent, but the ATO powder does. These observations of spherulites confirm that in the case of the dry-blended cPBT/10-wt%-PPBBA specimens, relatively large spherulites are seen. In contrast, in the cases of the dry-blended FR-cPBT and the dry-blended cPBT/5-wt%-ATO specimens, in the vicinity where the ATO powder exists,

the spherulites are small. However, in the region presumed to be the center of some of the cPBT powder particles, the state of the spherulites is almost the same as that of those in the dry-blended cPBT/10-wt%-PPBBA specimens.

Flame-retardant properties and combustion characteristics

The results of the MCC tests and UL94 tests on the FR-IM and SLS (FR-cPBT and dry-blended FR-cPBT) specimens are listed in Table 4.

Table 4: MCC and UL 94 tests results for FR-IM specimens and SLS specimens composed of FR-cPBT and dry-blended FR-cPBT.

	Molding method	Fumed silica	HRC (J/g·K)	THR (kJ/g)	Average burn-flaming-combustion duration (s)		Cotton ignited by flaming drip	UL94 rating
					1st	2nd		
FR-cPBT	IM	None	406	18.3	0	0	No	V0
FR-cPBT	SLS	0.1-wt%	408	18.6	0	0	No	V0
Dry-blended FR-cPBT	SLS	0.1-wt%	546	18.2	0	0	No	V0

The HRC and THR values of the FR-IM, FR-cPBT SLS, and dry-blended FR-cPBT SLS specimens show little difference in comparison with those values of the materials used (FR-cPBT pellets, FR-cPBT powder with 0.1-wt% silica, and dry-blended FR-cPBT powder with 0.1-wt% silica) for fabricating the specimens. This result confirms that the IM and SLS processes do not cause a change in combustion characteristics (radical-trap effect and diluting and blocking oxygen effect under gas phase [17]). Moreover, it was found that UL94 rating of V0 was achieved with a test piece with thickness of 2 mm. According to Lyon, et al. [39], in the MCC test, a polymer that can obtain “V rating” has HRC in the range from 200 to 700 J/g·K; in

particular, when the rating is V0, HRC is reported to be less than 600 J/g·K. All the IM and SLS specimens tested in this study show HRC values within that range. As shown in Fig. 9, however, most of the ATO powder in the FR-cPBT SLS specimens is embedded in the PPBBA, while the SLS specimens composed of dry-blended FR-cPBT have ATO adhering around the PPBBA and cPBT only. As a result, even in the case of the shaped specimens, the distances between cPBT, PPBBA, and ATO regions differ in the same manner as in the case of the powders; therefore, it is conceivable that the difference in distances causes the differences in HRC.

3-4. Conclusions

It was found that the flowability of a flame-retardant dry-blended powder, obtained by dry blending 10 wt% of pulverized PPBBA and 5 wt% of ATO and added to pulverized cPBT, is significantly improved compared to that of powder formed by pulverizing of FR-cPBT pellets (containing kneaded cPBT pellets with 10 wt% of PPBBA and 5 wt% of ATO) because the ATO powder becomes coated around the cPBT powder and the PPBBA powder. Furthermore, in the case of all the flame-retardant powders, their flowability is improved by adding 0.1 wt% of silica, and the improvement effect was especially strong in the case of FR-cPBT powder (which has low flowability). It was also found that the PPBBA powder does not act as a nucleating agent for cPBT, but the ATO powder does; consequently, the crystallization temperature of cPBT is increased. It was also revealed that the combustion characteristics of the powders, especially HRC, differ according to whether or not the ATO is embedded in the PPBBA.

When the flame-retardant IM and SLS specimens were compared, it became clear that the SLS specimens contain more porosity than the IM specimens, so all of their mechanical properties tended to be lower. On the other hand, the SLS specimens showed higher heat-deflection temperature because of their higher crystallinity than the IM specimens. Comparing the different kinds of SLS specimens revealed that the SLS specimens dry blended with ATO showed higher mechanical and thermal properties than the SLS specimens embedded with ATO in PPBBA and the SLS specimens dry blended with PPBBA. It is therefore concluded that the presence or absence of a coating of ATO around the cPBT powder particles affects mechanical properties and thermal characteristics of the SLS specimens. It was also revealed that in the case of the SLS specimens, in the vicinity the ATO coating, the ATO acts as a nucleating agent, so fine spherulites are formed there. In addition, the IM and SLS specimens showed combustion characteristics (HRC and THR) equivalent to those of the pellets and powders before molding. It is therefore concluded that the IM and SLS processes do not affect combustion characteristics of the formed specimens. Furthermore, even in the case of the IM and SLS specimens, HRC varies according to whether or not the ATO embeds in the PPBBA. It was also revealed that all the IM and SLS specimens containing PPBBA and ATO powder formed with thickness of 2 mm satisfy grade V0 of the UL94 test.

References

[1] R.D. Goodridge, C.J. Tuck, R.J.M. Hague, Laser sintering of polyamides and other polymers, Prog. Mater. Sci. 57 (2012) 229–267.

[2] J. Bai, B. Zhang, J. Song, G. Bi, P. Wang, J. Wei, The effect of processing conditions on the mechanical properties of polyethylene produced by selective laser sintering, Polym. Test. 52 (2016) 89–93.

[3] Y. Khalil, A. Kowalski, N. Hopkinson, Influence of energy density on flexural properties of laser-sintered UHMWPE, Addit. Manuf. 10 (2016) 67–75.

[4] W. Zhu, C. Yan, Y. Shi, S. Wen, J. Liu, Y. Shi, Investigation into mechanical and microstructural properties of polypropylene manufactured by selective laser sintering in comparison with injection molding counterparts, Mater. Des. 82 (2015) 37–45.

[5] A. Wegner, New polymer materials for the laser sintering process: polypropylene and others, Phys. Procedia 5 (2016) 1003–1012.

[6] D. Drummer, D. Rietzel, F. Künlein, Development of a characterization approach for the sintering behavior of new thermoplastics for selective laser sintering, Phys. Procedia 83 (2010) 533–542.

[7] L. Verbelen, S. Dadbakhsh, M. Van den Eynde, J.P. Kruth, B. Goderis, P. Van Puyvelde, Characterization of polyamide powders for determination of laser sintering processability, Eur. Polym. J. 75 (2016) 163–174.

[8] J. Schmidt, M. Sachs, S. Fanselow, M. Zhao, S. Romeis, D. Drummer, K. E. Wirth, W. Peukert, Optimized polybutylene terephthalate powders for selective laser beam melting, Chem. Eng. Sci. 156 (2016) 1-10.

[9] S. Arai, S. Tsunoda, R. Kawamura, K. Kuboyama, T. Ougizawa, Comparison of crystallization characteristics and mechanical properties of poly(butylene terephthalate) processed by laser sintering and injection molding , Mater. Des. 113 (2017) 214–222.

[10] O.R. Ghita, E. James, R. Davies, S. Berretta, B. Singh, S. Flint, K.E. Evans, High temperature laser sintering (HT-LS): an investigation into mechanical properties and

shrinkage characteristics of poly (ether ketone) (PEK) structures, Mater. Des. 61 (2014) 124–132.

[11] S. Berretta, K.E. Evans, O. Ghita, Processability of PEEK, a new polymer for high temperature laser sintering (HT-LS), Eur. Polym. J. 68 (2015) 243–266.

[12] J. Scheirs, T.E. Long, Modern polyesters: chemistry and technology of polyesters and copolyesters, Wiley, Chichester, 2003.

[13] J. Green, J. Chung, Flame retarding polybutylene terephthalate - properties, processing characteristics, and rheology, J. Fire Sci. 8 (1990) 254-265.

[14] A. Litzenburger, Criteria for, and examples of optimal choice of flame retardants. Polym. Polym. Compos. 8 (2000) 581–592

[15] S.K. Tiwari, S. Pande, S. Agrawal, S.M. Bobade, Selection of selective laser sintering materials for different applications, Rapid Prototyp. J. 21 (2015) 630-648.

[16] A.V. Borille, J.O. Gomes, D. Lopes, Geometrical analysis and tensile behaviour of parts manufactured with flame retardant polymers by additive manufacturing, Rapid Prototyp. J. 23 (2017) 169-180.

[17] A.R. Horrock, D. Price, Fire Retardant Materials, Woodhead Publishing, Cambridge, 2001.

[18] R. Smith, P. Georlette, I. Finberg, G. Reznick, Development of environmentally friendly multifunctional flame retardants for commodity and engineering plastics, Polym. Degrad. Stab. 54 (1996) 167-73.

[19] R. Pfeffer, R. N. Dave, D. Wei, M. Ramlakhan. Synthesis of engineered particulates with tailored properties using dry particle coating, Powder Technol. 117 (2001) 40-67.

[20] S. Dupin, O. Lame, C. Barrès, J.-Y. Charmeau, Microstructural origin of physical and mechanical properties of polyamide 12 processed by laser sintering, Eur. Polym. J. 48 (2012) 1611–1621.

[21] B. Caulfield, P.E. McHugh, S. Lohfeld, Dependence of mechanical properties of polyamide components on build parameters in the SLS process, J. Mater. Process. Technol. 182 (2007) 477–488.

[22] S. Ziegelmeier, F. Wöllecke, C. Tuck, R. Goodridge, R. Hague, Characterizing the bulk & flow behaviour of LS polymer powders. Proc. of the Solid Freeform Fabrications Symp., Austin, TX, (2013) 354–367.

[23] C. Yan, L. Hao, L. Xu, Y. Shi, Preparation, Characterisation and processing of carbon fibre/polyamide-12 composites for selective laser sintering, Compos. Sci. Technol. 71 (2011) 1834–1841.

[24] F.J. Vallejo, J.I. Eguiazábal, J. Nazábal, Solid state features and mechanical properties of PEI/PBT blends, J. Appl. Polym. Sci. 80 (2001) 885-892.

[25] N. Tomar, S.N. Maiti, Thermal and crystallization properties of PBT/ABAS blends, J. Appl. Polym. Sci. 113 (2009)1657-1663.

[26] S. Ziegelmeier, P. Christou, F. Wöllecke, C. Tuck, R. Goodridge, R. Hague, E. Krampe, E. Wintermantel, An experimental study into the effects of bulk and flow behaviour of laser sintering polymer powders on resulting part properties, J. Mater. Process. Technol. 215 (2015) 239–250.

[27] P.K. Jain, P.M. Pandey, P.V.M. Rao, Selective laser sintering of clay-reinforced polyamide, Polym. Compos. 31 (2010) 732–734.

[28] J. Bai, R.D. Goodridge, R.J.M. Hague, M. Song, Carbon nanotube reinforced Polyamide 12 nanocomposites for laser sintering Proc. of the Solid Freeform Fabrications Symp., Austin, TX, (2012) 98–107.

[29] M. Karevan, S. Eshraghi, R. Gerhardt, S. Das, K. Kalaitzidou, Effect of processing method on the properties of multifunctional exfoliated graphite nanoplatelets/polyamide 12 composites, Carbon 64 (2013) 122–131.

[30] B.V. Hooreweder, J.P. Kruth, High cycle fatigue properties of selective laser sintered parts in polyamide 12, CIRP Ann. Manuf. Technol. 63 (2014) 241–244.

[31] M. Vasquez, B. Haworth, N. Hopkinson, Methods for quantifying the stable sintering region in laser sintered polyamide-12, Polym. Eng. Sci. 53 (2013) 1230–1240.

[32] S. Griessbach, R. Lach, W. Grellmann, Structure-property correlations of laser sintered nylon 12 for dynamic dye testing of plastic parts, Polym. Test. 29 (2010) 1026–1030.

[33] T. Stichel, T. Frick, T Laumer, F. Tenner, T. Hausotte, M. Merklein, M. Schmidt, A round robin study for selective laser sintering of polyamide 12: microstructural origin of the mechanical properties Opt. Laser Technol. 89 (2017) 31-40.

[34] S. Xie, S. Zhang, F. Wang, H. Liu, M. Yang, Influence of annealing treatment on the heat distortion temperature of nylon-6/montmorillonite nanocomposites, Polym. Eng. Sci. 45 (2005) 1247–1253.

[35] M.H. Angela, C.J. Ellen, Improving mechanical performance of injection molded PLA by controlling crystallinity, J. Appl. Polym. Sci. 107 (2008) 2246-2255.

[36] H. Zarringhalam, N. Hopkinson, N.F. Kamperman, J.J. de Vlieger, Effects of processing on microstructure and properties of SLS nylon 12, Mater. Sci. Eng. A 435-436 (2006) 172–180.

[37] B.V. Hooreweder, D. Moens, R. Boonen, J.P. Kruth, P. Sas, On the difference in material structure and fatigue properties of nylon specimens produced by injection molding and selective laser sintering, Polym. Test. 32 (2013) 972–981.

[38] A.M. Rhoades, J. L.Williams, N. Wonderling, R. Androsch, J. Guo, Skin/core crystallinity of injection-molded poly(butylene terephthalate) as revealed by microfocus X-ray diffraction and fast scanning chip calorimetry, J. Therm. Anal. Cal. 127 (2017) 939-946.

[39] R.E. Lyon, R.N. Walters, S.I. Stoliarov, Screening flame retardants for plastics using microscale combustion calorimetry, Polym. Eng. Sci. 47 (2007) 1501–1510.

Chapter 4

Effects of short glass fiber content on material properties of laser sintered PBT

4-1. Introduction

Selective laser sintering (SLS), which is defined as a powder-bed fusion technology according to ISO/ASTM 52900; 2015, is mainly used for forming three-dimensional (3D) laminated moldings by repeatedly irradiating a thinly spread powder with a laser beam. In comparison to conventional methods, such as injection molding (IM), SLS has several advantages, namely, increased degree of design freedom, ease of handling complicated shapes and customizations, and fabrication in a short time [1].

Polyamides (polyamides 11 (PA11) and 12 (PA12)) are one kind of crystalline resin, and they are the most widely used as standard materials for SLS [2]. However, crystalline resins other than PA12 and PA11 are being actively researched, and some of those resins have been commercialized [3-9]. In a previous research [10], "copolymer PBT (cPBT)" (which has lower crystallization temperature than that of the homo-PBT used in [7]) was successfully used for SLS possible at a powder-bed temperature of 190 °C (as for commercial SLS apparatuses still in general use, maximum powder-bed temperature is fixed at around 200 °C [2]).

As for crystalline resins (including PBT) used for IM, to improve mechanical properties and heat resistance, it is normal to strengthen the neat materials by adding inorganic filler to them [11, 12]. The application range of such resins is thus expanding considerably. In particular, in the case glass fiber is used as the filler, a great many factors (such as fiber length, content, orientation, and strength as well as adhesion of resin and molding conditions used) [13-17] affect the properties of the IM-formed product. Furthermore, the phenomena involved in IM are complicated. In regard to SLS too, additions of glass beads [18, 19], glass fiber [20, 21], carbon fiber [22, 23], graphite platelets [24], alumina [25] and silicon carbide [26] as inorganic fillers have been

studied extensively; however, the effects of those fillers and filler contents on various characteristics of the bulk resin (including PA11 and PA12) have not been investigated as extensively. In particular, in the case of PBT, the effects of filler on powder and part properties on the properties of the powder and finished parts have only been studied sparingly. For the reasons described above, in a similar manner to IM, to expand the fields in which SLS is applied, it is necessary to fully understand the effects on various characteristics of the SLS product when inorganic fillers are combined with bulk resins. In general, as for SLS, layer thickness in the range of 0.10 to 0.15 mm is used [27, 28]; consequently, the long fibers used for IM are not used [29]. It is therefore necessary to investigate the effects of the addition of short fibers and its content on powder and part properties. In this study, which aims to meet that need, the effects of amount of added short glass fiber on powder properties, mechanical properties, thermal properties, and shrinkage of SLS specimens (when short glass fiber is added to cPBT powder resin developed in a previous study [10]) were investigated.

4-2. Experimental methods

4-2-1. Sample preparation

Material

The copolymer PBT (cPBT) powder (powder size of D50 was 78 μm) used in this study was formed by cryomilling (as described in a previous study [10]). In the case of selective laser sintering (SLS), generally, lamination layers with thickness of 0.10–0.15 mm are repeatedly formed [27, 28]; consequently, laying them uniformly is presumed to be difficult if continuous fibers or long fibers used for injection molding (IM) are added to the SLS powder. In the present study, 15, 30, 45, or 60 wt% of short-glass-fiber (SGF,

SS05C-404, Nitto Boseki Co., Ltd.) was added to cPBT resin powder. Distribution range of SGF length is shown in Fig. 1, and the SGF (with average fiber length of 99 μm, fiber diameter of 11 μm, and density of 2.6 g/cm^3) was treated with a silane coupling agent, and 0.1 wt% of hydrophobic silica (AEROSIL®RA200H; Evonik Industries) was added to the mixed powder. The cPBT powder, SGF, and silica were blended for 15 minutes by mixer (SKH-40CA, Misugi Ltd.). Scanning electron microscopy (SEM) images of the (a) cPBT powder [10] and (b) cPBT/30-wt%-SGF powder are shown in Fig. 2.

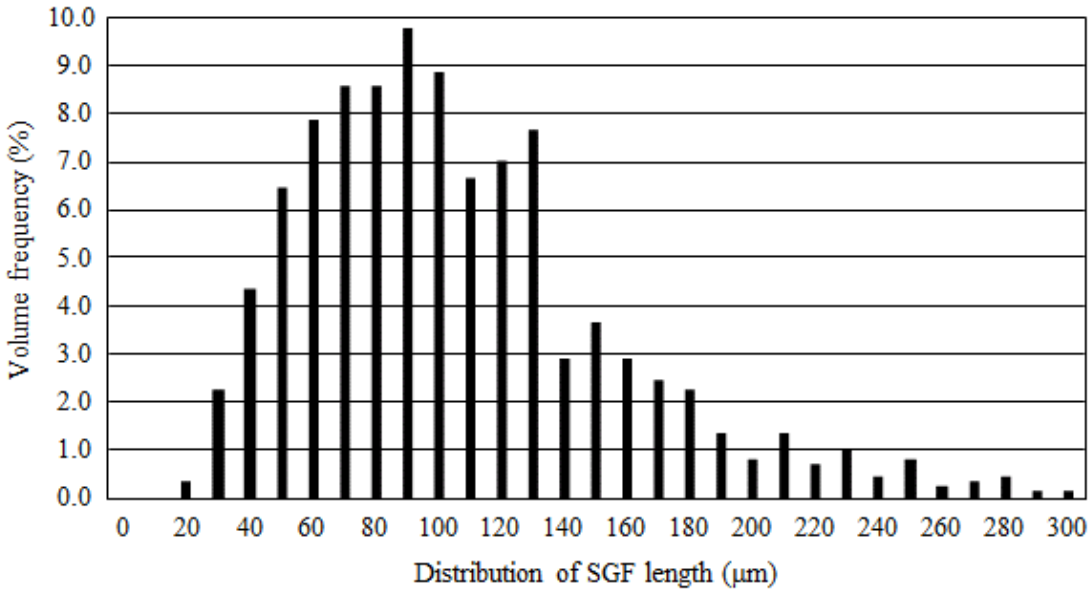

Fig. 1: Distribution of SGF length.

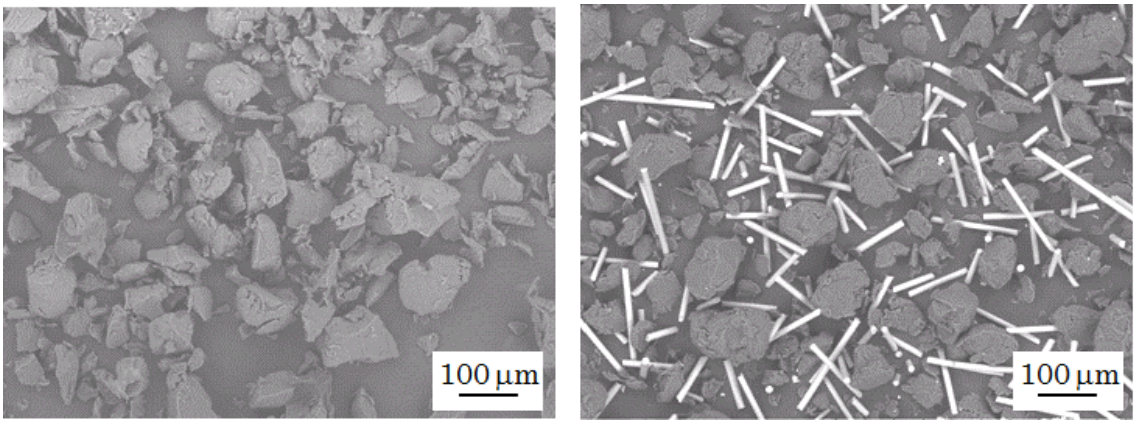

Fig. 2: SEM images of (a) cPBT-powder [10] and (b) cPBT/30-wt%-SGF composite powder.

Selective laser sintering (SLS)

An SLS machine (RaFaEl 300, Aspect Inc.) was used for fabricating the specimens. As the heat source for SLS, a carbon-dioxide laser (with wavelength of 10.6 µm and spot diameter of about 0.3 mm) was used. As for SLS, the parameters that influence the quality of the sintered specimens are laser power, scan rate, scan spacing, powder-bed temperature, feed temperature, and layer thickness [2]. Among those parameters, laser power was taken as the variable parameter used in this study and varied as eight values, namely, 5, 8, 11, 14, 17, 20, 25, and 30 W. The conditions under which the specimens were formed are listed in Table 1.

Table 1: Processing parameters for SLS of cPBT powder and cPBT-SGF composite powder.

Processing parameters	
Wavelength	10.6 μm
Laser beam diameter	0.3 mm
Fill and outline laser power	5, 8, 11, 14, 17, 20, 25, 30 W
Scan speed	5.0 m/s
Scan spacing	0.15 mm
Fill energy density	6.7, 10.7, 14.7, 18.7, 22.7, 26.7, 33.3, 40.0 kJ/m^2
Laser scan direction	Alternating bi-directional scan
Powder bed temp.	190 °C
Feed temp.	165 °C
Layer thickness	0.1 mm
Part piston temp.	180 °C

All parameters other than laser power are the same as those used in a previous study on cPBT [10]. As for SLS, it is known that the build direction of the fabricated specimen has a significant effect on its properties [2]. In the present study, as for the build direction, the x-direction is defined as the roller-movement direction, the y-direction is defined as the perpendicular surface direction (i.e., perpendicular to the direction in which the roller moves along the surface), and the z-direction is defined as the layer-thickness direction.

4-2-2. Evaluation methods

Powder flowability

As for SLS, flowability of the powder has a significant effect on the properties of the formed product. Flowability of the sample powders with 15-, 30-, 45-, and 60-wt% added short glass fiber (SGF) was evaluated in terms of Hausner ratio (HR), given as [30]

$$\mathrm{HR} = \frac{\rho_{tapped}}{\rho_{bulk}} \tag{1}$$

where ρ_{tapped}(tapped density) and ρ_{bulk}(bulk density)were measured by powder-characteristics tester (PT-X, Hosokawa Micron Corporation) at 25 °C.

Differential-scanning calorimetry (DSC)

Isothermal-crystallization differential-scanning calorimetry (DSC) (EXSTAR 6000, Seiko Instruments Inc.) was performed to evaluate the crystallization time of the cPBT powder and SGF composites powder. In detail, the powders were heated to 250 °C, held for 10 min at that temperature, and then cooled to 190 °C, at which the heat of crystallization was measured. Crystallization half time was calculated as the time taken for the heat of crystallization to reach 50 % of the value for complete crystallization.

DSC (Q2000, TA Instruments) was carried out to determine the melting point, crystallization temperature, and degrees of crystallinity of the SLS specimens (cPBT/15-wt%-SGF, cPBT/30-wt%-SGF, cPBT/45-wt%-SGF, and cPBT/60-wt%-SGF). Degree of crystallinity (χ) is given in terms of heat of fusion (ΔH), perfect-crystal heat of fusion (ΔH_m^o), and mass fraction of fiber (f) as [31]

$$\chi(\%) = \frac{\Delta H}{\Delta H_m^o \times (1 - f)} \times 100 \quad (2)$$

In this study, ΔH_m^o was taken as 145.5 J/g [32, 33]. The SLS specimens were cut from the central portion of flexural test pieces. The DSC specimens (with assumed weight of 5 ± 0.5 mg) were measured under increasing temperature from 5 to 300 °C at a rate of 10 °C/min and nitrogen flow rate of 40 mL/min.

Mechanical testing

To evaluate the mechanical properties of the SLS specimens with cPBT, cPBT/15-wt% SGF, cPBT/30-wt% SGF, cPBT/45-wt% SGF, and cPBT/60-wt% SGF,

tensile tests, flexural tests, and Charpy impact-strength tests were performed. The tensile-testing specimens were taken as "type A" specified in ISO3167; 1993 [total length: 170 mm (x-direction); parallel-portion length (x-direction): 80 mm; thickness: 4 mm (z-direction)]. As for the tensile tests, performed on a 5500RF, Instron Corporation, according to ISO527-1 and -2; 2012, testing speed was 50 mm/min, and distance between the clamps was 115 mm. As for the flexural tests, performed on the same tensile tester according to ISO178; 2001, with test-specimen size of 80 (x-direction) × 10 (y-direction) × 4 mm (z-direction), testing speed was 2 mm/min, and the distance between the fulcrums was 64 mm. As for the Charpy-impact-strength tests performed on an AG-100kNX, Shimadzu Corporation, in accordance with ISO179–1; 2010, a notch was formed in a test specimen with the same shape as the flexural test specimens. With an energy of 0.5 J, the hammer weight was applied so that the impact was in the edgewise direction. All the strength tests were performed with n = 5 (minimum), and average strength and elongation at break were estimated.

Scanning electron microscopy (SEM)

The fracture surfaces after the tensile tests on the cPBT, cPBT/15-wt%-SGF, cPBT/30-wt%-SGF, cPBT/45-wt%-SGF, and cPBT/60-wt%-SGF SLS specimens were observed by SEM (model S-3700N, Hitachi High-Technologies Corporation) at acceleration voltage of 15 kV.

Optical microscopy

To evaluate the porosity of the SLS specimens, the central portions (10 × 4 mm) of the SLS specimens with cPBT/15-wt%-SGF, cPBT/30-wt%-SGF, cPBT/45-wt%-SGF, and cPBT/60-wt%-SGF were cut in the direction of layer thickness, and after embedding the specimens in epoxy resin, near-center portions of the SLS specimens

were polished at intervals of 0.5 mm and observed by microscope (VHX-2000, Keyence Corporation). After that, porosity was calculated by image processing (WinROOF, Mitani Corporation).

Measurement of SGF length

8-10 g of the sample powders with 15-, 30-, 45-, and 60-wt% added SGF and the SLS specimens with cPBT/30-wt%-SGF, cPBT/45-wt%-SGF, and cPBT/60-wt%-SGF were kept at 700 °C for 1.5 h, respectively, to burn off the cPBT resin. The lengths of the residual SGFs (at least 800) were measured by optical microscope (VHX-5000, Keyence Corporation).

Micro-computer tomography (micro-CT)

Orientation of the SGFs in the SLS specimens was determined by micro-computer tomography (micro-CT) measurements (inspeXio SMX-100CT, Shimadzu Corporation). The flexural test piece of the cPBT/30-wt%-SGF was cut in the middle portion, and a 2×2-mm area (x-y face) and 2×1.8-mm areas (y-z face and z-x face) were measured under the following conditions: X-ray tube voltage of 60 kV, X-ray tube current of 60 μA, and voxel size of 4 μm.

Dynamic mechanical analysis (DMA)

Storage elastic modulus (E'), loss elastic modulus (E"), and a loss factor (tan δ=E'/E") of the SLS specimens (size: 20×5×1 mm) with cPBT, cPBT/15-wt%-SGF, cPBT/30-wt%-SGF, cPBT/45-wt%-SGF, and cPBT/60-wt%-SGF were measured by DMA (Rheogel-E4000, UBM Corporation) at measurement frequency of 1 Hz. The temperature range of DMA was –50 to 200 °C, and the rate of temperature increase was 5 °C/min.

Heat deflection temperature (HDT) testing

Heat deflection temperature (HDT) of the SLS specimens with cPBT, cPBT/15-wt%-SGF, cPBT/30-wt%-SGF, cPBT/45-wt%-SGF, and cPBT/60-wt%-SGF was measured by HDT tester (6A-2, Taiyo-seiki Co., Ltd.). The HDT tests were performed according to standard ISO75-1,-2; 2004 (JIS K7191-1,-2; 2007) in flatwise mode under bending stress of 1.82 MPa.

Thermomechanical analysis (TMA)

The cPBT, cPBT/15-wt%-SGF, cPBT/30-wt%-SGF, cPBT/45-wt%-SGF, and cPBT/60-wt%-SGF SLS specimens [sample size: 10 mm (x-direction)×5 mm (y)×5 mm (z)] were measured by TMA (TMA4000SA, BrukerAXS Ltd.) according to standard ISO11359-2. A compressive load of 26 mN (face pressure: 4±0.1 kPa) was applied by a probe positioned about 3 mm from the x-y surface. As for the measurement environment, nitrogen gas was flowed at a rate of 100 ml/min, test temperature range was 25 to 200 °C, and rate of temperature increase was 5 °C/min. Before the TMA measurements, the specimens were not annealed. The linear-expansion coefficient, under a temperature not in the range near the glass-transition temperature (Tg), was calculated. Coefficients of linear expansion at temperature under Tg ($\alpha 1$) and temperature above Tg ($\alpha 2$) were calculated in the temperature ranges of 25-40 °C and 70-200 °C, respectively.

Shrinkage measurements

Shrinkage in SLS is strongly influenced by laser irradiation stage and cooling stage. In a design (CAD) model, the size of the samples was 200 × 10 × 10 mm, the 200-mm edge was aligned in the x-direction. Shrinkage ratio (S) of the cPBT,

cPBT/15-wt%-SGF, cPBT/30-wt%-SGF, cPBT/45-wt%-SGF, and cPBT/60-wt%-SGF SLS specimens was measured in the x-direction. S is defined as [34]

$$S = \frac{L1 - L2}{L1} \times 100 \quad (3)$$

where *L1* is the nominal value, and *L2* is the measured value after sintering and cooling. *S* was measured by using Vernier calipers.

4-3. Results and discussion

4-3-1. Composite powder properties

Powder flowability

To improve the flowability of copolymer PBT (cPBT) resin powder, 0.1-wt% silica was added to the powder, and selective laser sintering (SLS) processability was then evaluated [10]. Evaluated Hausner ratios (HRs) in the present study for additions of 15-, 30-, 45-, and 60-wt% short-glass-fiber (SGF) to cPBT powder are plotted in Fig. 3. In this figure, the results in the cases with or without 0.1-wt% added silica are plotted. As the amount of added SGF increases, HR increases. In particular, in the case that 0.1-wt% silica was not added, at 30-wt% added SGF and above, HR did not drop sufficiently from the sieve with hole diameter of 0.5 mm, and HR values could not be obtained. It is therefore clear that adding 0.1-wt% silica significantly improves flowability even in the case of the SGF-added composite powder. In other words, addition of 0.1-wt% silica to cPBT-SGF composite powder reduces not only the attractive force between cPBT particles but also that between the cPBT particles and the

SGFs. Moreover, the flowability of the SGF-added composite powder with 0.1-wt% silica added is better than that of the cPBT powder without 0.1-wt% silica.

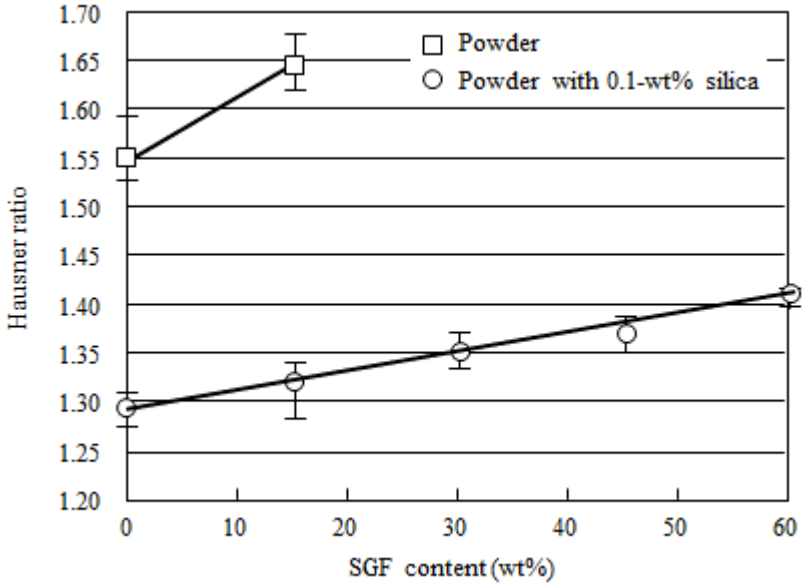

Fig. 3: Comparison of HRs of cPBT powder (with or without 0.1-wt% added silica) with SGF additions of 15, 30, 45, and 60 wt%.

Crystallization time

In the case of SLS, the process window is extremely important, and variation of the crystallization rate significantly affects SLS processability and accuracy [2]. In a previous study [10], cPBT powder was successfully sintered by using a powder-bed temperature of 190 °C. In accordance with that previous study [10], to determine whether SGF-added powder can also be set at 190 °C, crystallization time was estimated by isothermal-crystallization DSC. Crystallization half times at 190 °C of cPBT with SGF additions of 15, 30, 45, and 60 wt% are compared in Fig. 4.

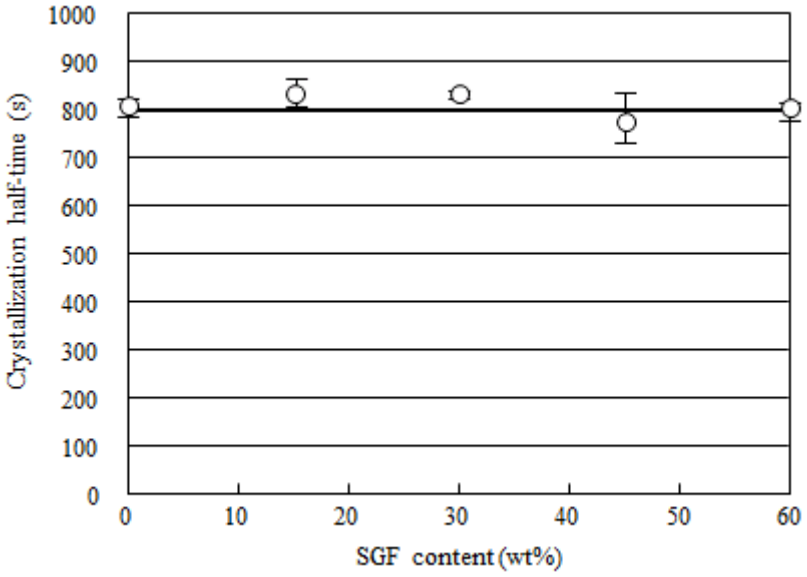

Fig. 4: Comparison of crystallization half time at 190 °C of cPBT powder with SGF additions of 15, 30, 45, and 60 wt%.

According to the figure, the powders exhibit about the same crystallization half times regardless of the amount of added SGF. It was reported by Park et al. [35] that glass fiber acts as a nucleating agent in PBT pellets containing glass fiber with fiber diameter of 10 μm and average length of 0.30 mm. Furthermore, it was reported by Yan et al. [22] that composite powder composed of surface-treated carbon fibers (CF) (average fiber length of 38 μm) and PA12 shows crystallization behavior, and the CFs act as nucleating agents. However, according to the present study, SGF does not act as a nucleating agent for cPBT. This discrepancy in findings is presumed to be due to the fact that the interaction at the interface between cPBT and SGF has a weaker influence than the equivalent interactions in the cases of other above-mentioned material combinations. In a previous study [10], it was found that contamination material generated during pulverizing of cPBT pellets act as crystallization nucleating agents in

cPBT powder. According to the results of the present study, SGF addition did not have the additional effect of a nucleating agent. It can thus be supposed that the SGF addition does not cause a change in the morphology. It can thus be supposed that the SGF addition does not cause a change in the morphology of the cPBT.

4-3-2. Characteristics of laser sintered specimens

Mechanical properties

Tensile strength, elongation at break, flexural strength, and notched Charpy impact strength of the SLS specimens with copolymer PBT (cPBT) only and cPBT with 15-, 30-, 45-, and 60-wt% added SGF under assumed laser energy densities of 6.7, 10.7, 14.7, 18.7, 22.7, 26.7, 33.3, and 40.0 kJ/m^2 are plotted in Fig. 5. According to these plots, in the cases of added SGF, as in the case of cPBT only, all mechanical properties are maximized at a certain laser energy density. As the amount of added SGF increases, the laser energy densities required for maximizing the mechanical properties increase. Viscosity and surface energy at melting of the cPBT resin (which affect adhesion with SGF) significantly affect the mechanical strength of the SLS specimens, so increased the laser energy density is supposed to be a necessary condition under which viscosity of the resin is further lowered. Moreover, in the case of SLS of cPBT powder, according to a previous study [10], when laser energy density is increased, the mechanical properties of the SLS specimen are degraded by a decrease in molecular weight of cPBT (namely, thermal degradation of cPBT). It is therefore considered that in the case SGF is added to the cPBT powder, the lowering of mechanical strength with increasing laser energy density is attributed to the decrease in the molecular weight of the PBT resin.

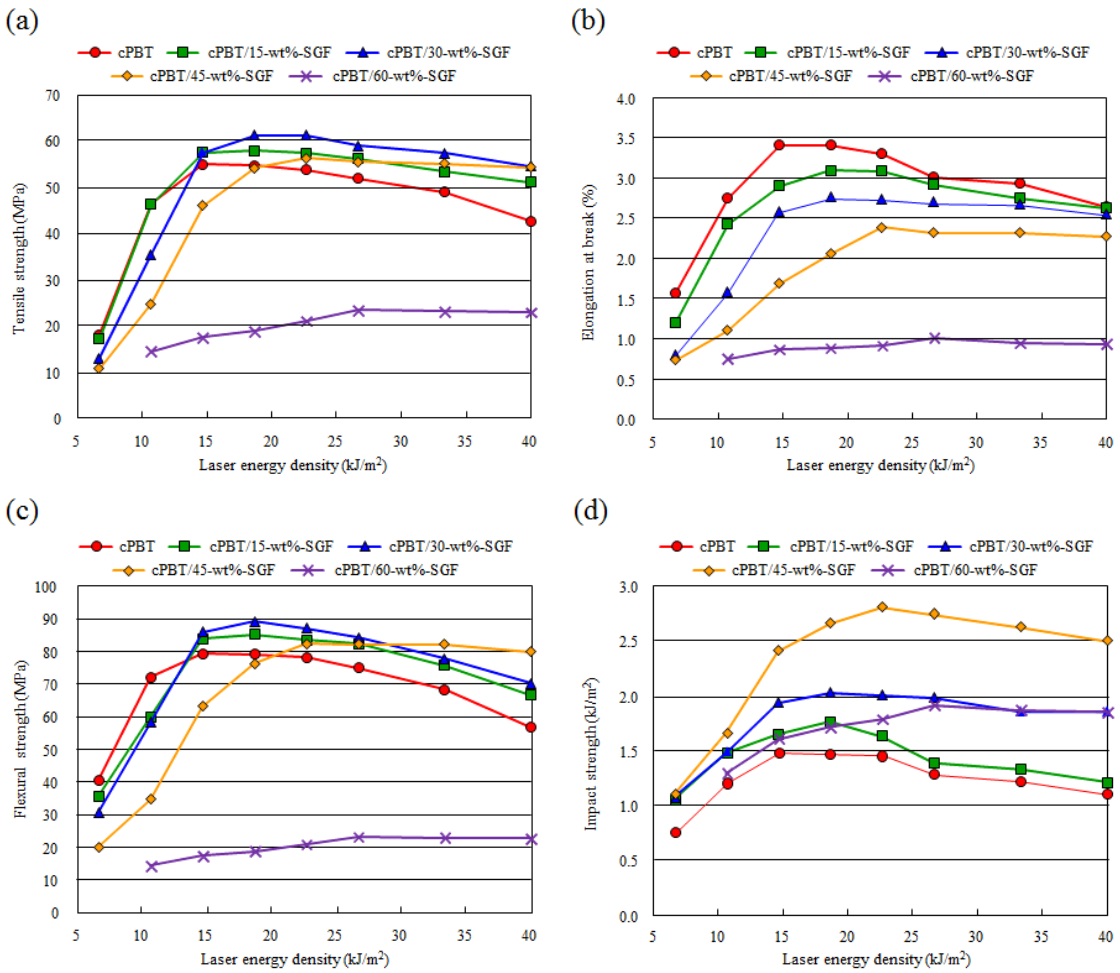

Fig. 5: Comparison of mechanical properties of SLS specimens with cPBT, and cPBT/15-wt%-SGF, cPBT/30-wt%-SGF, cPBT/45-wt%-SGF, and cPBT/60-wt%-SGF under assumed laser energy densities of 6.7, 10.7, 14.7, 18.7, 22.7, 26.7, 33.3, and 40.0 kJ/m^2: (a) tensile strength, (b) elongation at break, and (c) flexural strength, and (d) notched Charpy impact strength.

With SGF amount taken as a parameter, maximum tensile strength, elongation at break, and flexural strength are increased by SGF addition up to 30 wt%. However, it is clear that in contrast to the decrease in those properties at SGF addition of 45 wt%, Charpy impact strength increases up to SGF addition of 45 wt% and decreases at SGF addition of 60 wt%. In particular, in the case of SGF addition of 60 wt%, in contrast to

the considerably low values of tensile strength and flexural strength, impact strength is at the same level as in the the case of SGF addition of 30 wt%. It is thus clear that increasing the amount of SGF added significantly improves impact strength of the SLS specimens. Moreover, as the amount of added SGF is increased, tensile strain (elongation) at failure decreases. In the case of injection molding (IM) using crystalline resin, addition of GF or SGF significantly affects mechanical properties, and in accordance with the ratio of added GF or SGF, mechanical properties are improved [14, 36, 37]. Furthermore, according to Yan et al. [22], who evaluated the flexural properties of SLS specimens while taking amount of carbon fiber (CF) (preliminarily surface processed) added to PA12 resin powder as a parameter, flexural strength was increased by adding 50-wt% CF, and that result differs from the result of the present study. In the cases of IM and SLS, adhesion between the resin and fiber significantly affects mechanical properties of the formed product [22]. Moreover, as for the characteristic feature of SLS, relatively large porosity inevitably remains, and that porosity causes degradation of mechanical properties [38]. Hereafter, the results of a detailed evaluation of the above-described factors (adhesion of cPBT resin and SGF, porosity) are presented, and specimens sintered under laser energy density optimized to maximize mechanical properties are compared.

Observation of fracture surface

SEM images of the fracture surfaces of the (a) cPBT, (b) cPBT/15-wt%-SGF, (c) cPBT/30-wt%-SGF, (d) cPBT/45-wt%-SGF, and (e) cPBT/60-wt%-SGF SLS specimens are shown in Fig. 6.

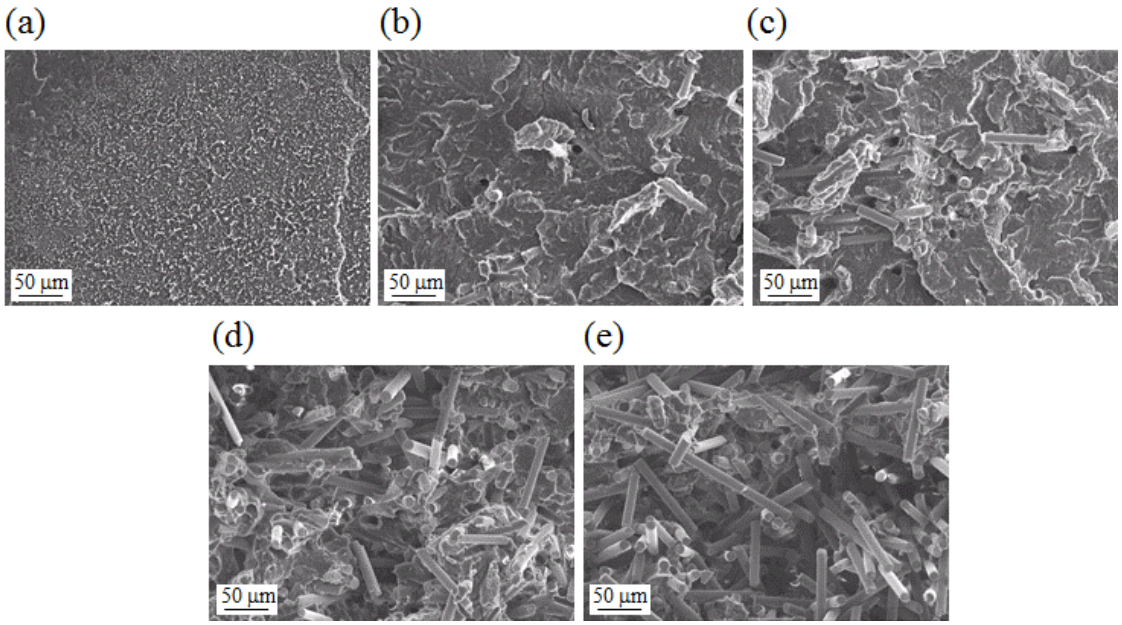

Fig. 6: SEM images of fracture surfaces of SLS specimens: (a) cPBT, (b) cPBT/15-wt%-SGF, (c) cPBT/30-wt%-SGF, (d) cPBT/45-wt%-SGF, and (e) cPBT/60-wt%-SGF.

The fracture surface of the cPBT specimen [image (a)] has a ductile-fracture surface morphology that extends as a fine fibrillar form compared to that of the specimens containing SGF. On the contrary, in the case of the fracture surfaces of the SGF-added specimens, as the proportion of SGF increases, many traces of pulled-out fibers can be seen. In particular, in the case of the specimen with 15-wt% SGF [image (b)], the cPBT resin exists around the SGF; in contrast, with at 30-wt% SGF and over [images (c), (d), and (e)], the cPBT resin around the SGF tends not to adhere. Moreover, as the proportion of added SGF increases, the laser energy density for maximizing mechanical properties also increases. It is possible that the increased the laser energy density lowers the effect of the silane treatment on the SGF surfaces with enhancing thermal degradation of the cPBT. The resulting weak adhesion between cPBT resin and SGF found is one difference compared with the results reported by Yan et al. [22].

Evaluation of porosity

Cross-sectional optical-microscope images of the (a) cPBT, (b) cPBT/15-wt%-SGF, (c) cPBT/30-wt%-SGF, (d) cPBT/45-wt%-SGF, and (e) cPBT/60-wt%-SGF SLS specimens are shown in Fig. 7, and the porosities of the specimens are plotted in Fig. 8.

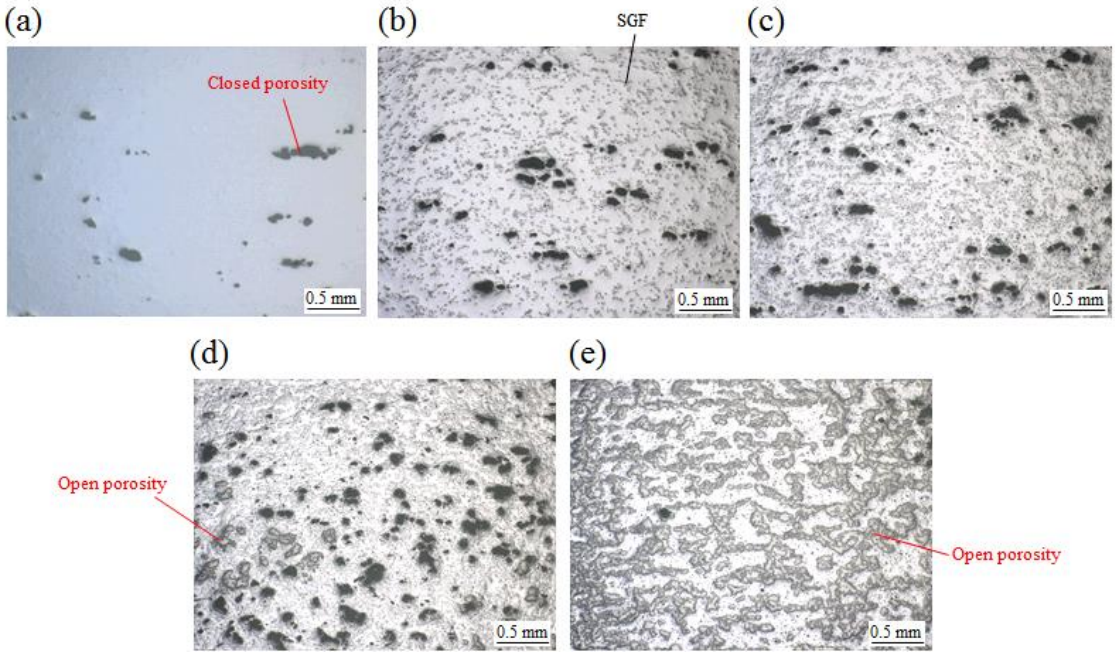

Fig. 7: Cross-sectional observation images by optical microscope of SLS specimens: (a) cPBT, (b) cPBT/15-wt%-SGF, (c) cPBT/30-wt%-SGF, (d) cPBT/45-wt%-SGF, and (e) cPBT/60-wt%-SGF.

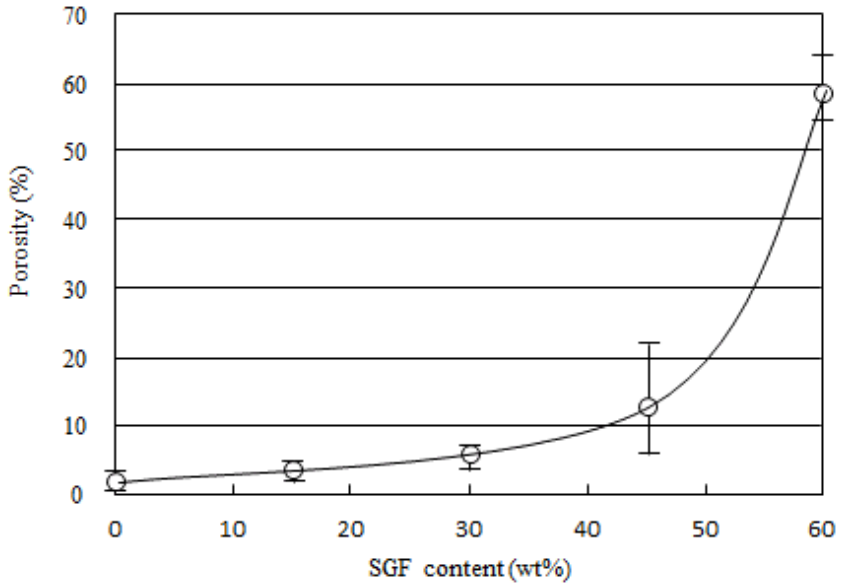

Fig. 8: Comparison of porosities of SLS specimens with cPBT, and cPBT/15-wt% SGF, cPBT/30-wt%-SGF, cPBT/45-wt%-SGF, and cPBT/60-wt%-SGF.

As the amount of added SGF increases, porosity increases gradually, and above SGF addition of 45 wt%, porosity increases dramatically. Moreover, above SGF addition of 45 wt%, "open porosity" can be seen [images (d) and (e)], and at SGF addition of 60 wt%, the greater part of the cross section is taken up by open porosity [image (e)]. According to reports by Childs et al. [20] and Wang et al. [24], in the case of SLS, adding inorganic fiber increases porosity, and the results of the present study are consistent with that phenomenon. Moreover, Ziegelmeier et al. [39] reported that the flowability of resin powder significantly affects the strength of SLS specimens. In the present study, as explained in subection ''Flowability'', as the amount of added SGF is increased, flowability becomes degraded. It is thus highly likely that the degraded flowability is one of the factors that increase the amount of porosity. Moreover, when the amount of SGF is increased, the individual SGFs become intertwined, and insufficient melted resin flows between the SGFs, and that resin insufficiency is the

reason porosity increases. In particular, in the case of the 60-wt%-SGF specimen, that effect is considerable.

Furthermore, it is supposed that another reason that the porosity is increased by adding SGF is that the adhesion of cPBT resin and SGF is weak. It can therefore be considered that in contrast to the case of IM [14, 36, 37], in the case of SLS, the rate of improvement in mechanical strength due to addition of SGF is very low because the increasing amount of porosity has a considerable countering effect on the effect of the SGF addition.

Observation of average SGFs and distribution

The residual distributions of SGF length in the 30-wt%-SGF, 45-wt%-SGF, and 60-wt%-SGF cPBT powder samples and SLS specimens are compared in Fig. 9.

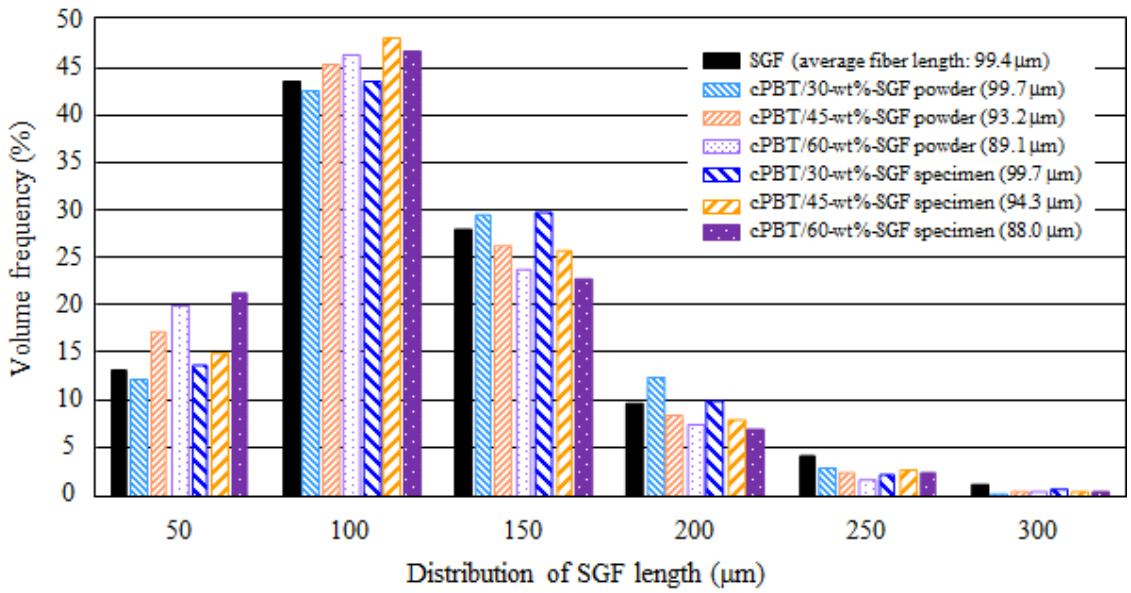

Fig. 9: SGF distribution of the composite cPBT powder with SGF additions of 30, 45, and 60 wt% and SLS specimens with cPBT/30-wt%-SGF, cPBT/45-wt%-SGF, and cPBT/60-wt%-SGF.

When the amount of added SGF was 45 wt% or more, the long SGFs were broken during the mixing to prepare the blended powders, the ratio of short-length fibers increased, and average fiber length decreased. In particular, average SGF length was decreased after blending, namely, by 5 to 6 % for the 45-wt%-SGF SLS specimens and 10 to 11 % for the 60-wt%-SGF SLS specimens. On the other hand, when the amount of added SGF was 30 wt%, average SGF lengths in the cases of the SLS specimens and the blended powders after the mixing of the cPBT powder, SGF, and silica hardly differ in comparison with those in the case of the SGFs alone. However, when fibers with length of more than 200 μm are compared, it becomes clear that the amount of such SGFs in the blended powders is lower than that before mixing. Also, as for the blended powder and SLS specimens, the distributions of SGFs do not significantly differ. It can thus be understood that breakage of SGFs does not occur during the processes for laying the composite powder with rollers and for laser irradiation.

It has been reported that in the case of IM, average fiber length decreases significantly, due to mutual interference between the screw and glass fiber, and fiber-length distribution has a substantial influence on mechanical properties (i.e., tensile strength, flexural strength, and impact strength) [40]. As in the case of the IM specimens, in the case of the SLS specimens, fiber-length distribution is thought to significantly influence mechanical characteristics. That is, in the present study, it was revealed that in regard to mechanical properties resulting from addition of SGF, in the case of SGF addition of up to 30 wt%, the effect of fiber breakage is low, whereas in the case of SGF addition above 45 wt%, it is significant and becomes greater as SGF content increases.

Observation of orientation of SGFs in each direction

Micro-CT images of the cPBT/30-wt%-SGF specimen in the (a) XY plane, (b) YZ plane, and (c) ZX plane are shown in Fig. 10.

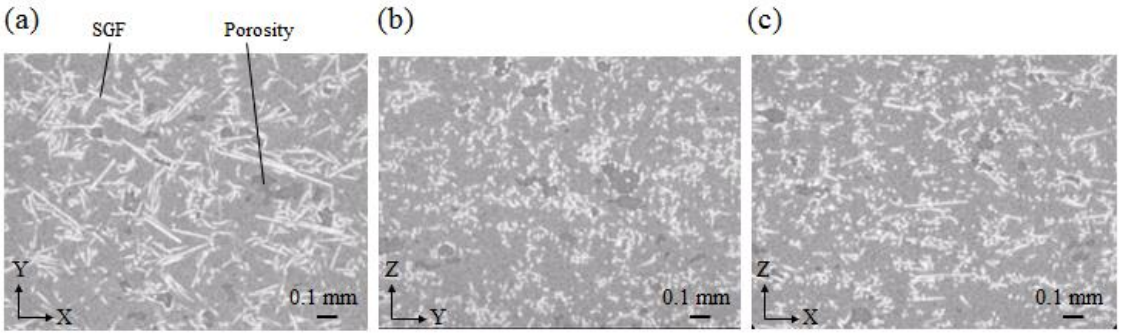

Fig. 10: Comparison by micro-CT images of cPBT/30-wt%-SGF specimen: (a) XY plane, (b) YZ plane, and (c) ZX plane.

It is clear from these images that SGF easily aligns in the x-direction (in which the roller moves) and that relatively long SGFs align in this manner. Moreover, the powder was laid down and SLS processed in 0.1-mm-thick layers, so no long fibers are aligned in the z-direction. According to micro-CT measurements on an SLS specimen composed of PA12 and CF by Jansson et al. [23], the CFs easily align in the direction that the blade moves. Although it is thought that the powder compacting force of the roller is weaker than that of the blade, the results of this study confirmed that the roller tends to arrange the SGFs in the direction it is moving. Fung et al. [17] reported tensile properties in the case that 30-wt%-SGF was added to PBT resin by changing the gate position of formed tensile-test pieces. According to their results, even in the case that the gate position was aligned perpendicularly to the direction of tension, tensile strength increased 1.3 times in comparison with the case that SGF was not added [17]. However, as for the cPBT/30-wt%-SGF specimen formed by SLS in the present study, the rate of

increase in tensile strength is much lower regardless of the fact that the fibers align easily in the x-direction and did not degrade. Therefore, in the case of SLS, particularly from the viewpoint of mechanical properties, it was confirmed that porosity as well as adhesion between SGF and PBT are major problems. Moreover, according the above-described results (namely, fracture-surface observation, porosity evaluation, and observation of average fiber length after SLS processing and SGF alignment), in the case of the SGF-added SLS specimens, porosity, fiber length, and adhesion between cPBT resin and SGF have weaker effects on impact strength than on tensile strength and flexural strength. This finding is in contrast with the finding that porosity, fiber length, and adhesion between cPBT and SGF have significant effects on the tensile and flexural properties of the SLS specimens.

DMA evaluation

Results of dynamic mechanical analysis (DMA) evaluation of storage elastic modulus and tanδ of the cPBT, cPBT/15-wt%-SGF, cPBT/30-wt%-SGF, cPBT/45-wt%-SGF, and cPBT/60-wt%-SGF SLS specimens are shown in Figs. 11(a) and (b), respectively.

In the case of SGF addition of 45 wt%, storage elastic modulus increases with increasing temperature from room temperature upwards. Moreover, in the case SGF addition of 60 wt%, at room temperature, it is about the same as that in the case of SGF addition of 15 wt%; in contrast, at higher temperature, it becomes closer to the value in the case of SGF addition of 45 wt%. This result is explained by the fact that the porosity of the 60-wt%-SGF SLS specimen has a much stronger effect on storage elastic modulus than that of the decrease of average fiber length. In addition, glass-transition temperature (Tg) does not significantly change with addition of SGF. This result is

thought to be due to the fact that mutual interaction at the interface between cPBT and SGF is weak.

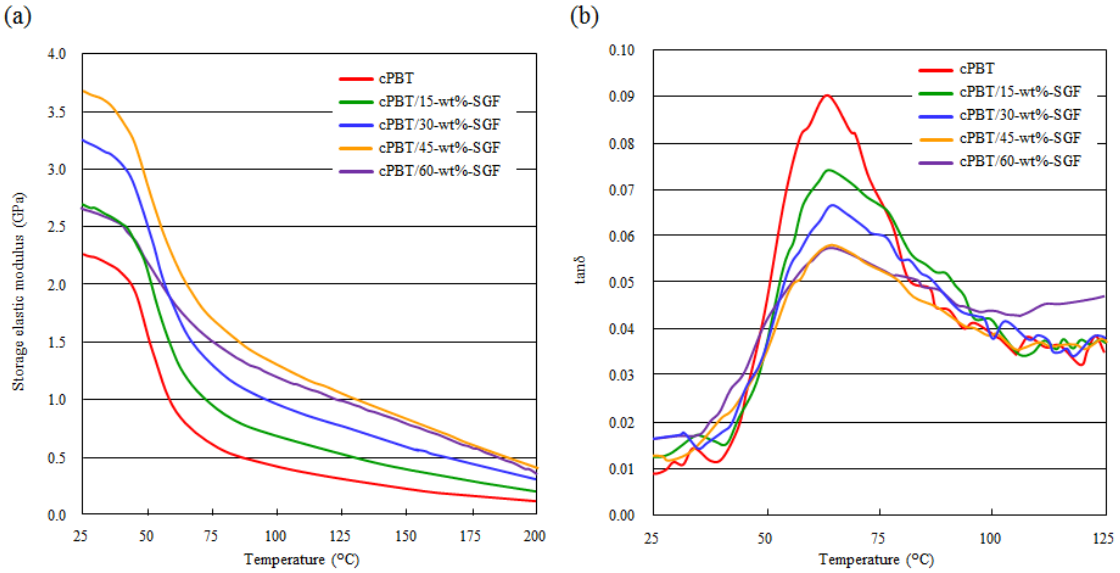

Fig. 11: Results of DMA evaluation of specimens with cPBT, cPBT/15-wt%-SGF, cPBT/30-wt%-SGF, cPBT/45-wt%-SGF, and cPBT/60-wt%-SGF: (a) storage elastic modulus and (b) tanδ.

Thermal properties

Heat deflection temperature (HDT) of the cPBT, cPBT/15-wt%-SGF, cPBT/30-wt%-SGF, cPBT/45-wt%-SGF, and cPBT/60-wt%-SGF SLS specimens is plotted in Fig. 12.

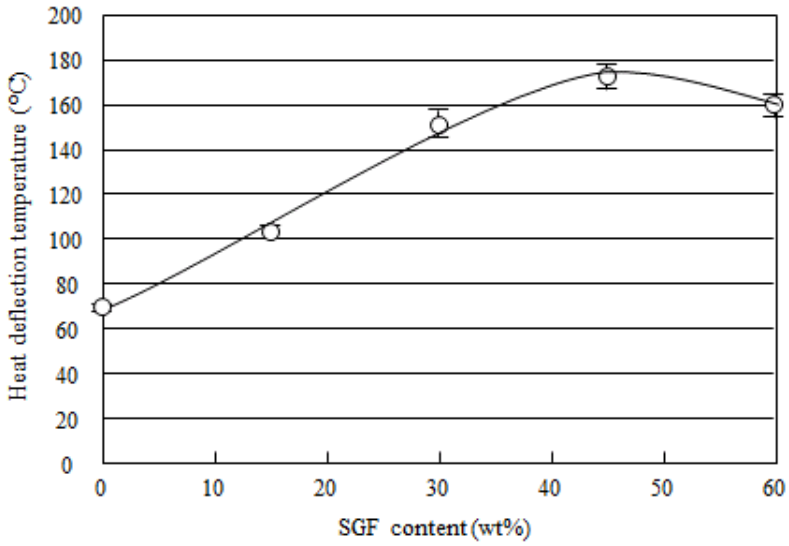

Fig. 12: Comparison of heat deflection temperature (HDT) of cPBT, cPBT/15-wt%-SGF, cPBT/30-wt%-SGF, cPBT/45-wt%-SGF, and cPBT/60-wt%-SGF specimens.

As the ratio of added SGF increases, HDT increases; in particular, in the case of cPBT/45-wt%-SGF, HDT is maximum, and in the case of cPBT/60-wt%-SGF, HDT falls slightly. In particular, in the case of the highest HDT (i.e., PBT/45-wt%-SGF), HDT increased by 103.2 °C compared to that of no added SGF. In other words, in contrast to the effect of SGF addition on mechanical properties, a significant stiffening effect (i.e., increased HDT) by SGF addition is shown. Therefore, in a similar manner to the DMA results, the HDT results indicate that SGF addition significantly enhances the elastic modulus at high temperature. According to Thomason, et al. [36], who performed a study on HDT in which amount of SGF addition to PA66 subjected to injection molding was taken as a parameter, HDT saturated at GF addition of 10 wt%, and the difference between the melting point of PA66 and HDT was around 20 °C. On the other hand, in the present study, even for SGF addition of 45 wt%, the difference between HDT and the melting point of the cPBT SLS specimens (209.9 °C) was

37.3 °C. Although the difference between the present HDT results and previously reported ones is supposed to be due to the effect of different fiber lengths, in a similar manner to the results concerning mechanical properties, porosity, fiber length, and adhesion between cPBT and SGF are also supposed to affect HDT. The results of the thermomechanical analysis (TMA) evaluation are shown in Fig. 13.

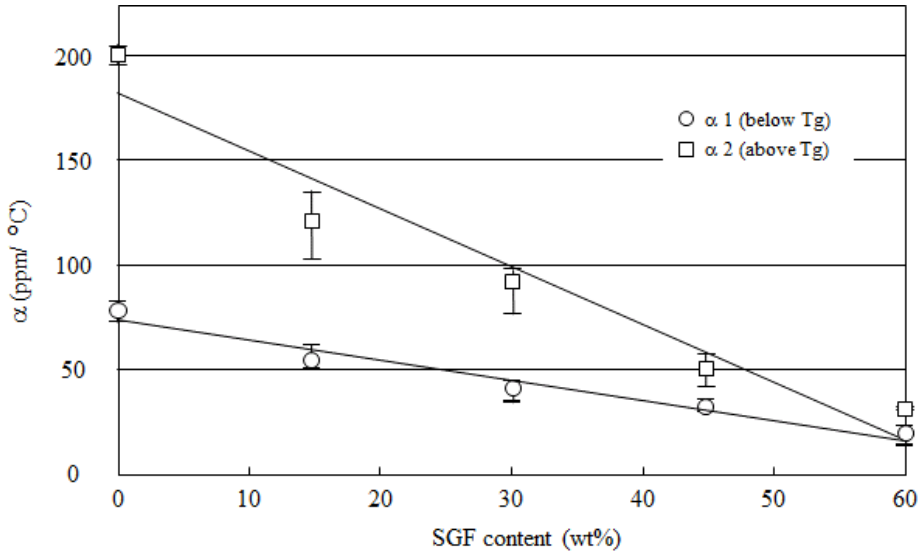

Fig. 13: Comparison of linear-expansion coefficient below and above glass transition temperature (Tg) with cPBT, cPBT/15-wt%-SGF, cPBT/30-wt%-SGF, cPBT/45-wt%-SGF, and cPBT/60-wt%-SGF specimens.

As the amount of SGF addition is increased, the linear-expansion coefficients of the SLS specimens in the regions above and below Tg, namely, $\alpha 1$ and $\alpha 2$, respectively, both decrease, and the effects of adding SGF on $\alpha 1$ and $\alpha 2$ do not significantly differ. In particular, up to SGF addition of 60 wt%, porosity increases and average fiber length decreases (as mentioned previously), so mechanical properties are significantly degraded; however, in comparison with the linear-expansion coefficient in the case that

SGF was not added, linear-expansion coefficient decreased by 76 % in $\alpha 1$ and 85 % in $\alpha 2$, respectively. From this significant result, it is supposed that (i) fiber orientation in the x-direction also has a significant reduction effect on the linear-expansion coefficient and (ii) increased porosity and decreased average fiber length with increasing SGF addition may not have a significant reduction effect on the linear-expansion coefficient.

Shrinkage evaluation

Shrinkage of the cPBT, cPBT/15-wt%-SGF, cPBT/30-wt%-SGF, cPBT/45-wt%-SGF, and cPBT/60-wt%-SGF SLS specimens is plotted in Fig. 14.

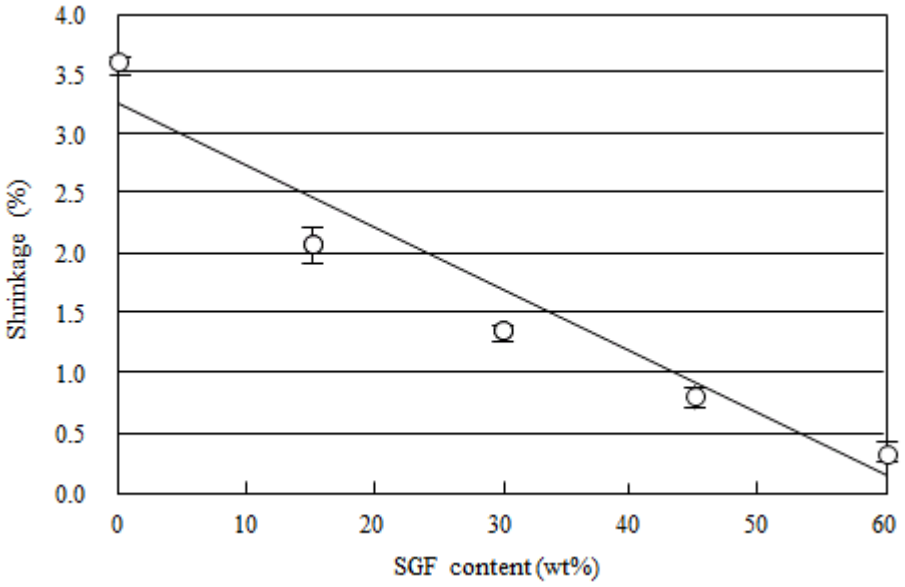

Fig. 14: Comparison of shrinkage of cPBT, cPBT/15-wt%-SGF, cPBT/30-wt%-SGF, cPBT/45-wt%-SGF, and cPBT/60-wt%-SGF specimens.

It is clear that shrinkage in SLS process depends on SGF-addition ratio and that of the SGF specimens in the direction in which the fibers tend to orientate decreases. In particular, in the case of 60-wt%-SGF addition, in comparison with the case of no SGF

addition, the shrinkage drops to less than one-tenth. Moreover, as also shown by the TMA results, a significant reduction effect by SGF addition was demonstrated. As for shrinkage during SLS, increased porosity and decreased average fiber length with increasing SGF addition may not have a significant reduction effect on shrinkage because SGF orientation has a significant effect (in a similar manner to the TMA results).

Crystallization characteristics

The results of an evaluation of degree of crystallization of the cPBT, cPBT/15-wt%-SGF, cPBT/30-wt%-SGF, cPBT/45-wt%-SGF, and cPBT/60-wt%-SGF SLS specimens are listed in Table 2.

Table 2: Results of evaluation of melting point, crystallization temperature, and degree of crystallization of SLS specimens: cPBT, cPBT/15-wt%-SGF, cPBT/30-wt%-SGF, cPBT/45-wt%-SGF, and cPBT/60-wt%-SGF.

	Tm (°C)	Tc (°C)	Degee of crystallinity (%)
cPBT	209.9	169.0	34.8
cPBT/15-wt%-SGF	209.2	168.9	34.8
cPBT/30-wt%-SGF	209.5	169.5	35.0
cPBT/45-wt%-SGF	209.9	168.3	34.7
cPBT/60-wt%-SGF	209.6	168.9	34.1

According to the results listed in the table, melting point, crystallization temperature, and degree of crystallization hardly change when SGF is added. IM-PEK (polyetherketone), SLS-PEK, and SLS-PEK-20-wt%-GB (glass beads) composite specimens were compared in terms of crystallinity and lamella thickness by Y. Wang et

al. [41], and they reported that the IM specimens have higher crystallinity and lamella thickness than SLS products; however, in the case of SLS products, GB addition has no significant influence, and crystallinity and lamella thickness of PEK products and composite products of PEK and 20-wt% GB are not significantly different. It was reported that particular process parameters (high-temperature holding time, cooling rate, etc.) significantly affect crystallinity, and in a previous study on cPBT [10], SLS specimens had a higher degree of crystallinity than that of IM specimens. Therefore, the result concerning composite GB using PEK reported by Y. Wang et al [41]. and the results concerning a previously reported cPBT [10] and the SGF and cPBT composite used in this study show similar trends. Furthermore, the results presented in the sub-section "Crystallization time" show that crystallization rate (which greatly affects the SLS process) in the powder does not change even if SGF is added, and as shown in the sub-section "Observation of fracture surface," that result is thought to be due to low interaction at the interface between cPBT and SGF.

It was therefore confirmed that while the degree of crystallinity did not increase, neither mechanical properties nor thermal characteristics changed due to the change in morphology of the cPBT.

4.4. Conclusions

In the case that short-glass-fiber (SGF) was added to copolymer PBT (cPBT), adding 0.1-wt% silica drastically improved flowability of the cPBT, and as the proportion of added SGF was increased, flowability was degraded. Moreover, even if SGF was added, crystallization time of the composite powder (which significantly affects selective laser sintering (SLS) processability and accuracy) did not change. In the case that proportion

of SGF addition (15, 30, 45, and 60 wt%) was taken as a parameter, mechanical properties (except tensile elongation at break) were improved; in particular, tensile strength and flexural strength were maximized by 30-wt%-SGF addition (which improves those properties 1.1 times compared to the case of no SGF addition), but impact strength was maximized by 45-wt%-SGF addition (which improves that property 1.8 times compared to the case of no SGF addition). Observations of the fracture surfaces of the SGF SLS specimens showed that as the amount of SGF addition increased, the amount of fiber "debonding" of the SGFs also increased, while the amount of cPBT resin that adhered to the SGFs decreased. This result suggests that the adhesion at the interface between the cPBT and SGF is weak. Moreover, porosity increased as the amount of SGF addition increased; in particular, at 45-wt%-SGF addition and above, it increases dramatically. In addition, average glass fiber length of the SLS specimens was reduced by 5–6 % with SGF addition of 45 wt% and by 10-11 % with SGF addition of 60 wt% , whereas average glass fiber length in the case of the SLS specimens with SGF addition of 30 wt% was not reduced. Furthermore, the micro CT results showed that in the case of SGF addition of 30 wt%, although long fibers remained aligned in the direction of the roller, the SGFs did not align in the direction of the layer thickness. These results show that porosity, adhesion between cPBT and SGF, and fiber length have significant effects on tensile and flexural properties; in contrast, those parameters have little effect on impact strength but a significant effect on stiffness. Compared to the effect of SGF addition on mechanical properties, its effect on thermal properties is more significant; in particular, in the case of SGF addition of 45 wt%, HDT was increased to 172.6 °C (from 69.4 °C) compared to that in the case of no SGF addition. Moreover, the linear-expansion coefficient in the

direction of alignment of the SGF-added SLS specimen was decreased by SGF addition, and the same reduction effect was shown above and below the glass-transition temperature. In addition, crystallization characteristics (i.e., crystallization temperature and degree of crystallization) of an SLS specimen did not change with addition of SGF.

References

[1] A.J. Pinkerton, Lasers in additive manufacturing, Opt. Laser Technol. 78 (2016) 25–32.

[2] R.D. Goodridge, C.J. Tuck, R.J.M. Hague, Laser sintering of polyamides and other polymers, Prog. Mater. Sci. 57 (2012) 229–267.

[3] J. Bai, B. Zhang, J. Song, G. Bi, P. Wang, J. Wei, The effect of processing conditions on the mechanical properties of polyethylene produced by selective laser sintering, Polym. Test. 52 (2016) 89–93.

[4] W. Zhu, C. Yan, Y. Shi, S. Wen, J. Liu, Y. Shi, Investigation into mechanical and microstructural properties of polypropylene manufactured by selective laser sintering in comparison with injection molding counterparts. Mater. Des. 82 (2015) 37-45.

[5] D. Drummer, D. Rietzel, F. Künlein, Development of a characterization approach for the sintering behavior of new thermoplastics for selective laser sintering, Phys. Procedia 5 (2010) 533–542.

[6] L. Verbelen, S. Dadbakhsh, M. Van den Eynde, J.-P. Kruth, B. Goderis, P. Van Puyvelde, Characterization of polyamide powders for determination of laser sintering processability, Eur. Polym. J. 75 (2016) 163–174.

[7] J. Schmidt, M. Sachs, S. Fanselow, M. Zhao, S. Romeis, D. Drummer, K. E. Wirth, W. Peukert, Optimized polybutylene terephthalate powders for selective laser beam melting, Chem. Eng. Sci. 156 (2016) 1-10.

[8] O.R. Ghita, E. James, R. Davies, S. Berretta, B. Singh, S. Flint, K.E. Evans, High temperature laser sintering (HT-LS): an investigation into mechanical properties and shrinkage characteristics of poly(ether ketone) (PEK) structures, Mater. Des. 61 (2014) 124–132.

[9] S. Berretta, O. Ghita, K.E. Evans, Morphology of polymeric powders in Laser Sintering (LS): From Polyamide to new PEEK powders, Eur. Polym. J. 59 (2014) 218-229.

[10] S. Arai, S. Tsunoda , R. Kawamura , K. Kuboyama , T. Ougizawa, Comparison of crystallization characteristics and mechanical properties of poly(butylene terephthalate) processed by laser sintering and injection molding , Mater. Des. 113 (2017) 214–222.

[11] S.Y. Fu, B. Lauke, Y.W. Mai, Science and engineering of short fibre reinforced polymer composites, Woodhead Publishing, Cambridge, 2009.

[12] T. Moriwaki, Mechanical property enhancement of glass fibre-reinforced polyamide composite made by direct injection moulding process, Composites: Part A 2l (1996) 379-384.

[13] B. Mouhmid, A. Imad, N. Benseddiq, S. Benmedakhene, A. Maazouz, A study of the mechanical behaviour of a glass fibre reinforced polyamide 6,6: Experimental investigation, Polym.Test. 25 (2006) 544–552.

[14] J.L. Thomason, Micromechanical parameters from macromechanical measurements on glass-reinforced polybutyleneterepthalate, Composites: Part A 33 (2002) 331-339.

[15] S.Y Fu, B. Lauke, Effects of fiber length and fiber orientation distributions on the tensile strength of short-fiber-reinforced polymers, Compos. Sci. Technol. 56 (1996) 1179–1190.

[16] S.H Jang. Y.H, Kim, S. Lim, G.D. Choi, S.H. Kim, W.N. kim, Effects of fiber characteristics on the mechanical and rheological properties of poly(butylene terephthalate)/glass fiber composites. J. Appl. Polym. Sci. 116 (2010) 3005-3012.

[17] C.P. Fung, J.R. Hwang, C.C. Hsu, The effect of Injection Molding Process Parameters on the Tensile Properties of Short Glass Fiber-Reinforced PBT, Polym. Plast. Tech. Eng. 42 (2003) 45-63.

[18] H. Chung, S. Das, Processing and properties of glass bead particulate-filled functionally graded Nylon-11 composites produced by selective laser sintering. Mater. Sci. Eng., A, 437 (2006) 226–234.

[19] Y. Wang, E. James, O.R. Ghita, Glass bead filled polyetherketone (PEK) composite by High Temperature Laser Sintering (HT-LS), Mater. Des. 83 (2015) 545–551.

[20] T.H.C Childs, A.E. Tontowi, Selective laser sintering of a crystalline and a glass-filled crystalline polymer: experiments and simulations, Proc. Inst. Mech. Engrs. Part B 215 (2001) 1481-1495.

[21] A. Salazar, A. Rico, J. Rodríguez, J. Segurado Escudero, R. Seltzer, F. Martin de la Escalera Cutillas, Fatigue crack growth of SLS polyamide 12: Effect of reinforcement and temperature, Composites: Part B 59 (2014) 285–292.

[22] C. Yan, L. Hao, L. Xu, Y. Shi, Preparation, Characterisation and processing of carbon fibre/polyamide-12 composites for selective laser sintering, Compos. Sci. Technol. 71 (2011) 1834–1841.

[23] A. Jansson, L. Pejryd, Characterisation of carbon-fibre-reinforced polyamide manufactured by selective laser sintering: Addit. Manuf. 9 (2016) 7–13.

[24] Y. Wang, D. Rouholamin, R. Davies, O.R. Ghita, Powder characteristics, microstructure and properties of graphite platelet reinforced Poly Ether Ether Ketone composites in High Temperature Laser Sintering (HT-LS), Mater. Des. 88 (2015) 1310–1320.

[25] A. Mazzoli, G. Moriconi, M.G. Pauri, Characterization of an aluminum-filled polyamide powder for applications in selective laser sintering, Mater. Des. 28 (2007) 993–1000.

[26] K.K.B. Hon, T. J. Gill, Selective Laser Sintering of SiC/Polyamide Composites, CIRP Ann. 52 (2003) 173-176.

[27] H. Zarringhalam, N. Hopkinson, N.F. Kamperman, J.J. de Vlieger, Effects of processing on microstructure and properties of SLS Nylon 12, Mater. Sci. and Eng. A 435–436 (2006) 172–180.

[28] T. Stichel, T. Frick, T. Laumer, F. Tenner, T. Hausotte, M. Merklein, M.Schmidt, A Round Robin study for Selective Laser Sintering of polyamide 12: Microstructural origin of the mechanical properties, Opt. Laser Technol. 89 (2017) 31–40.

[29] M. Chapiro, Current achievements and future outlook for composites in 3D printing,

Reinf. Plast. 60 (2016) 372-375.

[30] S. Ziegelmeier, F. Wöllecke, C. Tuck, R. Goodridge, R. Hague, Characterizing the bulk & flow behaviour of LS polymer powders. Proc. of the Solid Freeform Fabrications Symp., Austin, TX, (2013) 354–367.

[31] R. Chávez-Medellín, LAS. de Almeida Prado, K. Schulte, Polyamide-12/functionalized carbon nanofiber composites: evaluation of thermal and mechanical properties, Macromol. Master. Eng. 295 (2010) 397-405.

[32] F.J. Vallejo, J.I. Eguiazábal, J. Nazábal, Solid state features and mechanical properties of PEI/PBT blends, J. Appl. Polym. Sci. 80 (2001) 885-892.

[33] N. Tomar, S.N. Maiti, Thermal and crystallization properties of PBT/ABAS blends, J. Appl. Polym. Sci. 113 (2009)1657-1663.

[34] K. Senthilkumaran, P.M. Pandey, P.V.M. Rao, Influence of building strategies on the accuracy of parts in selective laser sintering, Mater. Des. 30 (2009) 2946–2954.

[35] C.S. Park, K.J. Lee, J.D. Nam, S.W. Kim, Crystallization kinetics of glass fiber reinforced PBT composites, J. Appl. Polym. Sci. 78 (2000) 576-585.

[36] J.L. Thomason, Structure-property relationships in glass-reinforced polyamide, part 1: the effects of fiber content, Polym. Compos. 27 (2006) 552-562.

[37] J.L. Thomason, M.A. Vlug, Influence of fibre length and concentration on the properties of glass fibre-reinforced polypropylene 4. Impact properties, Composites: Part A 28A (1997) 277-288.

[38] J.P. Kruth, G. Levy, F. Klocke, T.H.C. Childs, Consolidation phenomena in laser and powder-bed based layered manufacturing, CIRP Ann. Manuf. Technol. 56 (2007) 730-759.

[39] S. Ziegelmeier, P. Christou, F. Wöllecke, C. Tuck, R. Goodridge, R. Hague, E. Krampe, E. Wintermantel, An experimental study into the effects of bulk and flow behaviour of laser sintering polymer powders on resulting part properties, J. Mater. Process. Technol. 215 (2015) 239–250.

[40] Z. Shuidong, T. Lingcao, L. Jizhao, H. Hanxiong, J. Guo, Relationship between structure and properties of reprocessed glass fiber reinforced flame retardant poly(butylene terephthalate), Polym. Degrad. Stabil. 105 (2014), 140-149.

[41] Y. Wang, E. James, O.R. Ghita, Glass bead filled Polyetherketone (PEK) composite by High Temperature Laser Sintering (HT-LS) , Mater. Des. 83 (2015) 545–551.

Chapter 5

Effect of anisotropy in the build direction and laser scanning conditions on characterization of short glass fiber reinforced PBT

5-1. Introduction

As one of the most-widespread additive-manufacturing (AM) processes, selective laser sintering (SLS) is a type of powder-bed fusion. In this process, a resin in the form of a bed of powder polymer is partially targeted by a laser, thereby forming a solidified layer of fused powder. In comparison to conventional methods, such as injection molding (IM), SLS has several advantages, namely, increased degree of design freedom, ease of handling complicated shapes and customizations, short fabrication time, and low cost in the case of low production volume [1].

As for standard resins used for SLS, polyamides (polyamides 11 (PA11) and 12 (PA12)) are the most common [2]. As for the PA materials, various properties resulting from addition of glass fiber [3-5] and carbon fiber [6-9] have been extensively studied, but examples other than PA are very few [10, 11]. Therefore, in a previous study [12], we added SGF to cPBT and evaluated various mechanical properties, thermal properties, and shrinkage factor with the amount of SGF as a parameter (15 to 60 wt%). In that study, in particular, the porosity was increased in accordance with the amount of SGF, and that porosity increase was presumed to be the main reason that the molten resin did not easily penetrate between the SGFs [12]. Generally, it is known that even in the case that SGF is not added, porosity is the biggest problem concerning SLS compared with injection molding [2,13,14]. Accordingly, various parameters affecting porosity in SLS have been extensively studied [12,14,15-17]. Furthermore, in regard to SLS, the effects of anisotropy due to the arrangement of test specimens have been reported [18-21]. In particular, it was reported that when the specimens are arranged in the direction of lamination-layer thickness, their mechanical properties tend to be lower than those of specimens arranged on the powder-bed plane. However, few examples of studies using

SLS powder with added fiber to investigate various influences of the specimen arrangement have been reported [8,10].

In the previous study [12], therefore, it was shown that when PBT composite powder with 30-wt%-added SGF was used, the SGFs tended to orientate in the direction of movement of the roller. The influence of orientation on various properties in the case of IM has been studied extensively [22-24]. In particular, to maximize the improvement of properties by fiber reinforcement, it is essential to understand the relationship between anisotropy and differences in characteristics and reflect that knowledge in product design. If that relationship is understood, it is speculated that even in the case of SLS, as with IM, it will lead to expansion of the application of SLS to final products.

Accordingly, in the present study, PBT composite powder with 30-wt% SGF was used, and the effects of laser-irradiation conditions (laser energy density and number of laser scans per layer) and the dependence of the properties (mechanical properties, thermal properties, and shrinkage ratio) of various SLS specimens on the build direction were evaluated, and the evaluated properties were compared with those of IM specimens.

5-2. Experimental methods

5-2.1. Sample preparation

Material

Copolymer PBT (cPBT) powder (powder size (D50) of 78 μm) was formed by cryomilling (as described in previous studies [12,14]). In the case of SLS, generally, lamination layers with thickness of 0.1–0.15 mm are repeatedly formed [17,25]; consequently, laying them uniformly is presumed to be difficult if continuous fibers or

long fibers are added [26]. In this study, 30-wt% short glass fiber (SGF, SS05C-404, Nitto Boseki Co., Ltd.) was added to the cPBT resin powder (as described in a previous study [12]). The SGF (with average fiber length of 99 μm, fiber diameter of 11 μm, and density of 2.6 g/cm^3) was treated with a silane coupling agent, and 0.1-wt% hydrophobic silica (AEROSIL®RA200H, Evonik Industries) was added to the mixed powder to improve its flowability. The cPBT powder, SGF, and silica were blended for 15 minutes by mixer (SKH-40CA, Misugi, Co., Ltd.). Scanning electron microscopy (SEM) images of the (a) cPBT powder [14], (b) SGFs, and (c) cPBT/30-wt%-SGF [12]

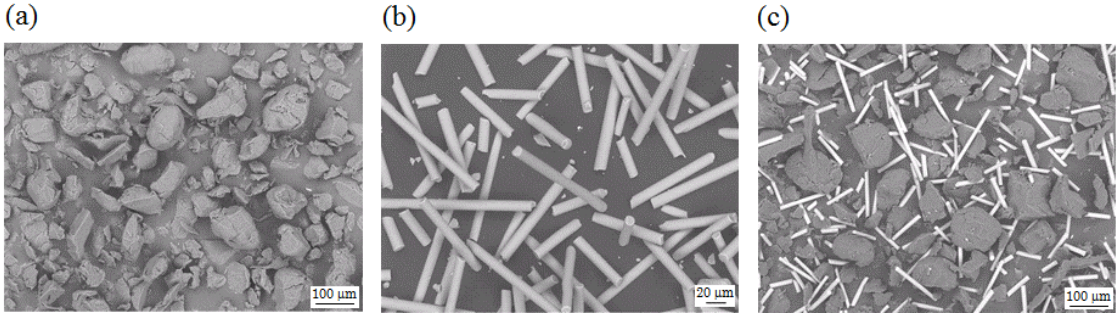

Fig. 1: SEM images of (a) cPBT-powder (b) SGFs, and (c) cPBT/30-wt%-SGF composite powder.

Selective laser sintering (SLS)

An SLS machine (RaFaEl 300, Aspect Inc.) was used for manufacturing the specimens. As the heat source, a carbon-dioxide laser (with wavelength of 10.6 μm and spot diameter of about 0.3 mm) was used. As for SLS, the parameters [2] that influence the quality of the sintered specimens are laser power, scan rate, scan spacing, powder-bed temperature, feed temperature, and layer thickness. In this study, laser power and number of laser scans per layer ("single scan" and "double scan," hereafter) were used as parameters.

Schematic diagrams explaining the “single scan” and “double scan” laser-scanning methods are shown in Fig. 2.

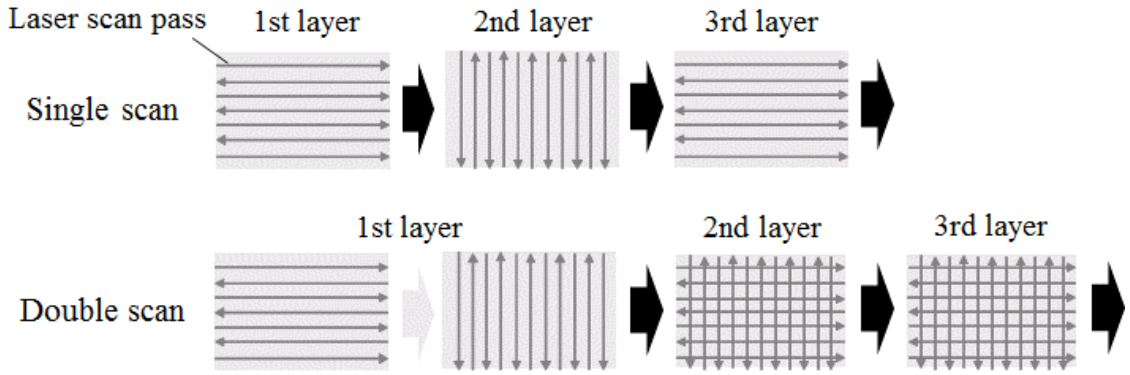

Fig. 2: Schematic of single laser scan and double laser scan.

Up until now, in our previous study on cPBT [14], the single-scan laser-scanning method was investigated. That is, as for the first layer, the laser is scanned in one direction on the powder-bed surface. After that, as for the second layer, the laser is scanned perpendicularly to the direction of the first-layer scan, and as for the third layer, the laser is scanned in the same direction as the first-layer scan. This single-scan laser scanning is then repeated for the remaining layers. In contrast, in the present study, the double-scan laser scanning method was investigated. That is, as for the first layer, the laser is first scanned in one plane on the powder-bed surface. After that, the laser is scanned again on the same layer but in the perpendicular plane to the first scan, before the next powder layer is laid to complete the laser scanning of the first layer. And the effect of repeating this double scan for the remaining layers was investigated. According to reports by Goodridge et al. [27] and Khalil et al. [28], in the case of the double-scan method, laser energy can be gradually imparted to each layer; consequently, this method is effective for materials, such as PE (polyethylene), with a narrow

processing window. Also according to those reports, shrinkage and warp can be reduced by using the double-scan method. For the single-scan procedure, laser power was set to 5, 8, 11, 14, 17, 20, 25, and 30 W; for the double-scan procedure, it was set to 5, 8, 11, 14, 17, and 20 W. The conditions under which the specimens were formed are listed in Table 1.

Table 1: Processing parameters for SLS.

Processing parameters	
Wavelength	10.6 μm
Laser-beam diameter	0.3 mm
Fill and outline laser power	5 - 30 W (single scan) 5 - 20 W (double scan)
Scan speed	5.0 m/s
Scan spacing	0.15 mm
Fill energy density	6.7 - 40.0 kJ/m^2 (single scan) 13.4 - 53.4 kJ/m^2 (double scan)
Laser-scan direction	Alternating bi-directional scan
Powder-bed temp.	190 °C
Feed temp.	165 °C
Layer thickness	0.1 mm
Part piston temp.	180 °C

Laser energy density per layer of the double-scan laser scanning was assumed to be the sum of that of two single scans. All parameters other than laser power are the same as those used in a previous study on cPBT [14] and cPBT/SGF composite [12]. In this study, the anisotropy of the build direction was investigated. The build direction is defined in Fig. 3 by using a tensile specimen as an example. As for the build direction, the X-direction is defined as the "roller-movement direction," the Y-direction is defined as the direction perpendicular to the "roller-movement direction on powder-bed plane," and the Z-direction is defined as the "layer-thickness direction."

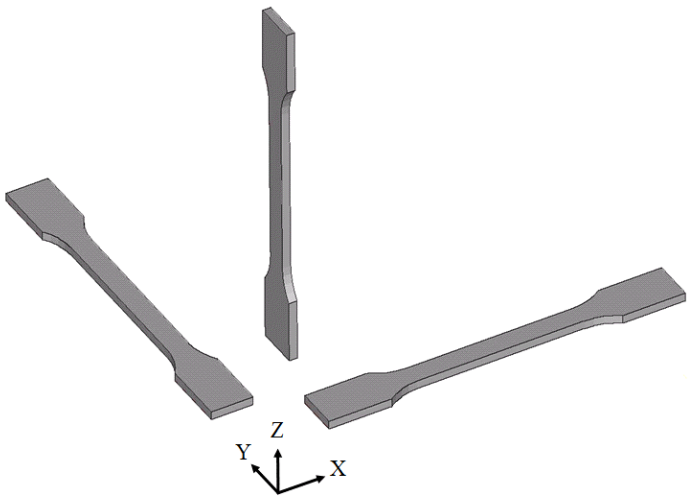

Fig. 3: Schematic of build direction of the tensile specimens.

Injection molding (IM)

IM specimens were prepared by using IM cPBT pellets (dried for 4 hours at 140 °C before IM) and an IM machine (S-2000i 50A, Fanuc Corporation). The dimensions of the test specimens formed by IM were assumed to be the same as those formed by SLS. As for the IM conditions, nozzle temperature was 245 °C, cylinder temperature was 230-250 °C, injection pressure was 50 MPa, holding pressure was 40 MPa, tool temperature was 72 °C, injection speed was 20 mm/s, and screw revolution rate was 120 rpm. As for the IM specimens, if a tensile specimen is taken as an example, the longitudinal direction is defined as the X-direction (i.e., "machine direction" (MD)), the Y-direction is defined as the "transverse direction" (TD), and the Z-direction is defined as the "nominal direction" (ND).

5-2-2. Evaluation methods

Mechanical testing

To evaluate mechanical properties of the SLS and IM specimens (composed of cPBT with 30-wt% added SGFs) oriented in each direction (X, Y, and Z), tensile tests, flexural tests, and Charpy-impact-strength tests were conducted. The tensile-test specimens were taken as "type A" specified in ISO3167; 1993 [total length: 170 mm; parallel-portion length: 80 mm; and thickness: 4 mm]. Tensile tests were performed on a 5500RF tensile tester, Instron Corporation, according to ISO527-1 and -2; 2012. Testing speed was 50 mm/min, and distance between the clamps was 115 mm. Flexural tests were performed on the same tensile tester according to ISO178; 2001. Size of the flexural-test specimens was 80 × 10 × 4 mm, testing speed was 2 mm/min, and distance between the fulcrums was 64 mm. Charpy-impact-strength tests were performed on an AG-100kNX testing machine, Shimadzu Corporation, in accordance with ISO179–1; 2010. A notch was formed in the Charpy-impact-strength-test specimens (with the same shape as the flexural-test specimens). Generating an energy of 0.5 J, the hammer weight was applied so that the impact was in the edgewise direction. All the strength tests were performed with n = 5 (minimum), and average strength and elongation at break were estimated.

Optical microscopy

To evaluate the porosity of the SLS and IM specimens, the central portions (10 × 4 mm) of the specimens were cut out, and the cut-out portions were embedded in epoxy resin. The epoxy-embedded portions were then polished at intervals of 0.5 mm and observed by microscope (VHX-2000, Keyence Corporation). After that, porosity of the portions was calculated by image processing with image-analysis software (WinROOF,

Mitani Corporation). For measuring porosity, cross sections of the portions at n = 5 or more were observed by optical microscope.

To compare the lengths of SGFs in the SLS and IM specimens, first, portions (weighing 8 to 10 g) of the flexural-strength SLS and IM specimens were cut out and heated at 700°C for 1.5 h to burn off the cPBT only. The lengths of the residual SGFs (at least 800) were measured by optical microscope (VHX-5000, Keyence Corporation). Moreover, polarization microscopy (model BX60, Olympus Corporation) was used to compare the morphologies of the single-scan- and double-scan-formed SLS specimens with that of the IM specimens. The middle part (40 × 10 × 4 mm) of the flexural specimens (80 × 10 × 4 mm) was cut out, and the cut-out portion was cut to a thickness of 2 μm with a microtome. The thin pieces were then observed by polarization microscopy.

Scanning electron microscopy (SEM)

After the tensile tests, the fracture surfaces of the IM specimens and SLS specimens composed of cPBT with 30-wt% added SGF and formed in each build direction were observed by SEM (JSM-7000F, JEOL, Ltd.) with acceleration voltage taken as 15 kV.

Micro-computer tomography (micro-CT)

Orientation of the SGFs in the SLS- and IM specimens was determined by micro-CT measurement with an inspeXio SMX-100CT (manufactured by Shimadzu Corporation). The center of a flexural test piece formed from the SLS specimens arranged in the X-direction (as shown in Fig. 3) was cut in the thickness direction, and an area of 2 × 2 mm in the X-Y plane in the center portion in the thickness direction and areas of 2 × 1.8 mm in the Y-Z and the Z-X planes were measured by micro-CT. As for the IM specimens, it is clear that the orientation of the SGFs differs in the ND [29]. Therefore,

as for the IM specimens, an area including the surface (skin layer) was measured instead of only the central portion (core portion). As for the measurement conditions, X-ray tube voltage and current were respectively 60 kV and 60 μA, and voxel size was 4 μm. The fiber-extraction angle of each SGF was calculated by using a fiber-extraction algorithm/tool [30] based on cylindrical fitting of SGF images obtained by micro-CT, and the orientation tensor of each fiber was estimated. The angle of a SGF is defined in Fig. 4, and the orientation tensor was calculated by using Equations (1) to (3) [29] shown as follows.

$$a_{11} = \frac{1}{N}\sum_{i=1}^{N}(sin\theta cos\varphi)^2 \tag{1}$$

$$a_{22} = \frac{1}{N}\sum_{i=1}^{N}(sin\theta sin\varphi)^2 \tag{2}$$

$$a_{33} = \frac{1}{N}\sum_{i=1}^{N}(cos\theta)^2 \tag{3}$$

Here, a_{11}, a_{22}, and a_{33} are respectively the orientation tensors in the X-, Y-, and Z-directions, and N is the number of SGFs.

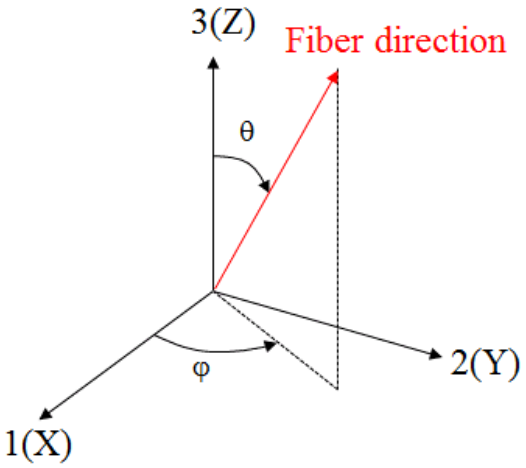

Fig. 4: Definition of fiber orientation.

Differential-scanning calorimetry (DSC)

Melting point, crystallization temperature, and degree of crystallinity of the SLS and IM specimens formed with cPBT/30-wt% SGF were determined by differential-scanning calorimetry (DSC) (Q2000, TA Instruments). Degree of crystallinity (χ) is given in terms of heat of fusion (ΔH), perfect-crystal heat of fusion (ΔH_m^o), and mass fraction of fiber (f) as [31]

$$\chi(\%) = \frac{\Delta H}{\Delta H_m^o \times (1 - f)} \times 100 \quad (4)$$

In this study, ΔH_m^o was taken as 145.5 J/g [32, 33]. The DSC specimens (with assumed weight of 5 $\pm$ 0.5 mg) were cut from the central portion of the flexural test pieces and measured under increasing temperature from 5 to 300 °C at a rate of 10 °C/min and nitrogen flow rate of 40 mL/min.

Heat-deflection temperature (HDT) testing

Heat-deflection temperature (HDT) of the SLS and IM specimens formed with cPBT/30-wt% SGF was measured by HDT tester (6A-2, Taiyo-seiki Co., Ltd.) according to standard ISO75-1,-2; 2004 (JIS K7191-1,-2; 2007) in flatwise mode under bending stress of 1.82 MPa.

Thermomechanical analysis (TMA)

The cPBT/30-wt%-SGF SLS specimens formed in the X-, Y-, and Z- directions (sample size: 10×5×5 mm) were measured by thermomechanical analysis (TMA) (TMA4000SA, BrukerAXS, Ltd.) according to standard ISO11359-2. A compressive load of 26 mN (face pressure: 4$\pm$0.1 kPa) was applied by a probe positioned about 3

mm from the surface of the specimen (size of 10 × 5 mm). As for the measurement environment, nitrogen gas was flowed at a rate of 100 ml/min, test temperature range was 25 to 200 °C, and rate of temperature increase was 5 °C/min. Before the TMA measurements, the specimens were not annealed. The linear-expansion coefficient, at a temperature not in the range near the glass-transition temperature (Tg), was calculated. Coefficients of linear expansion at temperatures under Tg ($\alpha 1$) and above Tg ($\alpha 2$) were calculated in temperature ranges of 25-40 °C and 70-200 °C, respectively.

Shrinkage measurements

In a CAD model, the size of the samples was 200 × 10 × 10 mm, the 200-mm edge was aligned in the X-, Y-, and Z-directions, and shrinkage ratio (S) in each build direction (X, Y, and Z) was evaluated from the following equation [34]:

$$S = \frac{L1 - L2}{L1} \times 100 \tag{5}$$

where *L1* is the CAD value of length, and *L2* is the measured length. S was measured in the X- and Y-direction by using Vernier calipers. However, in the Z-direction, an excessive amount of laser penetration occurs in the depth direction [34]. For that reason, it was predicted that the amounts of surplus sintering due to the laser in the Z direction differ in the cases of the single and double scans. Accordingly, a test piece with dimensions of 10 × 10 × 0.4 mm (thickness direction = Z-direction), which is expected to be undamaged during blasting and include the influence of shrinkage rate within the measurement error, was used, and thickness *L3* was measured, and the value obtained by subtracting *L3* from *L2* was used to estimate S in the Z-direction.

5-3. Results and discussion

5-3-1. Mechanical properties

Mechanical properties, namely, (a) tensile strength, (b) elongation at break, and (c) flexural strength, and (d) notched Charpy impact strength, of the single- and double-scan specimens formed in the X-, Y-, and Z-build directions are plotted against laser energy density in Fig. 5. The numerical values when mechanical properties in each direction are maximized and the laser energy densities at that time are listed in Table 2.

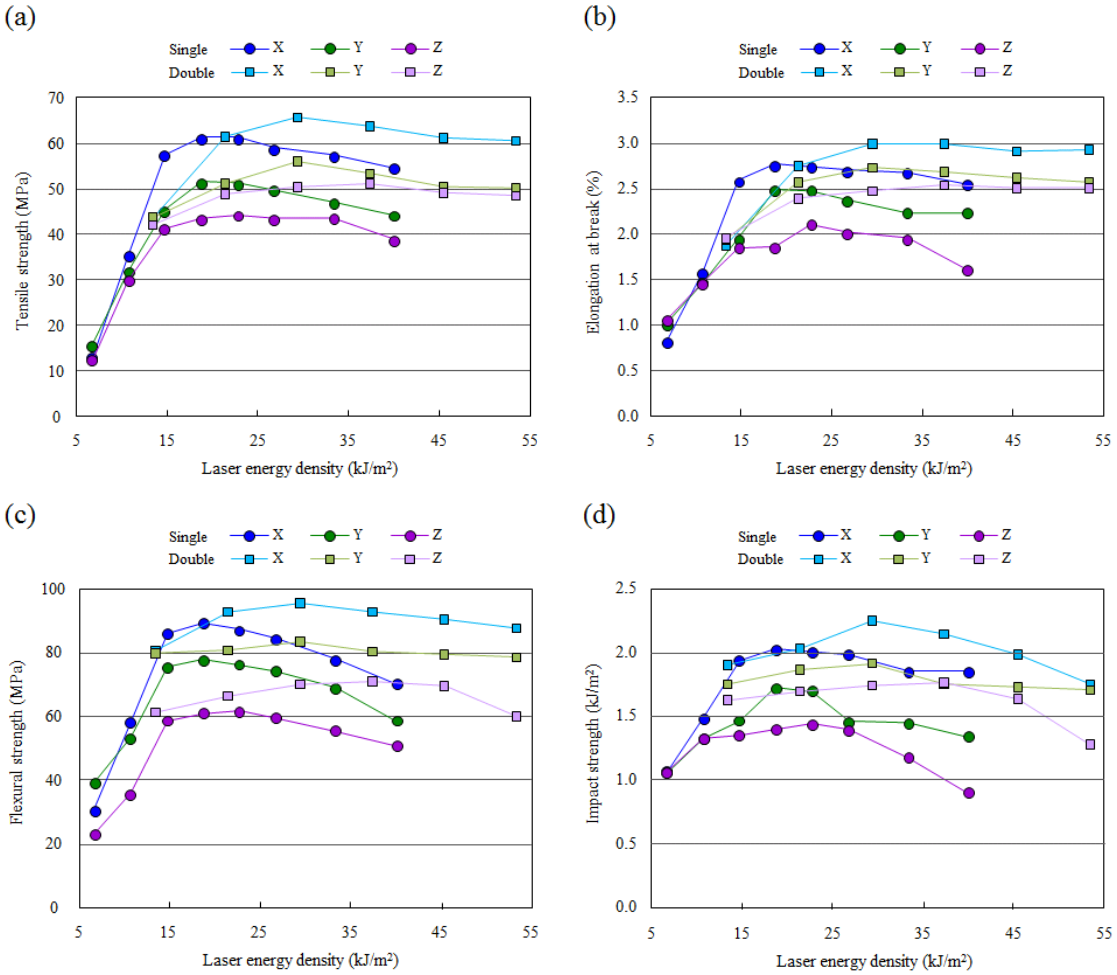

Fig. 5: Comparison of mechanical properties of SLS specimens formed by single-scan and double-scan laser-scanning method in the X-, Y-, and Z-build directions under various laser-energy densities: (a) tensile strength, (b) elongation at break, (c) flexural strength, and (d) notched Charpy impact strength.

Table 2: Comparison of mechanical properties of IM specimens and SLS specimens formed in the X-, Y-, and Z-build directions under optimum laser conditions for single-scan and double-scan laser scanning.

Molding method	Build direction	Scan method	Laser energy density (kJ/m^2)	Tensile strength (MPa)	Elongation at break (%)	Flexural strength (MPa)	Impact strength (kJ/m^2)
IM	-	-	-	66.1	3.07	97.8	3.02
SLS	X	Single	18.7	61.2	2.77	89.4	2.03
	Y	Single	18.7	51.4	2.49	78.0	1.73
	Z	Single	22.7	44.1	2.11	61.9	1.44
	X	Double	29.4	65.7	3.00	95.9	2.25
	Y	Double	29.4	56.0	2.73	83.7	1.92
	Z	Double	37.4	51.1	2.54	71.4	1.77

It is clear from these results that compared to the single-scan case, the double-scan laser-scanning procedure improves the mechanical properties (tensile strength, elongation at break, flexural strength, and notched Charpy impact strength) in any of the directions. Laser-energy densities of maximum mechanical properties are compared. It is clear that in both the single- and double-scan cases, as for difference in build directions, the mechanical properties in the case of the X- and Y-build directions are maximized at the same laser energy density; on the other hand, compared the case of the X- and Y-build directions, in the case of the Z-build direction, they are maximized at higher laser energy density.

Up to now, it has been shown that in the single-scan case with cPBT, mechanical performance deteriorates due to thermal degradation of cPBT (that is, reduction of molecular weight) when laser energy density is increased beyond 18.7 kJ/m^2 [14]. However, in the case of SGF30-wt% SLS specimens, it was reported that porosity and adhesion between SGFs and cPBT have significant influences and that mechanical properties showed maximum values when the single-scan laser scanning was applied (at

laser energy density of 18.7 kJ/m^2) with the build direction in the X-direction; that is, the cPBT resin itself may be deteriorated to some extent during laser scanning [12].

In the present study, it was revealed that when double scanning was used, as compared with the single-scan case, mechanical properties were maximized at higher laser energy density (that is, in the single-scan case, the value at which thermal degradation obviously occured), and it was also revealed that high strength was achieved while deterioration of the resin was suppressed by scanning twice with low energy density per layer. In addition, as reported by Bai et al. [35], although flexural modulus was also improved after the double-scan scanning, the same laser power as the single-scan method was used. From the results of this study, it is clear that the mechanical properties can be maximized by using the double-scan method with lower laser power (i.e., laser energy density) than that used with the single-scan method.

Comparing the dependences of maximum strength on built direction reveals that mechanical properties can be ranked in the descending order of build direction of X > Y > Z in both the single-scan and double-scan cases. It is known from several reports that normally in the case that the specimens are formed in the X- and Z-build directions, the strength in the latter case often decreases, and that result was confirmed in the present study. However, as for comparing the dependencies of the tensile strength on the X- and Z-build directions in the case that only cPBT was used, in the case of the X-direction and laser energy density of 14.7 kJ/m^2, the tensile strength was 54.9 MPa [14], however in the case of the Z-direction and laser energy density of 22.7 kJ/m^2, the tensile strength was 48.1 MPa. In other words, the tensile strength was lowered by about 12.4 %. On the other hand, it was revealed by the results of the present study (in which SGF was added to the cPBT) that in the case of the Z-direction in comparison to the X-direction, tensile

strength was about 27.9 % lower. And compared to the specimens formed without addition of SGF, those with added SGFs showed a remarkable anisotropy in build direction. Moreover, Jansson et al. [8] used a composite product formed with PA12 and carbon fibers (CF) to compare the influence on strength of the X- and Y-build directions, and they found that of the strength in the Y-direction is lower. The results reported in this paper show the same trend. It was therefore revealed that when SGF was added, in comparison with the case that SGF was not added, the influence of the dependence of mechanical properties on build direct was prominent.

Furthermore, when the influences of the single- and double-scan scanning methods were compared in terms of build direction, it became clear that the increase effect on the mechanical properties due to the double scan was 7 to 11 % in the case of the specimens in the X- and Y-build directions; in contrast, in the case of the Z-build direction, it was 15 to 23%. This result is presumed to be due to the fact that the effect of suppressing deterioration of the resin is higher in the double-scan case. And when the IM specimens are compared with the SLS specimens, it becomes clear that all the mechanical properties are lower in the SLS case. This result is similar to the results of studies on IM and SLS specimens formed with cPBT [14], PA12 [13, 36], and PEK [20]. However, in a similar manner to IM specimens, the various mechanical properties of SLS specimens with added SGFs are conceivably influenced in a complex way by properties other than porosity, such as adhesion of SGF and PBT, anisotropy of SGFs, and breakage of SGFs. In the next and following sections, these influences are compared with the results for IM specimens. In addition, the results of a study on SLS specimens presented hereafter are compared using specimens formed made under the condition that the mechanical properties are maximized.

5-3-2. Porosity and observation of fracture surface

Cross-sectional observations of SLS specimens formed in the X-build direction with the single- and double-scan laser-scanning methods are shown in Fig. 6. The results of the porosity evaluation of SLS specimens formed in the X-, Y, and Z-build directions with the single- and double-scan methods are plotted in comparison with the IM specimens in Fig. 7.

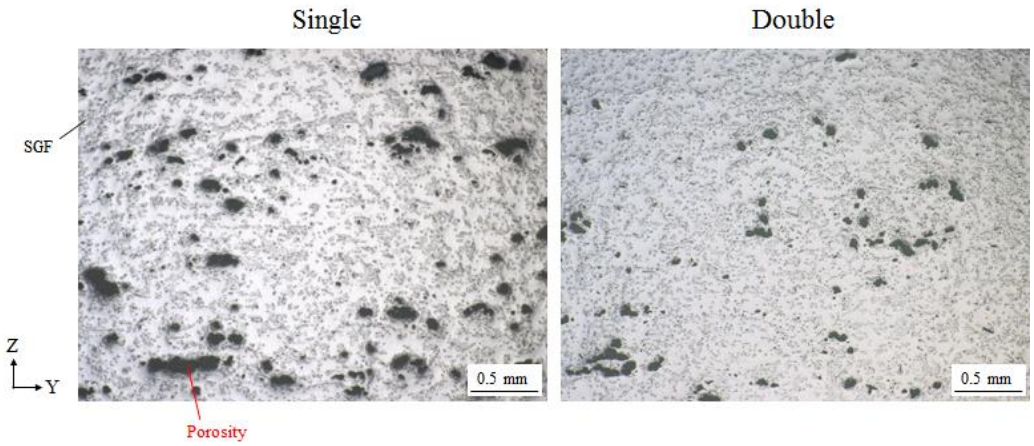

Fig. 6: Cross-sectional observation (optical microscope) images of SLS specimens formed in the X-build direction in the case of the single- and double-scan methods.

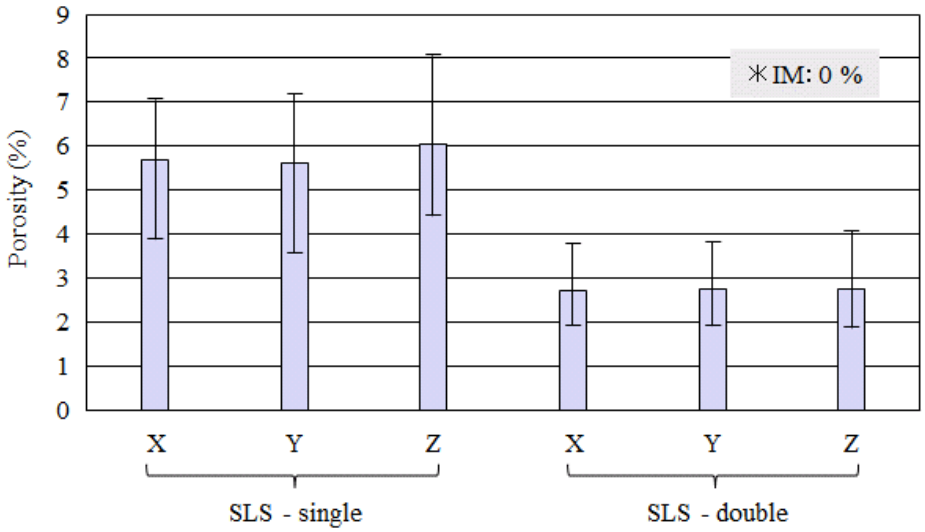

Fig. 7: Comparison of porosities of IM specimens and SLS specimens formed by the single- and double-scan scanning methods in the X-, Y-, and Z-build directions.

As for the IM specimens in this study, no porosity was observed in the same manner as previously reported results on IM specimens formed with cPBT [14]. When the amounts of porosity in the single-scan-formed specimens were compared, dependencies in the X- and Y-build directions were revealed. This result is presumed to be due to the fact that the laser is scanned alternately in the X- and Y-directions, respectively. It also agrees with the result reported by Jansson, et al. [8]. On the other hand, it confirms that the porosity in the Z-direction is slightly increased compared with that in the X- and Y-directions. In a previous study on cPBT [14], it was shown that as laser energy increases, porosity itself increases slightly due to the influence of gas in addition to a decrease in molecular weight due to thermal decomposition. In the present study, since the laser energy density in the Z-direction of the sample is higher than that in the X- and Y-directions, it is conceivable that it has a greater influence on porosity. Moreover, when the double-scan specimens are compared to the single-scam specimens, porosity decreases by more than half, and its size is decreased, with no significant difference seen between the X-, Y-, and Z-directions.

Dadbakhsh et al. [37] compared the single- and double-scan methods in terms of porosity from the top surface in a single layer by using virgin, mixed, and aged PA 12. In the case of the single scan, porosity was 0.2 to 2 %; in contrast, it has been reported that porosity is hardly seen after the double scan. The above results (observed in the cross section) revealed that the double-scan scanning method is not only effective for reducing in-plane porosity but also especially effective for reducing porosity in the thickness direction. It was thus confirmed that with the double-scan process, it is possible to easily impregnate the molten resin between the SGFs while suppressing

deterioration due to excessive laser irradiation; as a result, porosity can be considerably reduced.

SEM images of fracture surfaces of SLS specimens formed in the X-, Y-, and Z-build directions by the single- and double scan scanning methods are shown in Fig. 8.

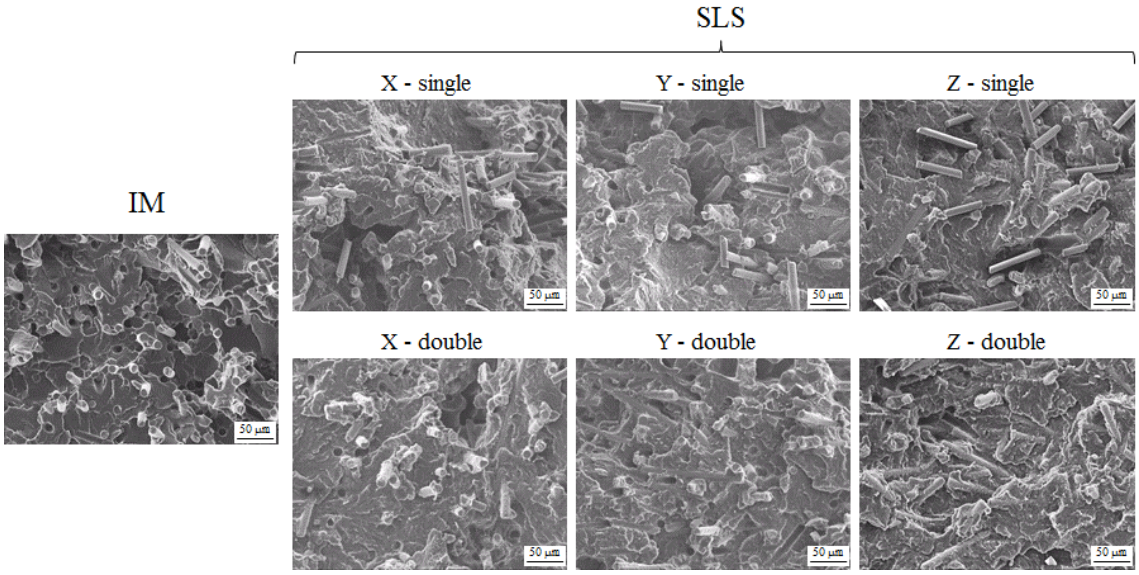

Fig. 8: SEM images of fracture surfaces of IM specimens and SLS specimens with single scan and double scan and arranged in the X- or Y- or Z-direction.

As for the IM specimens, many traces of missing fibers can be seen, and it is clear that adhesion between SGFs and cPBT is relatively poor. When the SLS specimens are compared, the single-scan specimens, as for the fracture surface in the case the specimens were formed by the single-scan method in either of the X-, Y-, or Z-build directions, areas containing SGFs existing alone can be seen; in contrast, the double-scan specimens do not show SGFs existing alone. As for the IM specimens, it is suggested that adhesion between SGFs and cPBT is poor. Given that result, it is assumed that as for the double-scan specimens, rather than improving the adhesion, the

reduction of porosity (namely, the fact that the resin sufficiently fills up the peripheries of the SGFs) has a greater influence.

5-3-3. Fiber orientation and distribution

Micro CT results for IM specimens and SLS specimens[12] formed in the X-build direction with SGFs are shown in Fig. 9. Fiber anisotropy extracted by image analysis is shown in Fig. 10. The results of estimating the tensor of SGFs in each direction are listed in Table 3.

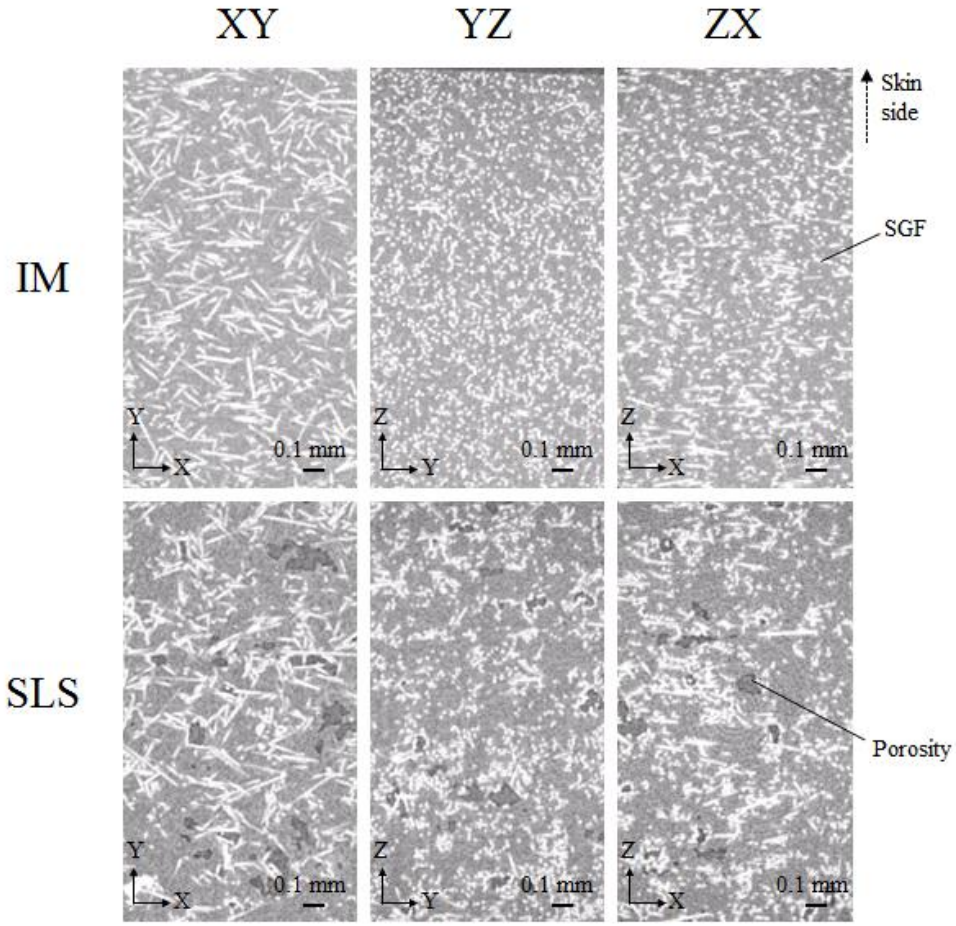

Fig. 9: Comparison by micro-CT images of IM and SGF specimens in X-Y plane, Y-Z plane, and Z-X plane.

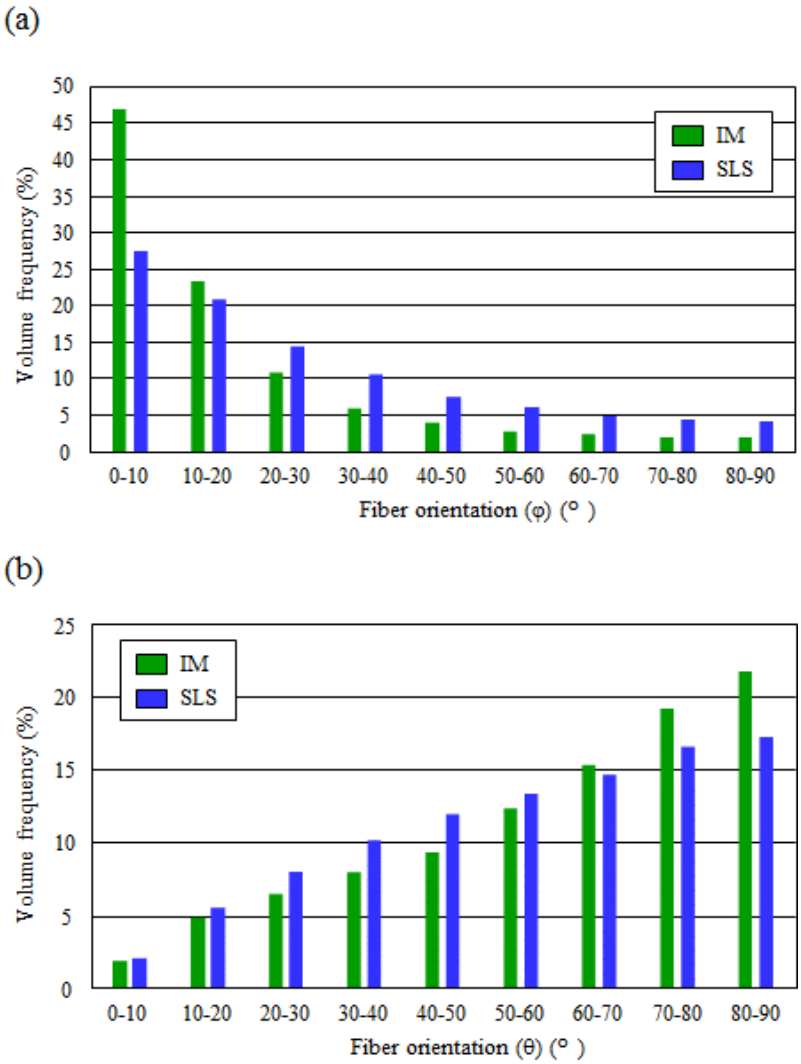

Fig. 10: SGF direction of IM and SLS specimens: (a) angle θ , and (b) angle φ .

Table 3: Results concerning fiber-orientation tensors of IM and SLS specimens.

Molding method	Fiber orientation tensors		
	α_{11}(X)	α_{22}(Y)	α_{33}(Z)
IM	0.62	0.30	0.07
SLS	0.50	0.35	0.15

As for the micro-CT results, in the case of the IM specimens, the fibers are aligned in the X-direction (i.e., MD), and the phenomenon in which the fibers align in the Y-direction of the core layers (which has often been reported [29]) was not observed. As for the cPBT used in the present study, crystallization rate for SLS is low, and since it is not intended for IM use, the influence of cooling due to the mold might be a minor factor that influences the normal injection grade.

As for the SLS specimens, the fibers are aligned in the X-direction (the direction in which the powder is laid by the rollers), indicating that relatively long fibers remain in the X-direction. Moreover, it is clear from the CT results as well that in the case of the IM specimens, in the same manner shown in the cross-sectional observations shown in subsection 5-4-2, the SGFs are well dispersed, porosity is not observed; in contrast, in the case of the SLS specimens, the SGFs are poorly dispersed, and porosity is observed. In the case of the IM specimens and SLS specimens, when anisotropy of extracted fibers and orientation tensors are compared, it becomes clear that in contrast to the alignment of fibers in the X-direction (i.e., MD) of the IM specimens, in the case of the SLS specimens, the ratio of fibers aligned in the X-direction (i.e., that in which powder is laid by the roller) is small, and the ratio of fibers aligned in the Z-direction is large. Moreover, it is understood from the results concerning orientation tensors that the difference in mechanical properties in the X- and Z-directions described in subsection 5-4-4 is a phenomenon resembling two concerning IM, namely, dependency on alignment of SGFs and mechanical properties of weld-line parts [38].

The distributions of SGFs in the IM and SLS specimens [12] are shown in Fig. 11. Although it is known that average fiber length of GF decreases in IM specimens due to the kneading process and interference of the glass fibers during the IM process [39],

even in the case of IM specimens formed using SGF in the present study, average fiber length of SGFs was shortened by about 10 %. Moreover, as for the SLS specimens, difference in average fiber length due to the SLS process was not seen; however, when fibers with length of more than 200 μm are compared, it becomes clear that the amount of such SGFs in the SLS specimens is lower than that before SLS processing, and it is supposed that the long fibers are broken during the SLS processing [12]. That is to say, in the case of SLS, although the effects of alignment and definite breakage of SGFs do not occur to the same extent as in the case of IM processing, it is clear that the SGFs are aligned by the roller laying and only long fibers (which make up with a very small proportion of SGFs) are broken.

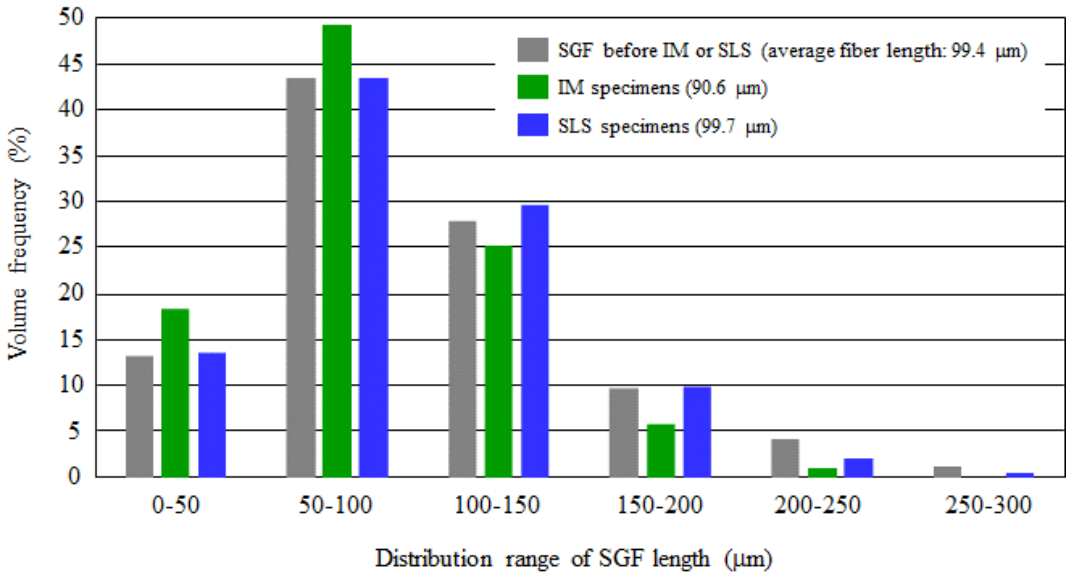

Fig. 11: Distribution of SGFs in IM and SLS specimens [12].

5-3-4. Crystallization characteristics and morphology

In the case of the double-scan method used in the present study, since the laser is irradiated twice per layer, the time that the sintered specimens are retained in the powder at high temperature is long. For example, in the case of the flexural specimen,

the retention time during which the sintered part remains in the powder is 1.5 times that in the case of the single scan. Although this trend also depends on the sintered shape, in the case of the Z-build direction, the retention time is longer than that in the cases of the X- and Y-build directions. Accordingly, melting point, crystallization temperature, and degree of crystallinity of the single-scan-formed specimens and double-scan-formed specimens by SLS were compared with the respective properties of the IM specimens. The results of the comparison are listed in Table 4.

Table 4: Results of evaluation of Tm, Tc, and degree of crystallinity of IM and SLS specimens formed by single-scan and double-scan methods and arranged in the X- or Z-build directions.

Molding method	Build direction	Scan method	Tm (°C)	Tc (°C)	Degree of crystallinity (%)
IM	-	-	207.8	173.9	29.4
SLS	X	Single	209.5	169.5	35.0
	Z	Single	209.8	169.7	42.6
	X	Double	210.1	169.8	37.1
	Z	Double	210.3	169.7	44.0

As for the IM specimen, Tc is 6.3 °C higher than reported Tc of a cPBT IM specimen (167.6 °C [14]) because the SGFs act as a nucleating agent as the resin flows. In the case of the SLS specimens, SGFs do not act as nucleating agents even if they are added, so Tc does not change significantly [12]. Also, when melting points and degrees of crystallinity are respectively compared, it becomes clear that the SLS specimens have higher values than those of the IM specimen. This result is similar to results reported in regard to cPBT [14], PA12 [35], PEK-glass-beads composite [40], and these properties have a significant influence on the difference in the IM and SLS processes [14, 40]. In

other words, it is supposed that the IM specimen is formed by rapid cooling using a mold; in contrast, the SLS specimen is formed by holding the sintered part at high temperature (near the melting point) and then slowly cooling it.

In comparison to the difference in the degrees of crystallinity of the SLS specimens formed in the X- and Z-build directions, the degree of crystallinity increases when either the single-scan or double-scan methods are applied in the case of the specimen formed in the Z-build direction. According to Ghita et al. [20], who compared the degrees of crystallinity in the vicinity of the bottom surface and the vicinity of the top surface in the case of specimens arranged in the Z-build direction and using PEK, the retention time concerning the vicinity of the bottom surface at high temperature is longer, so the degree of crystallinity increases there. Although the central part of the test piece was used for measuring the degree of crystallinity when it was formed in the Z-build direction in this study, it is thought that the degree of crystallinity is higher when the specimen is formed in the Z-build direction than when it is formed in the X-build direction because the retention time at high temperature is longer. It is therefore presumed that in the case of forming the specimen in the Z-build direction, the distribution of crystallinity is remarkably higher as compared with the case where it is formed in the X-build direction.

Moreover, comparing the single- and double-scan-formed specimens reveals that the former specimen has a slightly higher melting point. In the case of a crystalline resin, it is known that as isothermal crystallization temperature after melting rises, lamella thickness increases, and melting point rises [41]. In this study, the melting temperature in the case of the double-scan specimen is kept at a higher point than that in the case of the single-scan one, and since the temperature rises in the layer beneath that under laser

irradiation (that is, surplus sintering), it is possible that the longer holding temperature near the melting point has an effect on the crystallinity. Regarding the degree of crystallinity, it seems that the double-scan method produces a higher value because of the longer retention time at high temperature than in the case of the single-scan method.

Next, the results of spherulite observation of the IM specimens and the SLS single- and double-scan-formed specimens are shown in Fig. 12.

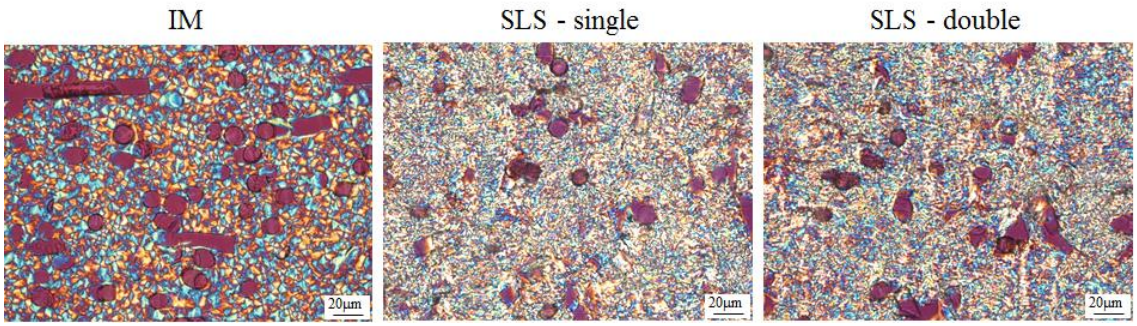

Fig. 12: Polarization-microscopy images of IM specimens and SLS specimens formed by single-and double-scan methods.

As for the IM specimen, clear Maltese crosses are observed, whereas in the SLS specimens, non-uniform spherulites are observed. Moreover, in the case of the SLS specimens, the spherulites are smaller. It was reported by Zarringhalam et al. [25] that in the case of PA12, compared to that of SLS-formed specimens, the size of spherulites was smaller in the case of IM specimens. This finding is attributed to the influence of rapid cooling in the IM process, which has no influence in the case of the SLS process. In the present study, even if the rise in crystallization temperature in the case of IM is considered, it was confirmed that the SGFs themselves function as nucleating agents; that is, it is conceivable that the SGFs have the effect of reducing the size of spherulites. However, compared to the IM specimens, the SLS-formed ones have smaller spherulite size, namely, the opposite trend. This contradictory trend is presumed to be due to the

significant influence of contamination, such as iron, which contaminates the cPBT during pulverization (as reported in a previous cPBT study [14]) and acts as a nucleating agent. Moreover, comparing the single- and double-scan cases regarding SLS reveals no remarkable difference in the spherulite states in the two cases. It is considered that this result is due to the considerable nucleating-agent effect of contamination.

In the case of the IM specimens made of crystalline resin, it has been reported that impact strength increases as spherulite size decreases [42]. However, as shown in subsection 5-4-1, impact strength increases in the order of IM specimen, double-scan SLS specimen, and single-scan SLS specimen, and it has no correlation with spherulite size. Therefore, it can be inferred from this comparative result concerning spherulite size that in the case of SLS, porosity affects mechanical properties (especially impact strength).

5-3-5. Thermal properties

Heat-deflection temperatures (HDT) of IM and SLS specimens formed with single-scan and double-scan methods and arranged in the X-, Y- and Z-build directions are compared in Fig. 13. Comparing the SLS specimens reveals that in the same manner as concerning mechanical properties, clear dependence on build direction. It is generally known that HDT greatly influences crystallinity in the case of IM specimens [43]. The same trend holds for IM and SLS specimens formed with cPBT, and when HDT and crystallinity of IM formed with cPBT are compared with the respective values for SLS specimens formed in the X-build direction, it becomes clear that those reported values for IM specimens (49.2 °C and 26.9 % [14]) differ from those for SLS specimens

(69.1 °C and 34.9 % [12]). As for SLS specimens, it is presumed that in contrast to IM specimens, although porosity remains, its influence is small.

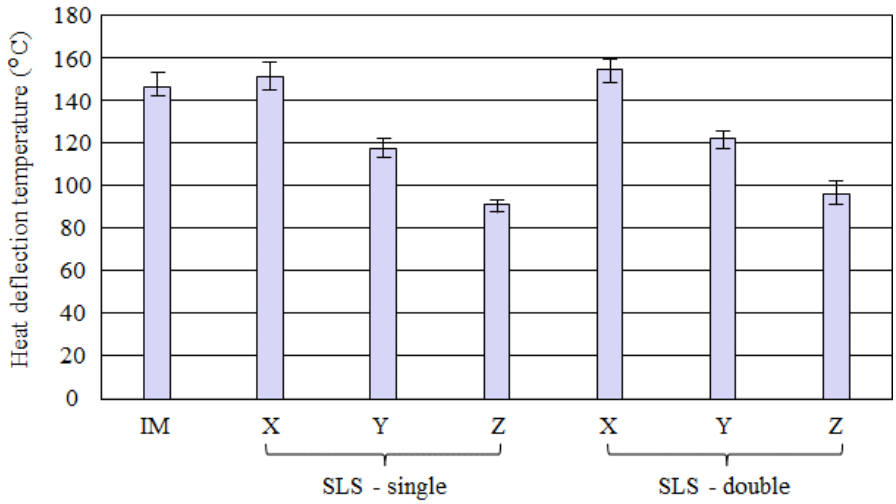

Fig. 13: Comparison of heat-deflection temperature (HDT) of IM and SLS specimens formed with single- and double-scan methods arranged in the X-, Y- and Z-build directions.

In the present study, compared to the case that the specimen is formed in the X-build direction, as indicated in Table 4, in the case of the Z-build direction, the degree of crystallinity is obviously a high value, but that trend is the opposite to that normally expected. This contradictory trend is due to the large difference in alignment of SGFs. Moreover, comparing the single- and double-scan cases reveals that HDT is higher by 4 to 5 °C in the latter case. This finding is supposed to be due to the difference in crystallinities.

In addition, when with IM and SLS specimens formed with 30-wt% SGF are compared, HDT under load is higher when the SLS specimen is formed in the X-build direction. From studies performed so far, it is known that IM specimens have no porosity compared to SLS specimens, the SGFs are 10 % shorter (although SGF

orientation ratio is slightly greater in the X- direction), and the degree of crystallinity is small. From this result as well, it can be judged that the influence of porosity is weaker in regard to HDT than in regard to mechanical characteristics. Results of the evaluation by TMA are plotted in Fig. 14.

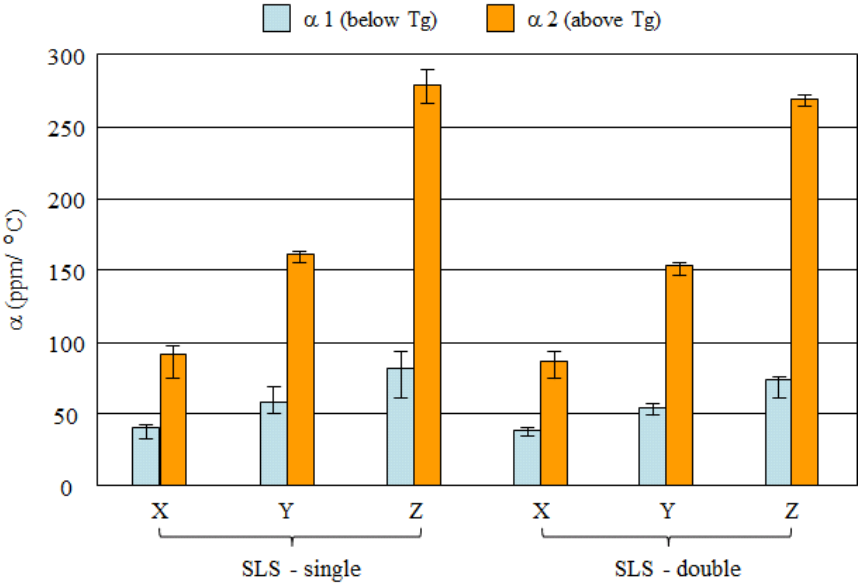

Fig. 14: Comparison of linear-expansion coefficient below and above glass-transition temperature (Tg) of SLS specimens formed with single- and double-scan methods and arranged in the X-, Y-, and Z-build directions.

According to these results, clear dependency on build direction due to the influence of alignment of SGFs can be seen. It is, however, clear that despite the fact that the specimens are reinforced with SGF, the linear-expansion coefficient in the Z-direction of the SGF-containing specimens is higher than that of cPBT (i.e., α2: 203 ppm/°C [12]). As for the reason for that result, it is conceivable that in regard to the X- and Y-build directions (in which SGFs align easily), by strongly suppressing linear expansion and applying compressive stress in the X- and Y-directions, that expansion distortion occurs in the Z-direction, and linear-expansion coefficient in the Z-direction increases. In addition, comparing the single- and double-scan cases shows that the latter

case has slightly smaller values. This trend is supposed to be due to the high degree of crystallinity in the latter case.

5-3-6. Shrinkage evaluation

Results of evaluating shrinkage ratios of specimens formed in the X-, Y, and Z-build directions by single- and double-scan SLS are listed in Table 5. Clear dependence of shrinkage ratio on build direction is observed in all build-direction cases. That is, the influence of orientation of SGFs is prominent.

Table 5: Comparison of shrinkage of SLS specimens formed with single- and double-scan methods and arranged in the X-, Y-, and Z-build directions.

Build direction	Scan method	Length (mm)	Excessive sinter depth (mm)	Shrinkage (%)
X	Single	197.30	-	1.35
Y	Single	195.16	-	2.42
Z	Single	193.08	0.43	3.68
X	Double	197.21	-	1.39
Y	Double	195.08	-	2.46
Z	Double	193.50	0.63	3.57

Comparing the single- and double-scan cases shows that shrinkage rate is slightly higher in the case of the double-scan-formed specimens when the specimen is formed in the X- and Y-build directions. In regard to the SLS process, it is presumed that there are two types of shrinkage: (i) shrinkage occurring when the specimens are held at high temperature in the powder during laser irradiation and (ii) shrinkage occurring during cooling until removal after completion of SLS processing. According to the results of TMA presented in subsection 5-4-7, linear-expansion coefficient is smaller in the case of the double-scan specimen than that in the case of the single-scan specimen. If only

cooling until removal after completion of SLS processing is considered, shrinkage ratio ought to be smaller in the case of the double-scan specimens. However, the influences of shrinkage during laser irradiation and holding at high temperature are considered to be greater in the double-scan case. In other words, it is presumed that as a result of the greater influences of shrinkage ratio during laser irradiation and high-temperature retention during SLS processing, shrinkage rate is higher in the double-scan case.

Furthermore, surplus sintering (namely, extra penetration depth in the depth direction) significantly influences dimension in the case of the Z-build direction [34]. Although laser energy density per one scan is lower for the double scan than that for the single scan, in double- scan case, each layer is irradiated twice, so excess sintering increased by 0.20 mm. When shrinkage ratios in the single- and double-scan cases are compared and this influence is eliminated, unlike the cases of the X- and Y-build directions, and the shrinkage ratio is smaller in the double-scan case.

In the case of the Z-build direction, unlike the cases of the X- and Y-build directions, the direction in which the shrinkage ratio is measured is the same as the layer-thickness direction; accordingly, even if shrinkage occurs during laser irradiation and holding at high temperature during SLS processing, as the powder continues to be supplemented, the shrinkage is canceled, and its influence seems to be small. In the case of cPBT as well, the same trend was clarified and shrinkage ratio in the X-direction was 3.56 % [14], whereas in the case the specimen was formed in the Z-build direction, it was 2.72 % (when laser-energy density is 22.7 kJ/m^2, and surplus-sintering amount is 0.48 mm). This result is presumed to be due to the effect of supplementing the powder resin. As a result, the double-scan specimen formed in the Z-build direction has a lower linear-expansion coefficient, so shrinkage ratio during cooling is also smaller;

consequently, it is considered that the shrinkage ratio of the double-scan specimens is smaller. Incidentally, when SGFs were added, shrinkage ratio in the Z-direction was about 0.96 % higher than that in the case SGFs were not added. As shown in subsection 5-4-6, it is presumed that due to inclusion of SGFs, the linear-expansion coefficient in the Z-direction is larger than that of cPBT.

5-4. Conclusions

cPBT with 30-wt%-added SGF was used to evaluate the dependence of build direction (X, Y, or Z) on properties of various specimens. It was confirmed that the mechanical properties of the specimens could be ranked in descending order of X > Y > Z in a similar manner to the degree of orientation of SGFs. In particular, comparing the dependences of X- and Z-build directions of specimens formed with cPBT revealed that when SGF was added, the influence of orientation of the SGFs was added, and the dependency on the build direction was increased. It was also revealed that in the case of the double-scan method, mechanical properties were maximized when the resin layer was irradiated twice at lower energy density than that used in the single scan. Furthermore, it was found that the effect of improving the mechanical properties by the double-scan laser-scanning method in the case of the Z-build direction was twice as large as that in the case of the X- and Y-build directions. This result is presumed to be due to the fact that the effect of suppressing deterioration of the resin is high in the former case. It was also confirmed that the double-scan method contributed greatly to reducing porosity.

HDT showed the same dependency on build direction as mechanical properties; however, the effect of the double-scan method was 4–5 °C higher than that of the

single-scan method. This trend is presumed to be due to the effect of increased crystallinity rather than the effect of reduced porosity. When the IM specimens were compared with SLS specimens formed in the X-build direction (in a similar manner to trend in alignment of SGFs), it was ascertained that the mechanical properties of the SLS specimens were lower. This trend seems to be mainly caused by the residual porosity of SLS. On the contrary, in regard to HDT, the SLS specimens showed higher values. This result is due to the fact that IM specimens are affected by about 10 % breakage of the SGFs (in the case of SLS, average fiber length does not decrease), and crystallinity is lower than that in the case of SLS; in the case of HDT, it is thus speculated that the influence of porosity is low.

Shrinkage ratio showed remarkably similar dependency on build direction as mechanical properties and HDT. However, when the single- and double-scan cases were compared, it became clear that in the cases of the X- and Y-build directions, despite the higher shrinkage rate in the double-scan case, in the case of the Z-build direction, shrinkage ratio was lower value and followed a different trend. This result is explained as follows. In the cases of the X- and Y-build directions, when the double-scan method is applied, the influences of shrinkage during holding at high temperature and laser irradiation during SLS processing are increased; on the contrary, in the case of the Z-build direction, the measured-shrinkage direction and lamination direction are the same. It is thus presumed that the main causes of the result concerning shrinkage ratio are the significant contributory effect of supplementing powder resin and the influence of increased crystallinity.

References

[1] A.J. Pinkerton, Lasers in additive manufacturing, Opt. Laser Technol. 78 (2016) 25–32.

[2] R.D. Goodridge, C.J. Tuck, R.J.M. Hague, Laser sintering of polyamides and other polymers, Prog. Mater. Sci. 57 (2012) 229–267.

[3] T.H.C Childs, A.E. Tontowi, Selective laser sintering of a crystalline and a glass-filled crystalline polymer: experiments and simulations, Proc. Inst. Mech. Engrs. Part B 215 (2001) 1481-1495.

[4] A. Salazar, A. Rico, J. Rodríguez, J. Segurado Escudero, R. Seltzer, F. Martin de la Escalera Cutillas, Fatigue crack growth of SLS polyamide 12: Effect of reinforcement and temperature, Composites: Part B 59 (2014) 285–292.

[5] D.A. Türk, F. Brenni, M. Zogg, M. Meboldt, Mechanical characterization of 3D printed polymers for fiber reinforced polymers processing, Mater. Des. 118 (2017) 256–265.

[6] F.R. Bruce, H. Gene, F. Kent, CFPC material characteristics and SLS prototyping process, Rapid Prototyp. J. 15 (2009) 339-345.

[7] C. Yan, L. Hao, L. Xu, Y. Shi, Preparation, Characterisation and processing of carbon fibre/polyamide-12 composites for selective laser sintering, Compos. Sci. Technol. 71 (2011) 1834–1841.

[8] A. Jansson, L. Pejryd, Characterisation of carbon-fibre-reinforced polyamide manufactured by selective laser sintering, Addit. Manuf. 9 (2016) 7–13.

[9] W. Jing, C. Hui , W. Qiong , L. Hongbo , L. Zhanjun, Surface modification of carbon fibers and the selective laser sintering of modified carbon fiber/nylon 12 composite powder, Mater. Des. 116 (2017) 253–260.

[10] S. Fischer, A. Pfister, V. Galitz, B. Lyons, C. Robinson, K. Rupel, R. Booth, S. Kubiak, A high-performance material for aerospace applications: development of carbon fiber filled PEKK for laser sintering, Proc. of the Solid Freeform Fabrications Symp., Austin, TX, (2016) 808-813.

[11] B. Chen, Y. Wang, S. Berretta, O. Ghita, Poly Aryl Ether Ketones (PAEKs) and carbon-reinforced PAEK powders for laser sintering, J. Mater. Sci. 52 (2017) 6004-6019.

[12] S. Arai, S. Tsunoda, A. Yamaguchi, T. Ougizawa, Effects of short-glass-fiber content on material and part properties of poly (butylene terephthalate) processed by selective laser sintering, Addit. Manuf. 21 (2018) 683–693.

[13] B.V. Hooreweder, J.P. Kruth, High cycle fatigue properties of selective laser sintered parts in polyamide 12, CIRP Ann. Manuf. Technol. 63 (2014) 241-244.

[14] S. Arai, S. Tsunoda , R. Kawamura , K. Kuboyama , T. Ougizawa, Comparison of crystallization characteristics and mechanical properties of poly(butylene terephthalate) processed by laser sintering and injection molding , Mater. Des. 113 (2017) 214–222.

[15] D. Bourell, J. Coholich, A. Chalancon, A. Bhat, Evaluation of energy density measures and validation for powder bed fusion of polyamide, CIRP Ann. Manuf. Technol. 66 (2017) 217–220.

[16] M. Pavan, M. Faes, D. Strobbe, B. Van Hooreweder, T. Craeghs, D. Moens, W. Dewulf, On the influence of inter-layer time and energy density on selected critical-to-quality properties of PA12 parts produced via laser sintering, Polym. Test. 61 (2017) 386-395.

[17] T. Stichel, T. Frick, T. Laumer, F. Tenner, T. Hausotte, M. Merklein, M.Schmidt, A Round Robin study for Selective Laser Sintering of polyamide 12: Microstructural origin of the mechanical properties, Opt. Laser Technol. 89 (2017) 31–40.

[18] B. Caulfield, P.E. McHugh, S. Lohfeld, Dependence of mechanical properties of polyamide components on build parameters in the SLS process, J. Mater. Process. Technol., 182 (2007) 477–488.

[19] T.L. Starr, T.J. Gornet, J.S. Usher, The effect of process conditions on mechanical properties of laser-sintered nylon, Rapid Prototyp. J. 17 (2011) 418-423.

[20] O.R. Ghita, E. James, R. Davies, S. Berretta, B. Singh, S. Flint, K.E. Evans. High temperature laser sintering (HT-LS): an investigation into mechanical properties and shrinkage characteristics of poly (ether ketone) (PEK) structures, Mater. Des. 61 (2014) 124–132.

[21] U. Ajoku, N. Saleh, N. Hopkinson, R. Hague, P. Erasenthiran. Investigating mechanical anisotropy and end-of-vector effect in laser-sintered nylon parts. Proc. IMechE. Part. B: J. Eng. Manufact. 200 (2016) 1077–86.

[22] M. Gupta, K.K. Wang, Fiber orientation and mechanical properties of short-fiber-reinforced injection-molded composites: Simulated and experimental results Polym. Compos. 14 (1993) 367-382.

[23] C.P. Fung, J.R. Hwang, C.C. Hsu, The effect of Injection Molding Process Parameters on the Tensile Properties of Short Glass Fiber-Reinforced PBT, Polym. Plast. Tech. Eng. 42 (2003) 45-63.

[24] S. Mortazavian, A. Fatemi, Effects of fiber orientation and anisotropy on tensile strength and elastic modulus of short fiber reinforced polymer composites, Composites: Part B 72 (2015) 116–129.

[25] H. Zarringhalam, N. Hopkinson, N.F. Kamperman, J.J. de Vlieger, Effects of processing on microstructure and properties of SLS nylon 12, Mater. Sci. Eng. A 435-436 (2006) 172–180.

[26] M. Chapiro, Current achievements and future outlook for composites in 3D printing,

Reinf. Plast. 60 (2016) 372-375.

[27] R.D Goodridge, R.J.M. Hague, C.J. Tuck, An empirical study into laser sintering of ultra-high molecular weight polyethylene (UHMWPE). J. Mater. Process. Technol., 210 (2010) 72–80.

[28] Y. Khalil, A. Kowalski, N. Hopkinson, Influence of energy density on flexural properties of laser-sintered UHMWPE, Addit. Manuf. 10 (2016) 67–75.

[29] T.B.N. Thi, M. Morioka, A. Yokoyama, S. Hamanaka, K. Yamashita, C. Nonomura, Measurement of fiber orientation distribution in injection-molded short-glass-fiber composites using X-ray computed tomography, J. Mater. Process. Technol., 219 (2015) 1–9.

[30] T. Suzuki, T. Sugita, M. Seto, H. Kakishima, H. Tanaka, M. Yamabe, Analysis of glass fiber orientation of an injection molded thin part using X-ray micro CT (Part 1) : extraction and quantification of glass fibers using cylinder-model fitting, Seikei-Kakou, 28 (2016) 239-246.

[31] R. Chávez-Medellín, LAS. de Almeida Prado, K. Schulte, Polyamide-12/functionalized carbon nanofiber composites: evaluation of thermal and mechanical properties, Macromol. Master. Eng. 295 (2010) 397-405.

[32] F.J. Vallejo, J.I. Eguiazábal, J. Nazábal, Solid state features and mechanical properties of PEI/PBT blends, J. Appl. Polym. Sci. 80 (2001) 885-892.

[33] N. Tomar, S.N. Maiti, Thermal and crystallization properties of PBT/ABAS blends, J. Appl. Polym. Sci. 113 (2009)1657-1663.

[34] K. Senthilkumaran, P.M. Pandey, P.V.M. Rao, Influence of building strategies on the accuracy of parts in selective laser sintering, Mater. Des. 30 (2009) 2946–2954.

[35] J. Bai, R.D Goodridge, R.J.M Hang, M. Okamoto, Processing and characterization of a polylactic acid/nanoclay composite for laser sintering, Polym. Compos. 38 (2017) 2570-2576.

[36] B. Van Hooreweder, D. Moens, R. Boonen, J.P.Kruth, P. Sas, On the difference in material structure and fatigue properties of nylon specimens produced by injection molding and selective laser sintering, Polym. Test. 32 (2013) 972–981.

[37] S. Dadbakhsh, L. Verbelen, O. Verkinderen, D. Strobbe, P. Van Puyvelde, J.P. Kruth, Effect of PA12 powder reuse on coalescence behaviour and microstructure of SLS parts, Eur. Polym. J. 92 (2017) 250–262.

[38] A. Khamsehnezhad, S. Hashemi, Mechanical properties of single- and double-gated injection moulded short glass fibre reinforced PBT/PC composites, J. Mater. Sci. 43 (2008) 6344-6352

[39] J.L. Thomason, Micromechanical parameters from macromechanical measurements on glass-reinforced polybutyleneterepthalate, Composites: Part A 33 (2002) 331-339.

[40] Y. Wang, E. James, O.R. Ghita, Glass bead filled Polyetherketone (PEK) composite by High Temperature Laser Sintering (HT-LS) , Mater. Des. 83 (2015) 545–551.

[41] X.F.Lu, J.N.Hay, Isothermal crystallization kinetics and melting behaviour of poly(ethylene terephthalate), polymer. 42 (2001) 9423-431

[42] T. Xu, J. Yu, Z. Jin, Effects of crystalline morphology on the impact behavior of polypropylene, Mater. Des. 22 (2001) 27–31.

[43] S. Xie, S. Zhang, F. Wang, H. Liu, M. Yang, Influence of annealing treatment on the heat distortion temperature of nylon-6/montmorillonite nanocomposites, Polym. Eng. Sci. 45 (2005) 1247–1253.

Chapter 6

General conclusions

In recent years, AM technology has been gaining attention due to popularization of low-cost 3D printers and improved performance and reduced cost of industrial equipment. Among AM technologies, SLS is starting to be used not only for prototypes but also for production of final parts, and its scope of application is expanding. However, the type of resin used for SLS is mainly PA12 and PA11, and its material limitation is the biggest problem. Although PBT resin features high heat resistance, good mechanical and electrical properties, high chemical resistance, and low cost, it is not commercially available as a resin for SLS, and very few studies on SLS have been done. Under those circumstances, in this study, the SLS process using PBT resin—with those many good characteristics—was investigated, and its various basic characteristics were evaluated and compared to those of an IM product.

As explained in **Chapter 2**, the influence of pulverization by cryogenic grinding was investigated by using cPBT pellets with low crystallinity (containing 10 mol% isophthalic acid). The investigation revealed that in the case of powder made from cPBT pellets pulverized at low temperature, although melting point, crystalline form, and molecular weight were unchanged by cryomilling, contaminants produced during the pulverization acted as nucleating agents of cPBT, which increased the crystallization temperature of the pulverized cPBT powder. As a result, although the process window became smaller, it was demonstrated that setting the powder-bed temperature of the SLS process to 190 °C made it possible to produce shaped articles with excellent characteristics.

As explained in **Chapter 3**, flame retardancy of cPBT was investigated. As for powder, two kinds of powders were used: (i) pulverized powder of flame-retardant cPBT pellets obtained by adding 10 wt% of flame-retardant poly(pentabromobenzyl

acrylate) (PPBBA) and 5 wt% of flame-retardant promoter antimony trioxide (ATO) to cPBT pellets (where ATO is embeded in PPBBA) and (ii) flame-retardant mixed powder obtained by dry-blending 10 wt% of PPBBA and 5 wt% of ATO pulverized into pulverized cPBT. It was revealed by the investigation that the combustion characteristics of the powder differed according to whether or not the ATO embeded in the PPBBA. Moreover, it was shown that although the ATO powder acted as a crystal nucleating agent for cPBT (which increases crystallization temperature), setting the powder-bed temperature to 192 °C made the SLS process possible with any powder. In addition, SLS products coated with ATO in cPBT and PPBBA showed superior mechanical and thermal properties than SLS products embedded in PPBBA with ATO. It was also revealed that although the combustion characteristics differed from products formed with either of the two powders, V0 grade in the UL 94 test could be attained with a thickness of 2 mm.

As reported in **Chapter 2** and **3**, the result of comparing various characteristics of SLS and IM products showed that SLS products had more porosity than IM products in the case of both cPBT and FR-cPBT, and all mechanical properties of both resins tended to decline. On the other hand, compared to the IM products, the SLS products were confirmed to have higher crystallinity because of a longer process time at high temperature. It was revealed that as a result of that higher crystallinity, the deflection temperature under load of the SLS products was higher than that of the IM products. However, the size of spherulites in the SLS products was smaller than that in the IM products. It is supposed that this finding is attributable to the fact that the nucleating-agent effect (due to contamination generated during powdering) is stronger than the influence of the process (IM or SLS).

As reported in **Chapter 4**, when the proportion of short-glass-fiber (SGF) addition (15, 30, 45, and 60 wt%) was taken as a parameter, various properties of the cPBT-SGF specimens manufactured by SLS were evaluated. As the proportion of added SGF was increased, the flowability of cPBT was degraded. In the case proportion of SGF addition was taken as a parameter, tensile strength and flexural strength of the SLS specimen were maximized by SGF addition of 30 wt%; however, impact strength was maximized by SGF addition of 45 wt%. As the proportion of added SGF was increased, the amount of SGF "debonding" also increased, while the amount of resin that adhered to the SGFs decreased and porosity increased. In addition, the average glass-fiber length of the SLS specimens decreased with addition of 45-wt% SGF, whereas it did not decrease with addition of 30-wt% SGF. Compared to SGF addition having an insignificant effect on mechanical properties, it significantly improved thermal properties (i.e., heat-deflection temperature and linear-expansion coefficient) and reduced shrinkage. Moreover, even if SGF was added, it had little effect on the crystallization properties of the powder and SLS-formed specimen.

As explained in **Chapter 5**, cPBT with addition of 30-wt% SGF was used to evaluate the dependence of the properties of specimens manufactured by SLS and the influence of laser-irradiation conditions on build direction. The degree of orientation of SGFs in SLS was ranked in descending order of roller-movement direction, vertical direction in the powder-bed plane, and direction of lamination-layer thickness. Moreover, the influence of fiber orientation on mechanical properties, thermal properties, and shrinkage ratio was found to be remarkable. In the case of the double-scan method in SLS, in comparison to the single-scan method, while thermal degradation was suppressed, porosity was reduced, and mechanical properties were improved.

Furthermore, in regard to roller-movement direction and lamination-layer thickness direction, the trends of shrinkage ratio differed in the cases of the single- and double-scan scanning methods. Moreover, it was revealed that the SLS product formed by double scan (in which the orientation of the fibers was similar to that in the IM product) had similar mechanical characteristics to the IM product (with fiber-breakage ratio of 10%) and a high HDT.

In summary, with respect to SLS specimens using PBT (which has very few research examples), we have succeeded in producing specimens of high-strength PBT—which can be used for actual products—by using cPBT-based materials. The cPBT powder used has been commercially available from Aspect Company as ASPEX PBT from June 2017. Furthermore, we have developed not only PBT but also flame-retardant PBT and SGF-reinforced PBT for SLS processing, and it is possible to increase SLS products line-up according to the application and develop these PBTs industrially. By comparing SLS products and IM products, we were able to understand detailed phenomena and mechanisms unique to SLS, such as ones that could not be grasped by research on traditional IM only (e.g., effects of ATO coating). From now onwards, while designing products with the characteristics of SLS in mind, we will accelerate the development of those designs to final products by utilizing the cPBT series developed in the present study.

Publications

[1] S. Arai, S. Tsunoda, R. Kawamura, K. Kuboyama, T. Ougizawa, Comparison of crystallization characteristics and mechanical properties of poly(butylene terephthalate) processed by laser sintering and injection molding , Mater. Des. 113 (2017) 214–222.

[2] S. Arai, S. Tsunoda, A. Yamaguchi, T. Ougizawa, Effects of short-glass-fiber content on material and part properties of poly (butylene terephthalate) processed by selective laser sintering, Addit. Manuf. 21 (2018) 683–693.

[3] S. Arai, S. Tsunoda, A. Yamaguchi, T. Ougizawa, Effect of anisotropy in the build direction and laser-scanning conditions on characterization of short-glass-fiber-reinforced PBT for laser sintering, Opt. Laser Technol. 113 (2019) 345–356.

[4] S. Arai, S. Tsunoda, A. Yamaguchi, T. Ougizawa, Characterization of flame-retardant poly(butylene terephthalate) processed by laser sintering, Opt. Laser Technol. 117 (2019) 94–104.

Acknowledgement

I express my sincere gratiude appreciation to Professor Toshiaki Ougizawa for accepting me as his student and giving his insightful comments as well as his scientific input while encouraging me throughout this research and leading me to my successful graduation.

I also express my gratutude to Dr. Keiichi Kuboyama, an assistant professor in the Ougizawa Laboratory, for his invaluable support.

In addition, I wish to thank Professor Yamabe Masashi and Tanaka Hiroaki, a reseacher at the Kanazawa Institute of Technology, for discussing and analyzing glass-fiber orientation.

I would also like to thank Hitachi Ltd. for giving me this opportunity to undertake my doctoral study at the Tokyo Institute of Technology.

Other invaluable support during my sutdies came from my wife, Yukiko, so I would like to express my deepest gratitude to her. Finally, I would like to thank my daughters, Miwa and Natsuki, for making my life wonderful at home.

Tokyo Institute of Technology

July 2019

Satoshi Arai